



GREEN SYNTHESIS OF MULTILAYER GRAPHENE/ZnO NANOCOMPOSITE FOR PHOTOCATALYTIC APPLICATIONS

by

DINEO PONO SEBUSO

Reg. No: 18100109

BSc (Physics, University of Botswana)

Department of Physics and Astronomy,

Faculty of Science,

Botswana International University of Science and Technology

dineo.sebuso@studentmail.biust.ac.bw, (+267 74657893)

A Dissertation Submitted to the Faculty of Science in Fulfilment of the Requirements for the Award of the Degree in Master of Science in Physics of Botswana International University of Science and Technology

Supervisors: Dr Cosmas M. Muiva

Senior Lecturer, Department of

Physics and Astronomy,

Faculty of Science, BIUST

muivac@biust.ac.bw, (+267) 4921566

Prof Alex T. Kuvarega

Associate Professor, Institute for

Nanotechnology and Water Sustainability

College of Science, Engineering and
Technology, University of South Africa

(UNISA)

kugarat@unisa.ac.za, +27(0) 116709198

Signature:  Date: 02/12/2021

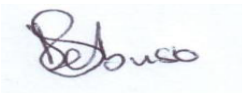
Signature:  Date: 02/12/2021

December 2021

DECLARATION AND COPYRIGHT

I, **DINEO PONO SEBUSO**, declare that this dissertation is my own original work and that it has not been presented and will not be presented to any other university for a similar or any other degree award.

Signature ...



Date.....02/12/21....

This dissertation is copyright material protected under the Berne Convention, the Copyright Act of 1999 and other international and national enactments, in that behalf, on intellectual property. It must not be reproduced by any means, in full or in part, except for short extracts in fair dealing; for researcher private study, critical scholarly review or discourse with an acknowledgement, without the written permission of the office of the Provost, on behalf of both the author and the BIUST.

CERTIFICATION

The undersigned certifies that he has read and hereby recommends for acceptance by the Faculty of Science a dissertation titled: **GREEN SYNTHESIS OF MULTILAYER GRAPHENE/ZnO NANOCOMPOSITE FOR PHOTOCATALYTIC APPLICATIONS** in fulfilment of the requirements for the degree of Master of Science in Physics (MSc Physics) of the Botswana International University of Science and Technology.


.....

Dr Cosmas M. Muiva
(Supervisor)

Date: 02/12/2021
.....


.....

Prof Alex T. Kuvarega
(Co-Supervisor)

Date: 02/12/2021
.....

ACKNOWLEDGEMENTS

First, I would like to extend my sincere gratitude to the good Lord, for providing me with the strength, wisdom and his grace throughout my studies. I am deeply grateful to my principal supervisor Dr Cosmas M. Muiva, for his assistance at every stage of the project, for his insightful comments and suggestions. Thank you for giving me an opportunity to be your mentee, your immense knowledge and experience have encouraged me to work extra hard to complete my studies besides all odds. I would also like to forward my heartfelt appreciation to my Co-supervisor Prof Alex T. Kuvarega for his unwavering support, guidance and contribution to my research project.

Special thanks goes to the Department of Physics and Astronomy technicians for the support and assistance they rendered in the use of equipment throughout my research project. Furthermore, I would like to extend my sincere appreciation to Dr Nagla Numan, a postdoctoral researcher, Materials Research Department (iThemba Labs), South Africa for the assistance she provided with sample characterization at University of Capetown and University of Western Cape, South Africa. No words can describe how grateful I am for the assistance you provided in my research work. I would also like to express my gratitude to my colleague, Ms Keadiretse Lefatshe (PhD Physics student) for the constructive comments and research advice she gave me throughout my studies.

I am particularly grateful for the support, warm encouragement and guidance provided by my family especially my parents; Mr Tiroyaone Sebuso and Ms Batendi Sebuso. Thank you for the love, care and financial support you provided everytime it got tough. Lastly, I would like to extend my profound acknowledgement to the Botswana International University of Science and Technology for providing funding for my research project.

Thank You! Kealeboga! Merci! Dank Je Wel!

DEDICATION

This research work is dedicated to my parents for being my pillar of strength, for the lessons they provided since childhood, without their tremendous support, encouragement and understanding, the completion of these studies would have been impossible.

TABLE OF CONTENTS

DECLARATION AND COPYRIGHT	i
CERTIFICATION	ii
ACKNOWLEDGEMENTS	iii
DEDICATION	iv
TABLE OF CONTENTS	v
LIST OF TABLES	viii
LIST OF FIGURES	ix
LIST OF ABBREVIATIONS	xi
LIST OF REVIEWED CONFERENCE PRESENTATIONS	xiii
ABSTRACT	xiv
CHAPTER 1: INTRODUCTION	1
1.0 Green Nanotechnology in Material Science	1
1.0.1 Green synthesis of nanoparticles	2
1.1 Heterogeneous Photocatalytic Applications of Nanomaterials.....	5
1.2 Statement of the problem	9
1.3 Aims and Objectives	10
1.4 Significance of Study.....	11
1.5 Dissertation Layout	11
CHAPTER 2: BACKGROUND INFORMATION AND LITERATURE REVIEW	13
2.0 INTRODUCTION	13
2.1 Heterogeneous Photocatalytic Applications of Semiconducting Metal Oxides .	13
2.1.1 Background Information on ZnO	18
2.1.2 Synthesis of ZnO	19

2.1.3 Green Synthesis of ZnO	20
2.1.4 Enhancing Photocatalytic Activity of ZnO Nanoparticles	24
2.2 Background Information on Graphene.....	26
2.2.1 Synthesis of Graphene	28
2.2.2 Green Synthesis of Graphene	28
CHAPTER 3: METHODOLOGY.....	34
3.0 INTRODUCTION	34
3.1 Materials and Methods	34
3.1.1 Green Synthesis of Multilayer Graphene from Waste Biomass	34
3.1.2 Green Synthesis of ZnO	38
3.1.3 Preparation of Multilayer Graphene/Zinc Oxide (MLG/ZnO) nanocomposites.	39
3.2 Sample Characterization.....	40
3.3 Photocatalytic Assessment	41
3.3.1 Photocatalytic Degradation of Organic Dyes	41
3.3.2 Photocatalytic degradation of Doxycycline (a Common Antibiotic)	42
3.4 Radical Scavenging Experiments	42
CHAPTER 4: RESULTS AND DISCUSSION.....	44
4.1 Structural and Morphological Characterization.....	44
4.1.1 Powder X-ray Diffraction analysis	44
4.1.2 Raman spectroscopy analysis	55
4.1.3 SEM AND HRTEM analysis.....	59
4.1.4 BET analysis	65
4.2 Optical Characterization Results	68
4.2.1 Absorbance and optical band gap energy.....	68

4.3 Photocatalytic Assessment	71
4.3.1 Photocatalytic degradation of organic dyes	71
4.3.2 Recyclability test.....	87
4.3.4 Photocatalytic degradation of DOX, a common antibiotic	88
4.3.3 Mechanism of photocatalytic degradation.....	91
CONCLUSION AND RECOMMENDATIONS	95
5.1 Conclusion.....	95
5.2 Recommendations for Future Work.....	97
REFERENCES	98

LIST OF TABLES

Table 2.1: Green synthesis of ZnO NPs by different researchers using plant extracts.	23
Table 2.2: Summary of experiments conducted on Carbon-based nanocomposites for photocatalytic applications.....	33
Table 3.1: Preparation conditions for different ratios of MLG/ZnO nanocomposite.....	40
Table 4.1: Crystal lattice parameters and unit volume of ZnO and ZnO in MLG/ZnO nanocomposites determined from XRD analysis.....	47
Table 4.2: Crystallite sizes from W-H and Scherrer and lattice strain of ZnO and MLG/ZnO composites from XRD analysis.....	50
Table 4.3: Crystallite size and lattice strain determined from H-W method.....	53
Table 4.4: Crystallite size and lattice strain determined from W-A plots.....	54
Table 4.5: BET Surface area and pore diameters of MLG, ZnO and MLG/ZnO nanocomposite	68
Table 4.6: Percentage degradation after 30 and 180 min of sunlight irradiation and.....	76
Table 4.7: Apparent rate constants for photodegradation of BB.....	79
Table 4.8: Percentage degradations of CR and RhB after 30 and 180 min of sunlight irradiation.	84
Table 4.9: Apparent rate constants for photodegradation of CR and RhB.	86
Table 4.10: Percentage degradation of BB, CR, RhB and DOX by MLG/ZnO nanocomposite in the absence and presence of various scavengers.	94

LIST OF FIGURES

Figure 1.1: Different methods for the fabrication of NPs.....	3
Figure 2.1: Mechanism for SMO photocatalysis.....	15
Figure 2.2: Applications of Metal Oxides.....	16
Figure 2.3: ZnO crystal structures a) cubic rocksalt b) cubic zinc blende c) hexagonal wurtzite [50].	19
Figure 2.4: Synthetic scheme for the green synthesis of NPs from plant extract [58].	22
Figure 2.5: A picture of A. Houstonianum weed.	23
Figure 2.6: Allotropes of carbon: a) 2-D graphene, b) 0-D fullerene, c) 1-D carbon nanotube, d) 3-D graphite [95].....	27
Figure 2.7: Typical schematic diagram for extraction of cellulose.	30
Figure 3.1: Schematic plan for extraction of cellulose.	35
Figure 3.2: Schematic diagram for the synthesis of MLG.....	36
Figure 3.3: Prepared leaf extract.	37
Figure 4.1: XRD patterns of MLG and its main predecessor stages (CH-C and CH-AC).	45
Figure 4.2: XRD patterns of ZnO and MLG/ZnO composites (# indicates the multilayer graphene peak in the composite).	46
Figure 4.3: Williamson-Hall plots for pure ZnO and MLG nanocomposites.....	50
Figure 4.4: Halder-Wagner plots for pristine ZnO and MLG/ZnO nanocomposites.....	52
Figure 4.5: Wagner-Agua plots for pure ZnO and MLG/ZnO composites.	54
Figure 4.6: Raman spectra of MLG, CH-C and CH-AC.	56
Figure 4.7: Raman spectra of pure ZnO and MLG/ZnO nanocomposites.....	58
Figure 4.8: SEM micrographs of MLG and its treatment stages (a-d) and pristine ZnO (e), f) MLG/ZnO_3 nanocomposite taken at low and high magnifications.....	61
Figure 4.9: a) particle size histogram of ZnO NPs b) EDS spectrum of MLG/ZnO_3 nanocomposite.....	62
Figure 4.10: HRTEM images of a) ZnO, b) MLG. Insert is SAED patterns of MLG and c) MLG/ZnO_3 composite with calculated d-spacing using lattice fringes d) SAED patterns of MLG/ZnO_3.....	64

Figure 4.11: t-plots for a) MLG and b) MLG/ZnO_3 (inset shows N ₂ adsorption-desorption isotherm plots at 77 K for the two materials which were used to acquire the t-plot) c) N ₂ adsorption-desorption isotherm plot at 77 K for ZnO (inset shows BET surface plot) and d) Pore size distribution curves for the three materials as labelled.....	67
Figure 4.12: UV-Vis absorption spectra of MLG, ZnO and MLG/ZnO nanocomposites.	69
Figure 4.13: Evaluation of plotted $(\alpha h\nu)^2$ against photon energy (hν) for determining the optical energy band gap of MLG, ZnO and MLG/ZnO nanocomposites.....	71
Figure 4.14: Evidence of dye colour change due to the photocatalysts as indicated in the pictures.	72
Figure 4.15: Absorbance spectra for the degradation of BB in the absence of a catalyst and in the presence of MLG, ZnO, MLG/ZnO_1, MLG/ZnO_2 and MLG/ZnO_3.....	74
Figure 4.16: A graph of percentage degradation of BB as a function of time photocatalyzed by different samples as indicated.	75
Figure 4.17: Photocatalytic degradation of BB by different photocatalysts as indicated.	77
Figure 4.18: A Langmuir-Hinshelwood plot for obtaining the reaction rate.....	78
Figure 4.19: Absorption profiles of CR and RhB in a) absence of catalysts, c) and e) presence of ZnO , d) and f) presence of MLG/ZnO_3.	82
Figure 4.20: Percentage degradation of a) CR and RhB by ZnO and MLG/ZnO_3.	84
Figure 4.21: Photocatalytic degradation of a) CR and b) RhB by ZnO and MLG/ZnO_3.	85
Figure 4.22: Kinetic plots for the photocatalytic degradation of a) CR and b) RhB.	86
Figure 4.23: Recyclability test for ZnO and MLG/ZnO_3 photocatalysts.	87
Figure 4.24: Changes in UV-Vis absorption spectrum of aqueous DOX solution under UV irradiation a) without catalyst and b) in the presence of MLG/ZnO_3.	88
Figure 4.25: a) Percentage degradation of DOX as a function of time photocatalyzed by MLG/ZnO_3 and b) Photocatalytic degradation of DOX by MLG/ZnO_3.....	89
Figure 4.26: Kinetic plot for the photodegradation of DOX.	90
Figure 4.27: a) Mechanism of photocatalytic reaction of MLG/ZnO and b) band gap diagram for MLG/ZnO composite.	92
Figure 4.28: Percentage degradation of CR, RhB, DOX and BB by MLG/ZnO_3 nanocomposite in the absence and presence of various scavengers.	94

LIST OF ABBREVIATIONS

ROS	Reactive Oxygen Species
AOP	Advanced Oxidation Process
nm	Nanometer
rpm	Revolution per minute
SMOs	Semiconductor Metal Oxides
e^-/h^+	Electron-hole pair
NPs	Nanoparticles
CNCs	Cellulose Nanocrystals
ZnO	Zinc Oxide
MLG	Multilayer Graphene
MLG/ZnO	Multilayer Graphene/Zinc Oxide
FLG	Few Layered Graphene
CH-C	Corn Husk Carbonized
CH-AC	Corn Husk Activated Carbon
Min	Minutes
BB	Brilliant Black
RhB	Rhodamine B
CR	Congo Red
DOX	Doxycycline
M	Molar
hrs	Hours
eV	Electron Volt

SEM	Scanning Electron Microscope
XRD	X-Ray Diffraction
HRTEM	High Resolution Transmission Electron Microscope
UV-Vis-NIR	Ultraviolet, visible and near infrared radiation
W-H	Williamson-Hall
H-W	Halder-Wagner
W-A	Wagner-Agua
COD	Crystallography Open Database
D	Crystallite Size
L-H	Langmuir-Hinshelwood
IUPAC	International Union of Pure and Applied Chemistry

LIST OF REVIEWED CONFERENCE PRESENTATIONS

1. **Dineo. P. Sebuso**, Keadiretse. Lefatshe, Alex. T. Kuvarega, Cosmas. M. Muiva. “Green Synthesis of Graphene from waste biomass: Corn husk” 10th International Conference of the African Materials Research Society (AMRS, 2019), 10th-13th December 2019 held at Nelson Mandela African Institute of Science & Technology, Arusha, Tanzania.

ABSTRACT

Green nanotechnology is an innovative research field with emphasis on the development of methods that minimize the use of health hazardous substances for environmental remediation. This study reports on the biosynthesis of nanostructured multilayer graphene (MLG) and zinc oxide (ZnO) from natural extracts for environmental applications. ZnO nanoparticles are fabricated for the first-time using *Ageratum Houstonianum* leaf extract as an effective chelating agent. Besides this, a green chemistry route involving the utilization of waste biomass was used for fabrication of multilayer graphene. This route was chosen because it offers good control of size, morphology and does not involve use of toxic reducing agents or surfactants thus contributing towards green nanotechnology. MLG was synthesized from corn husk via alkali-acid treatment. This entails extraction of cellulose followed by carbonization of the nanomaterial and activation of the carbon material. The separately synthesized nanostructures were used to synthesize MLG/ZnO nanocomposites of different ratios of MLG/ZnO (1:1, 1:2, 1:3) through *ex-situ* casting of the two materials (MLG/ZnO_1, MLG/ZnO_2, MLG/ZnO_3). The X-ray diffraction (XRD) profiles and Raman spectra exhibited predominant features of MLG and confirmed a hexagonal wurtzite phase of ZnO in the composite verifying the formation of MLG/ZnO nanocomposite. The UV-Vis absorbance spectra analysis revealed that incorporation of MLG to ZnO narrowed the band gap of ZnO nanoparticles, and consequently improved the light absorption of the semiconductor in the visible range. From Scanning electron microscopy (SEM) and High-Resolution TEM (HRTEM) analysis, short hexagonal nanorods were observed for ZnO while sheet-like structures with ripples and crinkles were observed for MLG. Energy dispersive spectroscopy (EDS) confirmed the purity of the samples and successful incorporation of MLG and ZnO with presence of only C, O and Zn in the composites. Brunauer-Emmett-Teller (BET) analysis revealed less surface area of 0.42 m²/g for bare ZnO and increased surface area of 148.74 m²/g in the composite (MLG/ZnO_3). Brilliant black (BB), congo red (CR) and rhodamine B (RhB) were chosen as model pollutants in this study, because they are among the many water pollutants from textiles and industries which are found to be stable with complex structures hence making them environmentally problematic. The nanocomposites were initially applied for

photodegradation of BB under direct sunlight irradiation to determine the best performing nanocomposite. It is worth to note that MLG/ZnO_3 nanocomposite showed the best photocatalytic performance of 93% degradation compared to pristine ZnO, MLG/ZnO_1 and MLG/ZnO_2, which showed lower photocatalytic activity. The best performing nanocomposite was further used to degrade CR and RhB and gave degradation efficiencies of 86 and 100%, respectively while pure ZnO showed degradations of 71% and 85% for CR and RhB, respectively. The obtained results showed high photocatalytic activity for the optimized MLG/ZnO nanocomposite in RhB and CR under natural sunlight irradiation. The nanocomposite further demonstrated 95% degradation for doxycycline (DOX) under UV light. The photodegradation mechanism was proposed and discussed in light of scavenging experiments using the optimum composite for all the four pollutants. It was revealed that holes play a major role in photodegradation of BB while the main reactive species in the photodecomposition of CR, RhB and DOX were found to be superoxide radicals. This work provides an insight for cheap, sustainable and eco-friendly methods for the fabrication of nanomaterials for environmental remediation and better ways of recycling waste biomass to fabricate valuable materials to solve society problems.

CHAPTER 1: INTRODUCTION

1.0 Green Nanotechnology in Material Science

Technological development and fast growth of research has resulted in the mushrooming of innovative ideas for the betterment of human living standards. The development of nanomaterials through nanotechnology has drawn much attention. Nanotechnology is a hugely growing sector due to its various applications in science and technology. It is defined as the manufacture and exploitation of materials and devices on the scale of atoms or small groups of atoms. The word “nano” is extracted from the Greek word “nanos” which symbolize dwarf or microscopic [1].

Nanotechnology describes technologies working on nanoscales comprising of nanoparticles which are atomic or molecular clusters with particle sizes ranging between 1 and 100 nm [2]. Nanostructures generally refer to molecular clusters with atleast 1 dimension in this range. The term nanotechnology was firstly introduced by a Japanese Professor in Tokyo Science University called Norio Taniguchi (1974) but its historic origin is linked to the physicist Professor Richard Feynman [3]. Ever since its introduction, it has advanced rapidly in the past one to two decades leading to development of functional nanostructures and advances of new synthesis methods of nanoparticles (NPs) to minimize negative impact on the environment among other application fields.

NPs can be categorized into different groups based on their size, morphology and chemical properties. These classes include carbon-based NPs, metal NPs, ceramics NPs, semiconductor NPs, polymeric NPs and lipid-based NPs. Carbon-based NPs include two major materials, fullerenes and carbon nanotubes (CNTs). Fullerenes are allotropes of carbon possessing a structure of hollow cage [4]. CNTs are cylindrical rolled up graphene sheet with hexagonal structure of hybridized carbon atoms [5].

Semiconductor NPs display properties between metals and nonmetals, therefore they can be applied in various fields. NPs possess enhanced physical properties such as surface area, functionalization, quantum confinement, uniformity and optical properties based on particle distribution, size and morphology. Due to these properties NPs can be considered for various applications such as catalysis, electrochemistry, medical devices, textile industry, electronics and photonics, information storage, chemical sensing, environmental decontamination, biological labelling and drug delivery, etc [6,7].

The need to rescue the environment has led to the birth of a resultant field and nascent branch of nanotechnology called green nanotechnology [8]. Green nanotechnology is an innovative research field that focuses on the production of environmentally sustainable products which can be used for environmental remediation. It focuses on the use of non-toxic compounds to synthesize nanomaterials, thereby promoting environmental sustainability of NPs development [9].

Semiconductor metal oxides (SMOs) and carbon-based materials have attracted much attention recently due to their intrinsic properties and applications. Carbon-based materials have amazing physical, chemical, thermal and electric properties, whereas semiconductor metal oxides possess high exciton binding energy, high thermal and chemical stability. In recent years, research has focused on the incorporation of SMOs with carbon-based materials for enhanced photocatalytic activities.

1.0.1 Green synthesis of nanoparticles

Synthesis of nanostructures and nanomaterials are one of the major keys of nanotechnology and nanoscience. NPs are synthesized through different methods which can be classified into top to bottom or bottom to top approach. The various

methods used for fabrication of NPs are illustrated in Figure 1.1. Bottom to top approach refers to the formation of NPs due to the build-up of materials from atom to clusters while top to bottom approach involves the reduction of bulk material into nanosized particles [10]. Although nanomaterials are popularly synthesized using different physical and chemical methods, most of them lead to environmental pollution due to the release of toxic chemicals. Therefore, this study focuses on bioremediation.

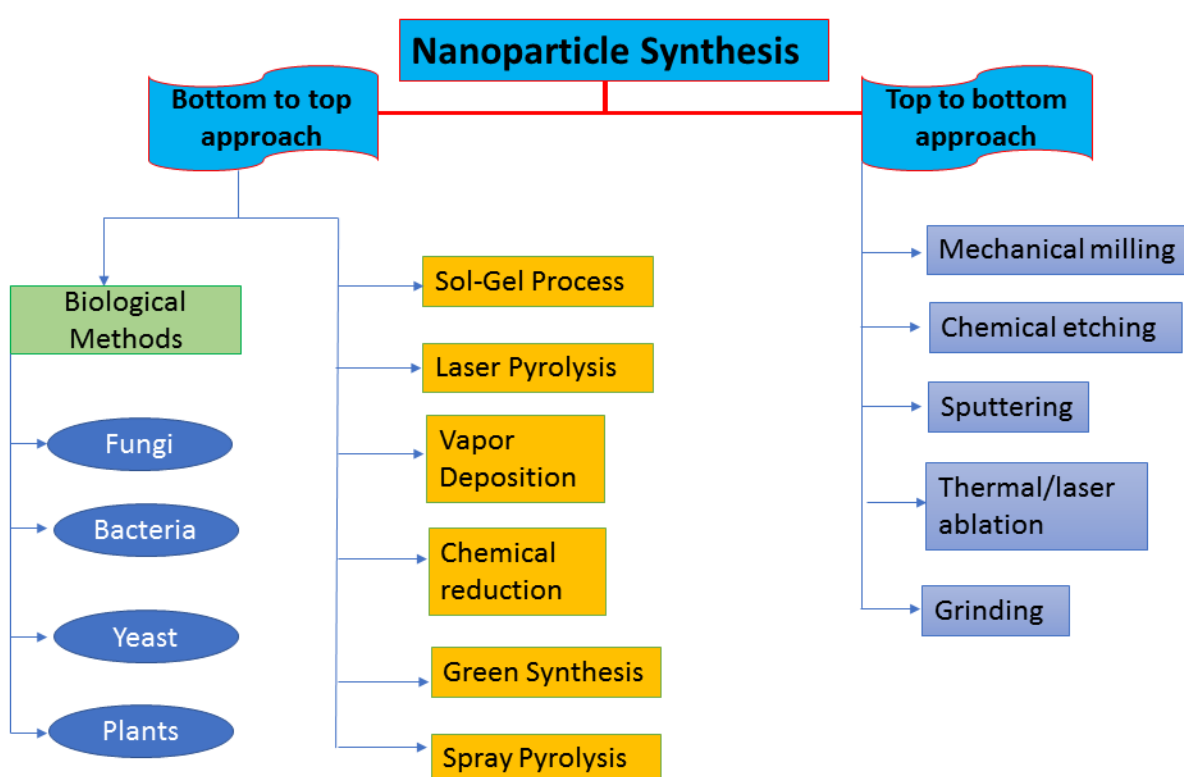


Figure 1.1: Different methods for the fabrication of NPs.

Green synthesis method has attracted great attention due to its amazing benefits such as low-costs, environmental friendliness as toxic chemicals are not used, simple processes, can be used at large scale production of NPs and is energy saving [8,11]. Green chemistry comprises of the use of natural reducing, capping and stabilizing

agents to fabricate NPs with preferred size and morphology. Biosynthesis of nanostructures includes the use of microorganisms or plants. The plant based synthesis has become more attractive to obtain metal and metal oxide NPs due to easy availability of extracts, simple processes involved, low costs and environmental friendliness [9].

Carbon-based materials can be fabricated from waste biomass to emphasize the spirit of green nanotechnology for environmental remediation. Biowaste materials are currently of high interest due to their abundance, being sufficient sources of carbon and the need for recycling. Biomass from plant wastes is mostly composed of proteins, carbohydrates and fiber. Plant fiber mainly consists of lignin, cellulose, hemicellulose and small amounts of starches, protein and lipids [12]. Corn husk is one of the waste biomass materials that can be converted into carbonaceous materials including graphene. Cornhusk lignocellulosic material comprises of lignin, hemicellulose and cellulose. The pretreatment of cellulosic biomass can be done through alkali and acid hydrolysis to dissolve residual hemicellulose. The extracted cellulose can be carbonized followed by activation of the carbon material to be considered for further treatments for fabrication of graphene.

Different methods have been reported for the synthesis of a semiconductor carbon-based nanocomposite, and this includes *in-situ* and *ex-situ* casting of the materials. *In-situ* synthesis is a method that allows the NPs to be synthesized within the matrix during fabrication of the composite. This method has some limitations; it is difficult to control size and morphology of the NPs formed in the composite. It can involve the use of chemicals which can be harmful to the environment if not disposed properly. *In-situ* synthesis can involve the use of expensive equipment which requires high energy to operate. *Ex-situ* casting of materials refers to a synthetic method where pre-synthesized materials are inserted into the matrix in a secondary process involving powder processing of infiltration. *Ex-situ* synthesis of composite guarantees good control of size, morphology, distribution and density of NPs on the host material due

to preliminary synthesis of NPs. It also involves the use of harmless solvents like deionized water and does not involve the use of toxic reducing agents or surfactants and it is less expensive.

1.1 Heterogeneous Photocatalytic Applications of Nanomaterials

The use of non-renewable sources has increased over the years due to the rapid growth of technological industries. There is an increase in demand of materials related to fertilizers, textile, dyes, pharmaceuticals, plastic etc. As a result, environmental pollution and energy crises have become a major problem. Organic dyes released from industries are a great threat to the environment since they are chemically stable and difficult to biodegrade in water hence causes water pollution. Previous researchers [13-16] have indicated that another major source of environmental contamination is from chemical drugs that find their way into ground water and wastewater after release from industries, households and municipal wastewater. The improper disposal of expired drugs leads to an increase in contamination from drugs. Therefore, multidrug resistance is a major concern in the treatment of contagious diseases [17]. This has caused so many problems in the health system. Hence, efforts were made to develop technologies to assist in removal of these pollutants through degrading organic pollutants and pharmaceuticals.

Research findings reveal that about 3.2 million children perish each year due to drinking contaminated water as a result of poor sanitation in developing countries [18]. Various chemical, biological and physical methods are currently employed for water treatment including adsorption, precipitation, sedimentation, filtration, Fenton process, coagulation, ozonation, membrane separation process, reverse osmosis and oxidation ditch [19,20]. The adsorption method does not degrade the pollutants completely but grant quick separation with high recoveries. These methods are not

adequate for wastewater treatment since they come with significant drawbacks including high energy use, ineffective degradation of pollutants and build-up of harmful sludge after treatment [18,20]. They are also expensive to operate on large scale and require long process time hence are inefficient in wastewater treatment. Therefore, there is a vital requirement for developing economically viable wastewater treatment methods.

Nanotechnology through advanced oxidation processes (AOPs) has emerged as a promising approach for the degradation of organic and inorganic pollutants [21]. AOPs are processes which rely on the formation of highly reactive radicals that react with pollutant molecules to degrade them into non-toxic compounds. Metal NPs and metal oxides NPs are considered good catalysts in oxidation reactions. Nanomaterials are considered good catalysts due to their size and properties. They can also act as sensors for some selected pollutants in wastewater. They oxidize the pollutant molecules to less toxic substances. Therefore, nanocatalysts can effectively be used in AOPs for chemical oxidation of organic and inorganic pollutants in water. However, AOPs have some limitations such as high energy costs. It has been reported that among the AOPs, semiconductor-mediated heterogeneous photocatalysis is an effective technique for the degradation of pollutants because of low cost, non-toxicity, easy operation, reusability and complete mineralization of organic compounds to H₂O and CO₂ [22,23].

For better photocatalytic performance, the photocatalyst should possess the following properties; proper substrate to immobilize the photocatalyst, higher adsorption of the pollutant molecule and lower recombination rate of the excited electrons to allow enough time for the degradation of the organic pollutant [24]. However, SMOs have some drawbacks in the field of photocatalysis; most SMOs suffer from rapid electron-hole recombination effect resulting in reduced photocatalytic activity. The fast recombination is attributed to the wide band of semiconductors like zinc oxide (ZnO) which leads to a decrease in photocatalytic efficiency in the UV region. In addition,

effective surface area is one of the key factors for rapid degradation of organic molecules during a photocatalytic reaction. A large surface area provides more active sites on the surface of the photocatalyst for easy adsorption of organic molecules for improved interaction between the catalyst and the organic molecules. Nanomaterials offer this advantage owing to their large surface area to volume compared to the bulk. The useful photocatalytic properties of the nanomaterials can be improved by modifying their morphology and structures for enhanced performance. These properties can be improved through fabrication of a heterostructure through noble metal loading, ion doping and incorporation of electron-accepting materials [22].

Several metal oxides have been studied for their photocatalytic properties. However, research activities are mostly focused on titanium dioxide (TiO_2) and ZnO for photocatalytic degradation of organic dyes and pharmaceuticals for water purification. Some previous researchers [25] reported that the use of TiO_2 for remediation of organic pollutants in wastewater comes with some drawbacks because of catalyst poisoning. Furthermore, another challenge is that TiO_2 is largely responsive towards ultraviolet light irradiation. The photocatalytic activity of TiO_2 in the visible region is very low [26,27] due to low absorption emanating from a band gap (3.5 eV) encroaching into the UV region. ZnO is a promising photocatalyst for degradation of organic dyes and pharmaceuticals due to its non-toxicity, high photosensitivity, high chemical stability and low-cost [28]. However, ZnO suffers from photocorrosion effect due to the rapid recombination of the photogenerated electron-hole pairs. Therefore, it is important to reduce the rate of electron-hole pair recombination. This can be achieved by lowering the band gap of ZnO for improved photocatalytic performance. Efforts were made to modify ZnO for enhanced photoresponse. ZnO can be incorporated with carbon-based materials to assist in charge transfer between the metal oxide and the organic molecules for improved photocatalytic activities [24,29]. Carbon-based composites improve the photocatalytic performance of the host material by contributing intrinsic properties. The formation of nanocomposites also reduces the potential photocorrosion of ZnO on exposure to UV radiation.

The incorporation of ZnO with carbon-based materials yields what is known as a nanocomposite. The development of a nanocomposite is another logical technique to make semiconductors photoresponsive in the visible region of the spectrum. Incorporation of semiconductor with carbon-based materials provides a large surface area for easy adsorption of pollutant molecules for enhanced interaction between the organic molecules and the catalyst. The carbon-based materials include graphene, reduced graphene oxide (RGO), activated carbon and carbon nanotubes [30]. In this study ZnO was incorporated with multilayer graphene (MLG) for enhanced photocatalytic performance. MLG was chosen due to its ground breaking properties in new applications including photocatalysis, energy storage and single molecule gas detection [31]. Its large surface area makes it a good candidate for adsorption of aromatic organic compounds via p-p electron coupling of Van der Waals interactions [32]. It is ideal to incorporate SMOs with MLG for enhanced photocatalytic performance.

In order to reduce the energy requirement for application and in the spirit of green nanotechnology, natural solar light was used as a source of light for the photocatalytic degradation of organic dyes. Therefore, it is crucial for the photocatalyst to absorb in the visible light region. But most SMOs are incapable of utilizing abundant clean and safe solar energy. ZnO nanostructures suffers restrictions and makes use of about 4% of the UV part of solar energy. As already stated, efforts are being made to expand the photoresponse of ZnO into the visible-light region of about 43% of solar spectrum [21]. However, this study also explored the photoresponse of ZnO in the UV region by using multilayer graphene/zinc oxide (MLG/ZnO) nanocomposite to degrade a common antibiotic under UV irradiation.

1.2 Statement of the problem

Building up of waste biomass has always been a problem in towns and cities. Recycling which entails valorisation of these waste products is one of the strategies being adopted worldwide to deal with this menace. Waste biomass materials are of interest due to the need for recycling, abundance and being sufficient sources of carbon.

Heterogeneous semiconductor-mediated photocatalysis has been widely employed for the treatment of pollutants in the environment. Semiconductor metal oxide ZnO is a promising material for environmental remediation. ZnO has been widely studied and used as a photocatalyst due to its electronic band structure which absorbs energy in the UV region. However, it has some limitations. ZnO encounters photocorrosion effect during photocatalysis due to the rapid electron-hole recombination hence lowering its quantum yield and photocatalytic activity. Reduced photocatalytic activity is also contributed by a smaller effective surface area for photon absorption. Another challenge is fabrication of ZnO NPs since common routes such as Sol-gel, chemical vapor deposition (CVD), hydrothermal and wet chemical methods, generate a number of chemical waste products that find their way into the environment. Therefore, there is need to explore green routes.

Population growth and technological development have contributed to increase in various environmental pollutants including organic dyes, fertilizers, drugs, pesticides etc. These contaminants are usually lost into the water streams, hence causing severe environmental problems. Particularly, organic dyes possess a threat to the aquatic life since they impair photosynthesis, may promote toxicity, carcinogenicity and mutagenicity and inhibit plant growth. Most of consumed antibiotics exit the organism in their original form contributing to environmental contamination. Therefore, widely used antibiotics like doxycycline (DOX) results in having an increasing number of bacteria resistant to their antimicrobial action.

1.3 Aims and Objectives

This study focuses on green synthesis of a nanocomposite with exceptional photocatalytic activity under visible light. It also emphasizes on the improvement of photocatalytic activity of semiconductors by incorporating them with carbon-based materials.

The materials of interest in this study are semiconducting metal oxide, zinc oxide (ZnO) and a carbon-based material, multilayer graphene. In the anticipated work, ZnO NPs will be embedded on the MLG sheets to fabricate MLG/ZnO nanocomposite and test the photodegradation efficiency of the nanocomposite. This will be achieved through the following objectives.

- Green synthesis of ZnO using *Ageratum Houstonianum* (*A. Houstonianum*) leaf extract.
- Green synthesis of MLG from corn husk through extraction of cellulose from waste biomass.
- Green synthesis of MLG/ZnO nanocomposite through *ex-situ* casting of the two materials.
- Optimization of the MLG concentrations in the MLG/ZnO nanocomposite for enhanced photodegradation of brilliant black (BB) dye.
- Investigation of the photocatalytic activity of MLG/ZnO nanocomposite against congo red (CR), rhodamine B (RhB) and doxycycline (DOX).

1.4 Significance of Study

This study focuses on the use of cheap, simple processes and non-toxic compounds for the fabrication of nanomaterials to solve environmental problems. It emphasizes on clean nanotechnology for the synthesis of an environmentally friendly nanocomposite for enhanced photocatalytic activity for degradation of organic pollutants and pharmaceuticals. To start with ZnO is prepared for the first time from *Ageratum Houstonianum* leaf extract. In addition, graphene is prepared from waste biomass which is an abundant environmental nuisance. This work provides a new insight into novel ways of recycling waste biomass and using them to fabricate valuable materials for photodegradation experiments.

One of the hiccups that hinder photocatalytic degradation of ZnO is charge recombination. To mitigate this ZnO is incorporated with MLG to improve charge transfer between the metal oxide and the pollutant. This reduces the chances of electron-hole recombination. Furthermore, incorporation of a semiconductor metal oxide with carbon-based materials increases the active surface area for easy adsorption of pollutants for enhanced interaction between the catalyst and the organic molecules. Utilization of the two materials reduces the agglomeration of the ZnO NPs. Agglomeration of NPs reduces their photocatalytic activity by hindering enough light from reaching the SMOs active sites.

1.5 Dissertation Layout

This dissertation is divided into five chapters; Introduction, Background Information and Literature review, Methodology, Results and Discussion, Conclusion and Recommendations for future work.

Chapter 1: Introduction

Brief information of green nanotechnology in material science is given in this chapter. It further explains the concept of heterogeneous photocatalytic applications of nanomaterials. It outlines the significance, motivation, aims and objectives of the study.

Chapter 2: Background Information and Literature review

It gives background information on the materials of interest, ZnO and graphene. It extensively explains their structure, synthetic routes and applications with emphasis on modification of SMOs structures for enhanced photocatalytic applications. This chapter also explains in full the previous studies conducted with similar objectives, their findings, drawbacks and the gaps identified in the research field.

Chapter 3: Methodology

This chapter elaborates on the synthetic route, characterization techniques and assessment approach.

Chapter 4: Results and discussion

It presents the results obtained on the structural, morphological and optical characterization of the materials, photocatalytic assessment and discusses them in depth.

Chapter 5: Conclusion and recommendations

This chapter gives a summary of the project and suggests recommendations for future work. References are given at the end of the dissertation. The next chapter gives background information on the materials and the previous studies conducted with the same objectives.

CHAPTER 2: BACKGROUND INFORMATION AND LITERATURE

REVIEW

2.0 INTRODUCTION

This chapter investigates the properties and applications of ZnO and graphene nanomaterials. It elaborates in depth the photocatalytic applications of the two materials. The amazing properties of ZnO make it an excellent candidate for photocatalytic applications. However, ZnO has some limitations of experiencing photocorrosion effect therefore research activities nowadays are coming up with ways of incorporating it with carbon-based materials to help in charge transfer between the metal oxide and the organic molecules. The incorporation of ZnO NPs and carbon-based material in a form of a nanocomposite is to modify its physical and morphological structure for enhanced photocatalytic activities.

2.1 Heterogeneous Photocatalytic Applications of Semiconducting Metal Oxides

Historically, various methods have been adopted for treatment of contaminated water. Polluted waters were successfully treated by conventional methods including biological processes, reverse osmosis (RO), chlorination, adsorption on activated carbon, thermal oxidation, etc. [33]. However, there has been some reported limitations associated with these methods such as inefficiency due to poor removal capacity and unpleasant conditions with high operational costs [34,35]. There are efforts focused on developing efficient novel methods such as AOPs for total removal of pollutants including those resistant to conventional methods. These processes employ reactive species for the degradation of pollutants. AOPs includes photo-Fenton oxidation, photocatalysis and ozonation [36]. The best AOP for environmental

remediation is photocatalysis [37]. Photocatalysis is the use of a catalyst for the acceleration of chemical reactions in the presence of light. A material that absorbs light, generate electron-hole pairs to be utilized in chemical reactions is called a photocatalyst. A photocatalyst remains unchanged after each cycle of chemical interaction. Applications of photocatalysis includes bacterial disinfection, degradation of pollutants, water splitting to hydrogen (H₂) and oxygen (O₂), selective organic transformation, carbondioxide (CO₂) reduction to energy fuels and in biomedical applications such as cancer treatment etc. Photocatalysis occurs on the surface of the metal oxide and after absorption of a photon, therefore a good photocatalyst can be determined by the following features; high surface area, stability, desired band gap, recyclability and suitable morphology [38,39]. Photocatalytic reactions are divided into two categories which are homogeneous photocatalysis and heterogeneous photocatalysis [40].

Heterogeneous photocatalysis involves the use of SMOs for environmental remediation. This process involves two states; the solid state of the photocatalyst and the liquid state of the contaminant. The interest in heterogeneous photocatalysis dates to 1972 when Fujishima and Honda discovered the generation of hydrogen and oxygen gases from the photochemical photolysis of water in the presence of TiO₂. Thereafter, researchers have been fascinated by the utilization of semiconductor catalyst materials for hydrogen production from water in oxidation reduction reactions [25]. Environmental pollutants are usually treated using semiconductor photocatalysts due to the intrinsic properties of the later; they are innocuous materials, cheap, can be modified to suit certain applications e.g. decreasing size, doping or addition of sensitizers. In addition, they provide favorable environment for multielectron transfer process and are reusable [41]. When the surface of the pollutant is irradiated with light the absorbed photon energy induces the semiconductors to generate reactive oxygen species (ROSs) namely; singlet oxygen (O₂), hydroxyl radicals (·OH), atomic oxygen (O) and hydrogen peroxide (H₂O₂) which can completely degrade pollutants in a very short time.

Meanwhile, photoexcited electrons are generated from the valence band of the semiconductor to jump to the conduction band, creating an electron/hole pair (e^-/h^+). The radiation energy needed for this mechanism should be higher than the energy difference between the conduction and valence bands called band gap. As a result, a negative electron is produced in the conduction band (e^-_{cb}) and a positive hole will be left in the valence band (h^+_{vb}). This is known as photoexcited state of the semiconductor. The photogenerated pairs (e^-/h^+) migrates to the surface of the semiconductor to participate in redox (reduction and oxidation) reactions with adsorbed species; water and oxygen. The oxygen present in the pollutants react with conduction band electron (e^-) to form a superoxide oxygen radical ($O_2^{\cdot-}$). Hole vacancies reacts with absorbed water molecules or hydroxide ions (OH^-) to form the hydroxyl radical ($\cdot OH$). The $O_2^{\cdot-}$, $\cdot OH$ and OH_2^{\cdot} radicals are responsible for the degradation of the pollutants to harmless molecules such as H_2O , CO_2 and N_2 [20,23,40,41]. As illustrated in Figure 2.1. This is known as the semiconductor metal oxide (SMO) photocatalysis mechanism.

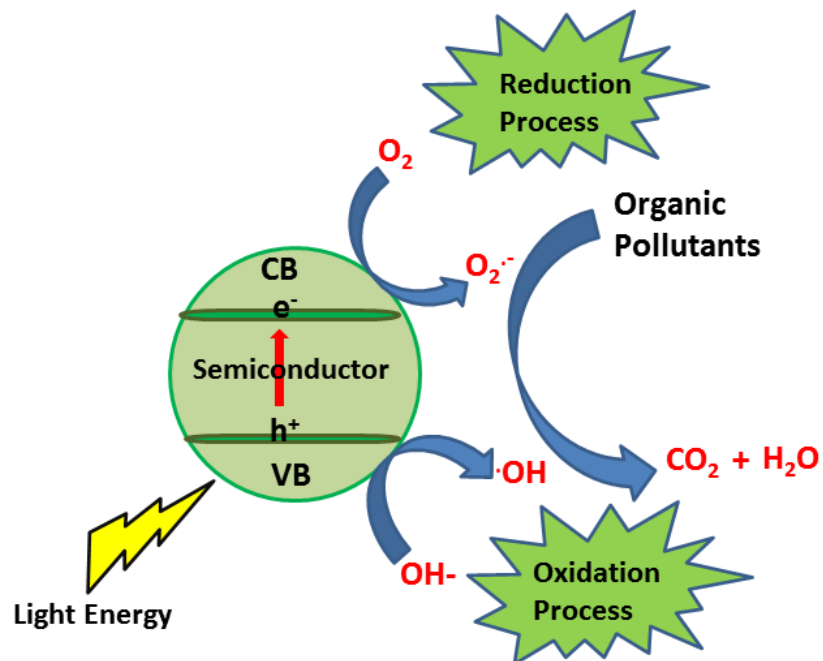


Figure 2.1: Mechanism for SMO photocatalysis.

Several studies [9,21,26,42] have been conducted for the degradation of different pollutants using numerous metal oxides such as molybdate (MoO_4), tungstate (WO_3), titanium dioxide (TiO_2), vanadate (VO_4), copper oxide (CuO), zinc oxide (ZnO), tin oxide (SnO_2), iron(III) oxide (Fe_2O_3) etc. The applications of metal oxides are displayed in Figure 2.2.

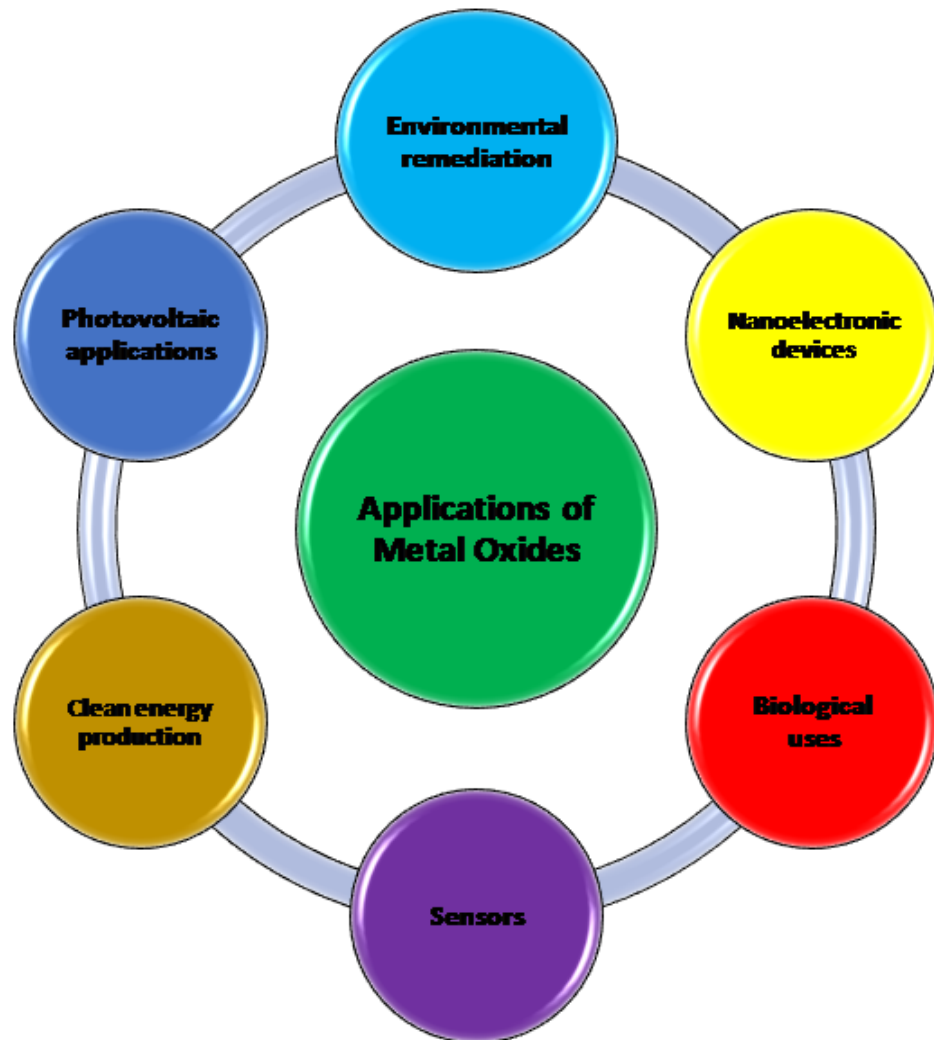


Figure 2.2: Applications of Metal Oxides.

Efforts have been made to improve the photocatalytic efficiency of semiconductors, these include coupling a semiconductor of a wide band gap with a narrow band gap semiconductor to form heterojunction composite. This method improves the photoresponse of the semiconductor in the visible light region, improves the photocatalytic activity of the semiconductor by increasing the photogenerated charge

carriers separation efficiency. The heterojunction of Ag_2CrO_4 based composites such as $\text{ZnO}/\text{Ag}_3\text{VO}_4/\text{Ag}_2\text{CrO}_4$ [43], $\text{AgBr}/\text{Ag}_2\text{CrO}_4$ [44], $\text{GO}/\text{Ag}_2\text{CrO}_4$ [45], $\text{ZnO}/\text{Ag}_2\text{CrO}_4$ [46] were reported to have improved the photocatalytic performance of Ag_2CrO_4 for the degradation of organic pollutants under sunlight irradiation.

Transition metal oxides have been extensively used in degradation of organic and inorganic dyes because they are inexpensive as compared to metal catalysts like platinum and palladium etc. Previous studies [47,48] explored improving the photocatalytic performance of semiconductors in the visible region through doping with transition metals such as Ag, Co, Mn, Cu, Pt, Fe, Ni, V, Mo, Cr, Zr, Zn, Au, Fe, Nb etc. Doping with transition metals modified the electronic structure of the semiconductor, reducing its band gap and consequently extending its light absorption edge from UV to visible light region. Guan et al [49] studied the photocatalytic activity of porous nickel doped titanium dioxide NPs synthesized through green hydrothermal route. The photocatalytic activity of transition metal doped semiconductor was investigated through the degradation of methylene blue. The results revealed that doping TiO_2 with Ni improved its photocatalytic performance under visible light. This was achieved through modification of the band gap with impurity bands.

TiO_2 and ZnO have been extensively studied [21,50,51] as photocatalysts for the degradation of various contaminants. They have gained research interest due to their non-toxic nature, wide band gap, inexpensiveness, excellent photocatalytic activity and long-term stability. Even though TiO_2 has been extensively studied for photocatalytic activities, there have been some limitations associated with its use. It has been a challenge to extend the photocatalytic response of TiO_2 in the visible region [25]. Although efforts were made to modify TiO_2 structure by doping with transition metals its photocatalytic activity in the visible region remains low. Therefore, ZnO has been chosen as a better photocatalyst. ZnO has higher electron mobility than TiO_2 [22]. Its photo-response in the visible region is higher leading to enhanced photocatalytic performance. Therefore, research activities nowadays are more focused on the

background of ZnO, its properties for better understanding of its photocatalytic performance.

2.1.1 Background Information on ZnO

ZnO is one of the fascinating metal-oxide-based semiconductors belonging to the group II-IV of the periodic table. ZnO is one of the semiconductors whose covalence is at the borderline between covalent and ionic semiconductors [52]. It is an n-type semiconductor. ZnO has three different crystal structures namely; cubic rock-salt, cubic zinc blende and hexagonal wurtzite as schematically shown in Figure 2.3. The shaded black and grey spheres symbolize O and Zn atoms, respectively. The rocksalt structure can be created under high pressure thus making it scarce, while the cubic zinc blende structure of ZnO is stable by growth on cubic substrates [18]. The most common structure of ZnO is hexagonal wurtzite as it crystallizes to this form under ambient conditions [53]. The wurtzite structure comprises of a hexagonal unit cell with three lattice parameters $a = b = 3.2495 \text{ \AA}$ and $c = 5.2069 \text{ \AA}$ with melting point $1975 \text{ }^\circ\text{C}$ and density of 5.605 gcm^{-3} .

ZnO is a promising metal oxide for quite a number of applications due to its intrinsic properties including outstanding optoelectronic and piezoelectric properties [21]. It has amazing physical and chemical properties including wide band gap of 3.37eV [54,55], high exciton binding energy of 60 meV at room temperature. Besides its non-toxicity, ZnO exhibits high chemical or thermal stability and biocompatibility [56]. It is the most promising material for a wide range of electronic and optoelectronic applications including solar cells, sensors, photocatalysis, field-emission devices, supercapacitors, ultra-violet laser diodes etc. [21].

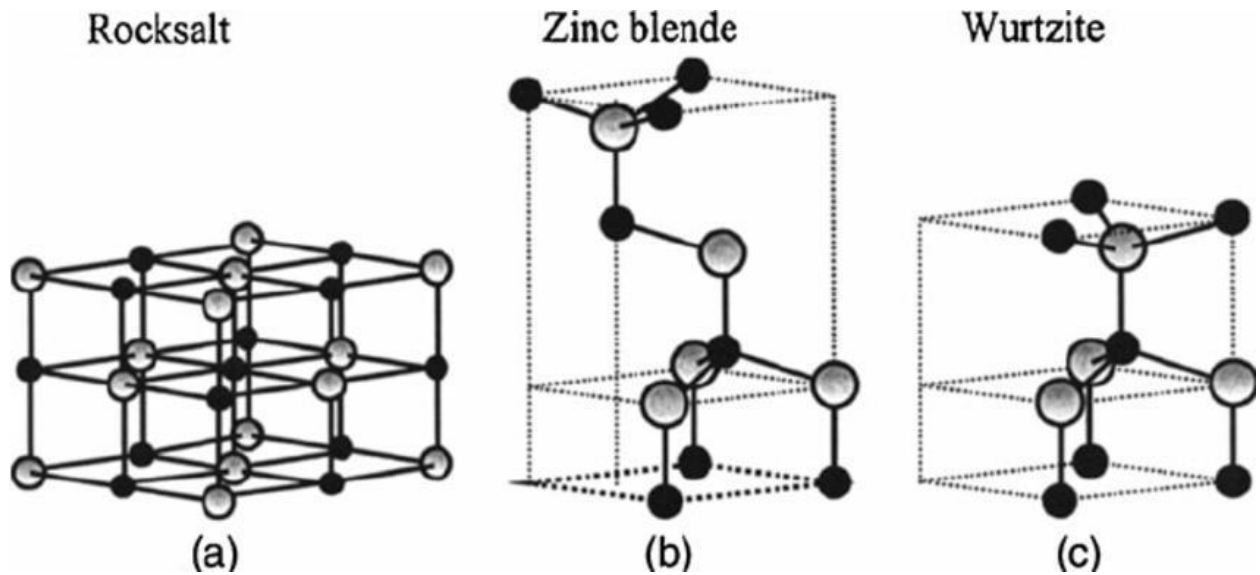


Figure 2.3: ZnO crystal structures a) cubic rocksalt b) cubic zinc blende c) hexagonal wurtzite [57].

2.1.2 Synthesis of ZnO

The structural and morphological properties of ZnO nanostructures depends on their fabrication methods. The emerging nanotechnology has provided insights for the engineering of ZnO nanostructures with different morphologies to improve their performance for various applications, hence biological, chemical and physical synthetic routes have been adopted. The preparation methods including pulse laser deposition (PLD), chemical vapor deposition (CVD), molecular beam epitaxy (MBE) and electro-chemical deposition have been used to grow ZnO nanostructures directly onto substrate [58]. In addition, some includes; sol-gel, hydrothermal, microwave assisted synthesis, spray pyrolysis and precipitation [59]. The vast range of fabrication methods of nanostructures yields different ZnO nanostructures with the desired morphology and composition of various shapes such as nanorods, nanocombs [58], nanocages, nanowires, nanobelts, nanorings, nanodiscs, nanopencils, nanoflowers, nanospheres etc. [60]. The synthetic methods that includes vapor phase process require high

vacuum and high temperatures [61]. The chemical methods utilize organic solvents as reducing agents which are toxic thus contributing to environmental pollution. Therefore, green synthetic method was developed due to its amazing advantages such as environmental benign, requires biogenic processes, cost-effective and no by-products produced.

2.1.3 Green Synthesis of ZnO

Many researchers nowadays are focused on the biological synthesis of nanomaterials due to its intrinsic advantages as already stated. The green synthetic route employs the use of living organisms for the fabrication of metal and metal oxide NPs [62]. Research activities are more interested in the use of plant extracts for the green synthesis of nanomaterials due to the abundance of biomass. The plants that are of great choice for biosynthesis of nanomaterials are the ones that are capable of detoxification and heavy metal accumulation. Furthermore, plant extracts are easily available and safe to handle. The major limitations associated with the green synthetic route includes lengthy reaction times, need for purification and impoverished understanding of the responsible mechanisms [63]. The biological synthesis of metal and metal oxide NPs involves the use of different plant parts such as seeds, flowers, leaves, barks, roots, fruits, vegetable waste and peels. Moreover, the green synthetic route utilizes universal solvent like water as a reducing medium with the help of harmless and biodegradable plant extracts.

The biosynthesis of nanomaterials employs the use of plant extracts which can act as reducing and capping agents in fabrication of NPs. Plant extracts contain biomolecules that are responsible for the reduction of metal ions such as amino acids, phenolics, alkaloids, proteins, enzymes, saponins, polysaccharides, vitamins, tannins and terpenoids, which are environmentally innocuous but chemically complex [7,64]. It was

suggested that metal ion reduction can be achieved with the assistance of quinones and plastoquinone molecules contained in the plant leaf extract [8] revealing biomolecules and heterocyclic compounds in plants are responsible for synthesis of NPs. In addition, oxygen released from the atmosphere or degrading phytochemicals connects the reduced metal ions. NPs are formed through electrostatic attraction between metal oxide ions. It has been reported [1,8] that quinones can be activated through moderate warming accompanied by subsequent incubation resulting in diminishing of particle size.

The green synthesized NPs from plants differ in size and shape as opposed to those produced by other organisms. Scientists are more interested in the biosynthesis of NPs using plants than other living organisms like fungi and bacteria since they demand prolonged incubation time for the reduction of metal ions compared to water soluble phytochemicals which take lesser time. A typical biosynthesis of NPs using plant extracts is conducted in the presence of metal salts as indicated in Figure 2.4. The natural extracts that have been used for the biosynthesis of ZnO NPs include different plant sources such as *Moringa Oleifera*, *Ageratum Houstonianum*, *Solanum torvum*, *Tecoma castanifolia* and as listed in Table 2.1 etc. It is clear that green synthesis of ZnO NPs using plant extracts is a hot topic. The *A. Houstonianum* used in this study is an environmental weed belonging to the Asteraceae family.

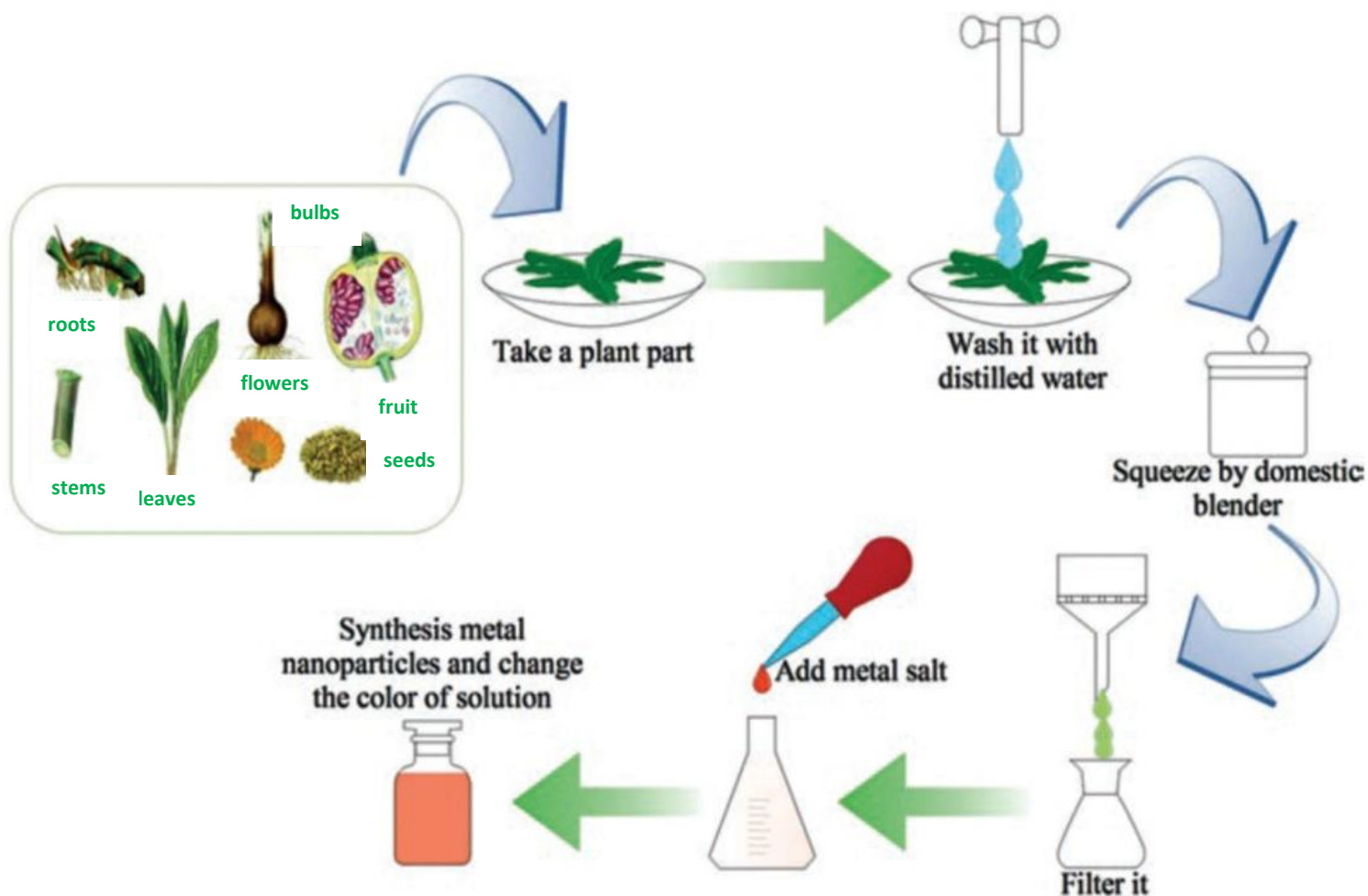


Figure 2.4: Synthetic scheme for the green synthesis of NPs from plant extract [65].

2.1.3.1 Background Information on *Ageratum Houstonianum*

It has been reported [66,67] that several plants belonging to the Asteraceae family contain a lot of secondary metabolites with biological activity. These secondary metabolites include lipids, saponins, phenolics, carbohydrates, terpenes and alkaloids. Several studies [68-71] have been conducted on some of Asteraceae plants such as *Vernonia sp*, *Achillea sp*, *Ageratum sp*, *Eupatorium sp* for fabrication of NPs. *Ageratum sp* has commonly been used as antidiarrheal, in wound and skin diseases, for the treatment of ophthalmia and leprosy [72]. They are also used in nursing pneumonia by

massaging them on the body of the patient. It is reported that this weed contains biomolecules such as phenolics, tannins and flavonoids which play a major role in the formation of NPs. *A. Houstonianum* weed is shown in Figure 2.5.



Figure 2.5: A picture of *A. Houstonianum* weed.

Table 2.1 : Green synthesis of ZnO NPs by different researchers using plant extracts.

Plant	Size of NPs (nm)	Plant part	Shape on NPs	Reference
Moringa oleifera	13-28 and 32-61	leaves	Small rods	[73]
Aspalathus linearis	1-8.5	flowers	Quasi-spherical	[61]
Cassia fistula	68.1	leaves	Spherical	[74]
Agathosma betulina	12-26	leaves	Quasi-spherical	[75]

Solanum torvum	34-40	leaves	Nano-spheres	[76]
Tecoma castanifolia	70-75	leaves	Nano-spheres	[77]
Scadoxus multiflorus	29-33	leaves	Spherical	[78]
Glycosmis pentaphylla	32-40	leaves	Spherical	[79]
Calotropis gigantea	10	leaves	Spherical	[80]
Lippia adoensis	19.78	leaves	Spherical	[81]
Sesbania grandiflora	15-35	leaves	Spherical	[82]
Mentha spicata	11-88	leaves	Spherical	[83]
Orange	200-230	fruit peels	Spherical	[84]
Jacaranda mimosifolia	2-4	flowers	Spherical	[85]
Nyctanthes arbor- tristis	12-32	flowers	Spherical	[86]
Terminalia chebula	9.6-25.5	fruits	Nano-spherical	[87]
Scutellaria baicalensis	50	roots	Spherical	[88]
Veronica multifida	10-100	leaves	Quasi-spherical	[89]
Phyllanthus embilica	15-25	stem	Nano-spheres	[90]

2.1.4 Enhancing Photocatalytic Activity of ZnO Nanoparticles

Solar energy is an abundant energy source thus photodegradation of pollutants using visible light is economically feasible. Photocatalytic research activities are focused on reducing the band gap of photocatalysts to utilize solar light rather than UV light for

energy saving costs. In addition, it is also crucial in photocatalytic reactions to minimize photogenerated electron-hole recombination for improved photocatalytic performance. This drawback can be minimized through ion doping [91], incorporation of electron-accepting materials and noble metal loading [22] and use of coupled semiconductors. Studies have been conducted on doping with rare earth ions and the results indicated that they improved the photocatalytic performance of semiconductors. Meshrametal [92] studied the photocatalytic performance of cerium doped ZnO which exhibited higher photocatalytic performance than pristine ZnO, even though the experiments were conducted under the same conditions. Therefore, Ce improved the photocatalytic activity of ZnO.

The photocatalytic performance of semiconductors also depends on surface area. An increase in surface area provides more active surface sites hence increasing the photocatalytic activity. Photocatalysis occurs on the surface of the catalyst making surface area crucial for enhanced mechanism. Good supporting materials like carbon-based materials can be incorporated with ZnO for enhanced photocatalytic activities. Carbon-based materials such as graphene oxide (GO) [93], activated carbon [94], reduced graphene oxide (RGO) [95], carbon dots [96] and graphene [97] have been reported to have improved the photocatalytic efficiency of ZnO. Carbon materials mobilize easy charge transfer between the pollutant molecules and metal oxides due to their high electronic conductivity. They minimize photogenerated electron-hole recombination. They also reduce agglomeration of NPs allowing more light to reach the active surface sites.

Previous researchers, Beura et al [24] studied the structural, optical and photocatalytic properties of graphene/ZnO nanocomposite. The photocatalytic performance of graphene/ ZnO nanocomposite was studied through the degradation of methyl orange under UV light. It was concluded that graphene/ZnO nanocomposite had higher photocatalytic performance than pure ZnO. It is reported that even though ZnO is the

best semiconductor metal oxide for photocatalytic activities it suffers from recombination of photogenerated electron-hole pairs leading to lower quantum yield. Incorporation of graphene with ZnO reduces the rate of recombination of the charge carriers and increases the surface area of the material, exposing more active sites, and more of the organic pollutant to be adsorbed on the surface of the nanocomposite hence improved dye degradation. Graphene is considered a significant carbon-based material due to its amazing properties.

2.2 Background Information on Graphene

Graphene is a two-dimensional carbon-based material in the form of single layer hexagonal lattice of sp^2 bonded carbon atoms [98,99]. It has been the most studied carbon-based material in both scientific and engineering research since its discovery in 2004 by Andre Geim and Konstantia Novoselov at the University of Manchester [100]. Consequently, the pair were awarded the Nobel prize in Physics in 2010 for innovative research with respect to two-dimensional material, graphene. Graphene is a building block for other graphitic materials. It can be folded into 0-dimensional fullerenes, rotated into 1-dimensional carbon nanotubes and piled into 3-dimensional graphite as illustrated in Figure 2.6.

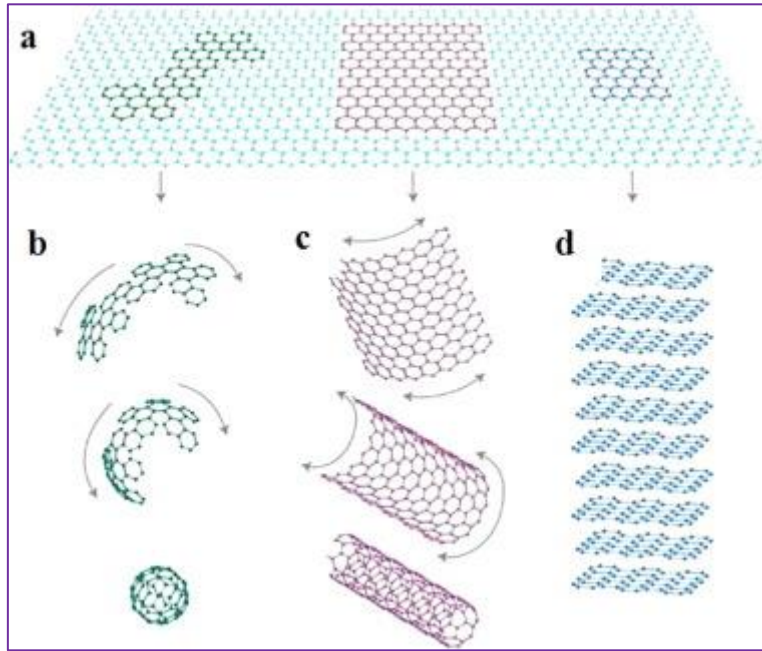


Figure 2.6: Allotropes of carbon: a) 2-D graphene, b) 0-D fullerene, c) 1-D carbon nanotube, d) 3-D graphite [101].

The properties of graphene can be changed into those of graphite through increasing the number of graphene layers. Previous studies revealed that if graphene layers exceed ten then the material is recognized as graphite. A single layer graphene is shortened as 1LG, few-layered as FLG, multilayer (MLG) and bilayer graphene is abbreviated as 2LG. The distinctive structure of graphene permits it to have numerous unusual and interesting properties such as excellent thermal conductivity, quantum hall effect (QHE), remarkable mechanical flexibility, high charge mobility, outstanding optical properties and large specific surface area [97,102]. These properties make it a versatile material for quite a number of applications including quantum physics [103], electronics, electrochemistry, optics [99], energy storage, sensor, medicine, single molecule gas detection and catalysis [31]. Since the properties of graphene rely on the synthetic route various methods were explored for the fabrication of graphene.

2.2.1 Synthesis of Graphene

Graphene can be fabricated using various methods such as epitaxial growth, chemical vapor deposition (CVD) [98], micromechanical exfoliation of graphite [104], and reduction of graphene oxide [105]. Various factors from the preparation method influence the graphene thickness and quality such as growth temperature, the growth period, cooling rate after the growth period and the methane (CH₄) concentration [106]. Furthermore, one of the contributing parameters of number of graphene layers in the CVD method is the flow of a reactive gas, CH₄. These methods have some drawbacks, they are not ideal for large-scale production. Chemical synthesis involves the use of complicated chemical synthetic techniques and highly harmful chemicals which are not environmentally friendly. The epitaxial growth method produces large sized graphene on wafers, the fabrication of graphene from this method is quite expensive due to the price of the substrate silicon carbide (SiC) [98]. In addition, pyrolysis has been a common method for the synthesis of graphene on metal surfaces from various carbon sources or other activated carbons [104]. Nevertheless, employing surface growth for synthesis of graphene produces small yield. Therefore, researchers have been focused on developing cheap sustainable techniques for fabrication of graphene from natural sources [12].

2.2.2 Green Synthesis of Graphene

Green synthesis of graphene involves the use of plant extracts, microorganisms or waste biomass as eco-friendly reducing agents. The use of microorganisms can be unmanageable due to the aseptic conditions they need for their growth. As already mentioned in section 2.1.3 plant extracts contain distinct polyphenols which acts as reducing and capping agents during fabrication of NPs. During reduction of GO, the polyphenols can be converted to their quinone forms to act as reducing agents [107]. The polyphenols are also responsible for functionalization of RGO sheets produced. Graphene can also be produced through a feasible and eco-friendly technique by

thermal pyrolysis of biomass. This method guarantees large scale production of graphene [104].

Waste biomass have gained much attention due to their abundance, sufficient sources of carbon and need for recycling. Disposing waste biomass has always been a challenge in towns and cities, therefore converting them to valuable materials like graphene contributes towards environmental remediation. The biomass and waste materials that can be utilized to produce graphene includes plant parts, wood waste, agricultural waste and food etc. Biomass from plant waste are mostly composed of cellulose, hemicellulose and lignin [108]. Cellulose is a semi crystalline polymer with amorphous and crystalline sections in different quantities depending on the nature of the plant. A lower molecular weight, amorphous biopolymer is called hemicellulose [109]. The formation of microfibrils is through binding bundles of cellulose fibrils, furthermore, crosslinked with lignin. Lignin is a macro molecule, comprising of aliphatic and aromatic constituents. Its structure comprises of three-dimensional shuffled network and are extremely complex.

Several studies [110-114] have been reported on the extraction of cellulose nanocrystals (CNCs) from a wide range of natural sources such as agricultural wastes (e.g. mango seed, pineapple leaf, rice husk, mulberry bark and corn husk). CNCs can be prepared through numerous extraction processes including hydrochloric and sulfuric acid hydrolysis. Alkali treatments can be used to dissolve hemicellulose and lignin. The step-by-step process for extraction of cellulose is as displayed in Figure 2.7.

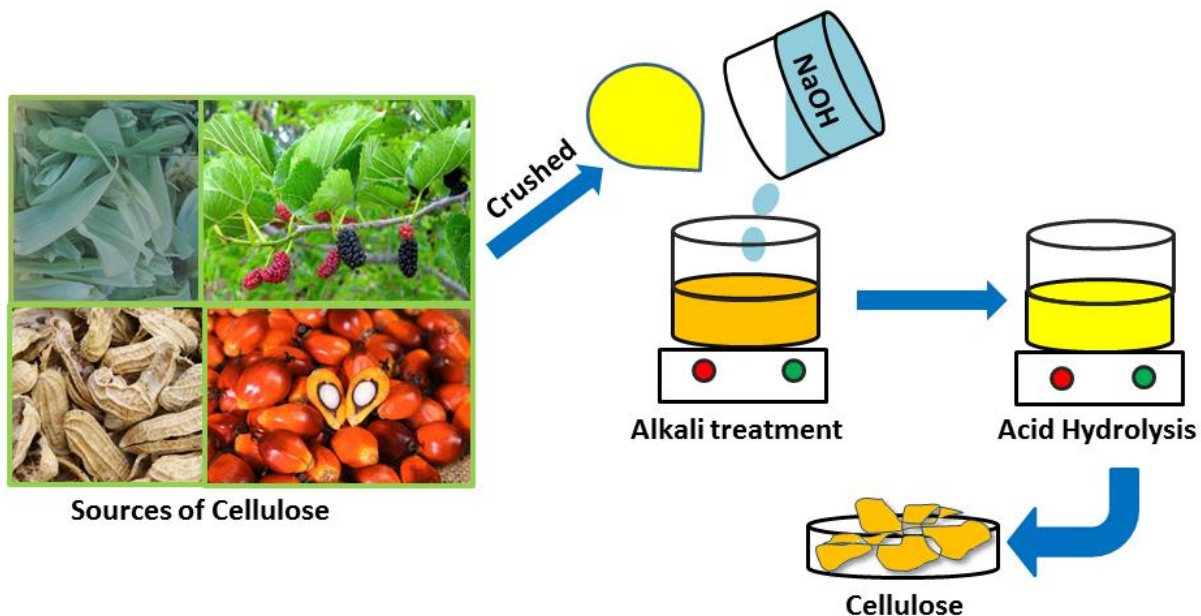


Figure 2.7: Typical schematic diagram for extraction of cellulose.

The major waste from corn production after harvesting is corn husk, cobs and corn stover such as stalk and leaves. Corn husk is comprised of cellulose (about 42%), lignin (approximately 13%), ash (4%) and 41% of extra material [115]. Usually corn husks are disposed through burning but this poses a threat to the environment and health system. Moreover, burning of corn husk is more polluting than thermal pyrolysis of biomass. Therefore, it is crucial to develop scientific methods for recycling corn husk. Graphene can be synthesized using waste biomass (Corn husk) via alkali treatment and acid hydrolysis to extract cellulose. This synthetic route includes thermal pyrolysis of biomass.

Purkait et al [12] synthesized FLG from waste peanut shells via simple activation by potassium hydroxide (KOH) accompanied by mechanical exfoliation. Their synthetic route involves thermal pyrolysis of the biomass. Shams et al [104] prepared FLG by thermal pyrolysis of biomass; camphor leaves. The camphor leaves were heated at 1200 °C at 10 °C/min for 4 min and the sample was cooled down to room temperature.

They further reported that D-Tyrosine and centrifugation assisted in separation of FLG from the final pyrolytic components. Zang et al [116] fabricated TiO₂-pillared multilayer graphene nanocomposite via a facile method that involves dodecanediamine pre-pillaring, ion exchange and interlayer *in-situ* synthesis of TiO₂ by hydrothermal method.

As already mentioned, applications of graphene include catalysis, it can be utilized in various catalytic reactions such as air purification, selective hydrogenation, oxygen reduction, NO_x abatement and wastewater treatment [100]. Graphene has been extensively used in photocatalysis due to its intrinsic properties. Researchers nowadays are more focused on the fabrication of semiconductor/graphene composite for improved photocatalytic efficiency of the nanocomposite. Previous studies [18,20,22,24] reveal that graphene-based composites possess amazing properties that include; efficient charge transportation, enhanced adsorption of pollutants, increased light absorption range and separation. Fabrication of graphene/ZnO nanocomposite improves the photocatalytic performance of ZnO. This is supported by previous researchers as illustrated in Table 2.2.

Water contamination has increased of late due to the release of huge quantities of pollutants from industries into aquatic environments which may affect plants and animals. These contaminants include pharmaceuticals and dyes from textile, printing, dyeing and food industry. Selvin et al [117] states that a variety of dyes exists based on their chromophore structures; azo, diazo, anthraquinone, xanthene, disperse, acidic and basic dyes. They can also be divided into cationic, anionic and non-ionic dyes. RhB is one of the extensively used cationic xanthene dyes in industries. This dye is toxic and causes irritation to skin, eyes and respiratory tract [118]. It is also carcinogenic and causes chronic toxicity to humans and animals, hence waste waters that contain it should be treated first before distribution. CR is an anionic diazo dye, commonly used in silk cloth manufacturing industries. The removal of CR from the environment has always been a major concern

worldwide. These dyes lead to massive environmental problems due to their good stability. Graphene/ZnO nanocomposite can be used to completely degrade different pollutants including organic dyes such as BB, RhB, CR and common antibiotics like DOX. BB is one of the extensively used azo dyes in industry which is extremely stable and stubborn to degrade.

As already indicated, another major source of environmental contamination is from drugs detected in ground water, surface water and wastewater that is discharged from households and municipal or industries. The rise in the contamination from drugs is due to the improper disposal of expired drugs, the rural effluents and the antibiotics found in animal manure. Borghi et al [17] indicated that the increase in the use of antibiotics contributes to their release into the environment as metabolites or in their original form. Moreover, multidrug resistance is a major concern in the treatment of contagious diseases. The extensive use of broad-spectrum antibiotics resulted in resistance to traditional antimicrobial agents for numerous bacterial human pathogens [119]. This has caused so many challenges in the health system. For example, DOX is a commonly used broad-spectrum tetracycline antibiotic which is used to cure many bacterial infections by hindering the bacterial protein fabrication [120]. It is used to cure risky diseases such as bubonic plague and anthrax. Therefore, it is of great importance to avoid DOX from entering the environment, since it can lead to increase in resistant bacteria and reduced efficacy of DOX in humans. As a contribution to mitigation efforts this study focused on the use of effective green methods for the synthesis of materials (MLG/ZnO nanocomposite) for the degradation of dyes and DOX under visible light and UV irradiation.

Table 2.2: Summary of experiments conducted on carbon-based nanocomposites for photocatalytic applications.

Photocatalyst	Preparation Method	Results	Reference
ZnO-Graphene	Dry mechanochemical	ZnO-Graphene nanocomposite revealed a superior photocatalytic performance as compared to pure ZnO	[97]
ZnO-Graphene	Hydrothermal	ZnO-Graphene composite exhibited higher photocatalytic efficiency than pristine ZnO	[29]
Porous graphene/ZnO nanocomposite	Fine tuning of combustion	PG/ZnO gave 69.2% degradation of total organic carbon (TOC) within 210 min while ZnO removed 44.8% TOC under the same conditions	[30]
ZnO/graphene-oxide	Chemical deposition route	ZnO/GO nanocomposite exhibits higher photocatalytic efficiency of 98% in degradation of Methylene blue MB after 60 min of visible light irradiation while ZnO removed only 54.3% of MB within 100 min of irradiation	[22]
ZnO/graphene flake-like	Facile in-situ hydrolysis-deposition route	ZnO/graphene revealed the highest photocatalytic performance than pure ZnO	[121]

The next chapter gives a description of the materials and methods used for the synthesis, characterization and analysis of MLG/ZnO nanocomposite.

CHAPTER 3: METHODOLOGY

3.0 INTRODUCTION

This study focused on recycling waste biomass materials to synthesize MLG due to their abundance and ample sources of carbon. This chapter describes all the materials and methods used for the preparation of MLG/ZnO nanocomposite. It outlines all the procedures for photocatalytic evaluation of the photocatalysts for the degradation of organic dyes and pharmaceuticals. It also outlines the techniques used for the characterization of the synthesized samples.

3.1 Materials and Methods

All reagents were purchased from Sigma Aldrich, Germany and were of high analytical grade hence were used as received.

3.1.1 Green Synthesis of Multilayer Graphene from Waste Biomass

MLG was synthesized using corn husk as a waste biomass. Corn husk was chosen in this study due to its ample supply and is an ideal biowaste to generate carbon nanomaterials.

The following reagents/materials were used for the successful synthesis of MLG:

- Fresh corn husk collected from nearby local farms, Palapye, Botswana
- Deionized water
- Ethanol, 99.99% purity
- Sodium hydroxide (NaOH) salt, 99.99% purity
- Hydrochloric acid (HCl), 32% purity

- Isopropanol, 99.5% purity
- Potassium hydroxide (KOH), 99.99% purity
- Sulfuric acid (H₂SO₄), 97% purity

3.1.1.1 Extraction of Cellulose from Corn Husk

The collected corn husks were washed with deionized water to remove soil and other impurities, then dried overnight in an oven at 80 °C. A ball mill was used to crush the cleaned husks. The resultant powder was passed through 40 mesh sieves to obtain the finest particles and stored at room temperature. Previously reported methods were adopted to remove non-cellulosic materials from corn husk powder [113,122,123]. The obtained powder was soaked in ethanol for 24 h to remove wax and other impurities. It was then treated with 4% weight per weight (w/w) sodium hydroxide at 80 °C for 2 h to eliminate hemicellulose and lignin and also increase the accessible surface area [108]. The solid was then filtered and washed several times with deionized water. Acid hydrolysis was conducted after alkali treatment using 30% w/w hydrochloric acid at 45 °C for 1 h to dissolve residual hemicellulose. The cellulose was filtered and washed several times with deionized water to remove chemicals and air-dried overnight. The step-by-step diagram for the extraction of cellulose is shown in Figure 3.1.

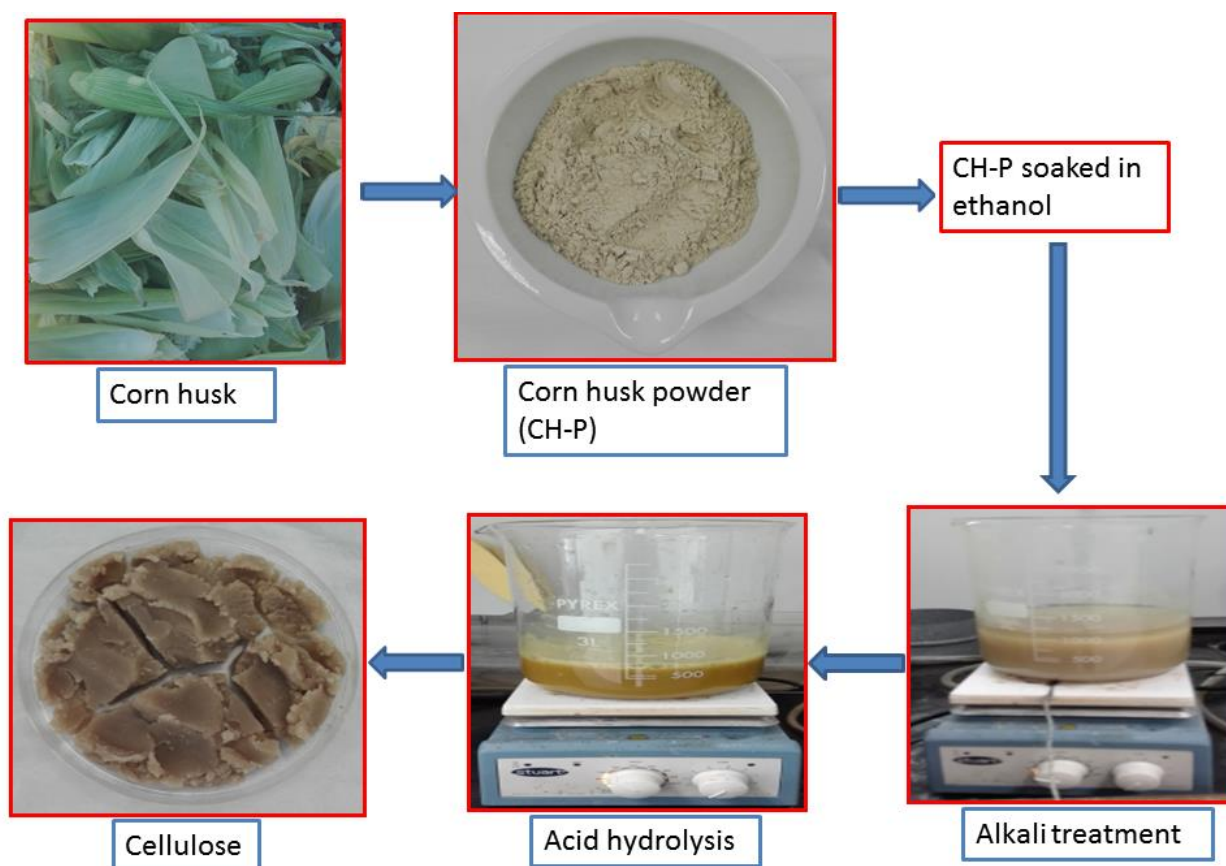


Figure 3.1: Schematic plan for extraction of cellulose.

3.1.1.2 Synthesis of Multilayer Graphene using Cellulose from Corn Husk

Procedures from previous studies were adopted to synthesize MLG using waste biomass [12]. The extracted cellulose was pyrolyzed at 800 °C for 2 h under nitrogen atmosphere. The collected material was named corn husk-carbonized material (CH-C). The carbonized material of mass 4.58 g was collected and washed with 50 mL isopropanol to remove the unwanted organic material. CH-C material was homogeneously mixed with potassium hydroxide (KOH) (w/w 1:3) using mortar-pestle for the potassium to tear apart the layers between carbons. The homogeneous mixture was repyrolyzed under the same conditions for 2 h to activate the carbon material. The corn husk activated carbon material (CH-AC) was then washed with 1:1 HCl solution followed by deionized water to remove the excess alkaline compounds

and neutralize the pH. It was then dried overnight at 50°C.

The CH-AC sample was then treated with 10% H₂SO₄ aqueous solution through ultrasonication. The desired temperature was maintained throughout by cold water bath. The collected sample was then washed several times with isopropanol and deionized water to dissolve any residual impurities. The final product, MLG was filtered and dried overnight at 80 °C. MLG was synthesized as shown in Figure 3.2.

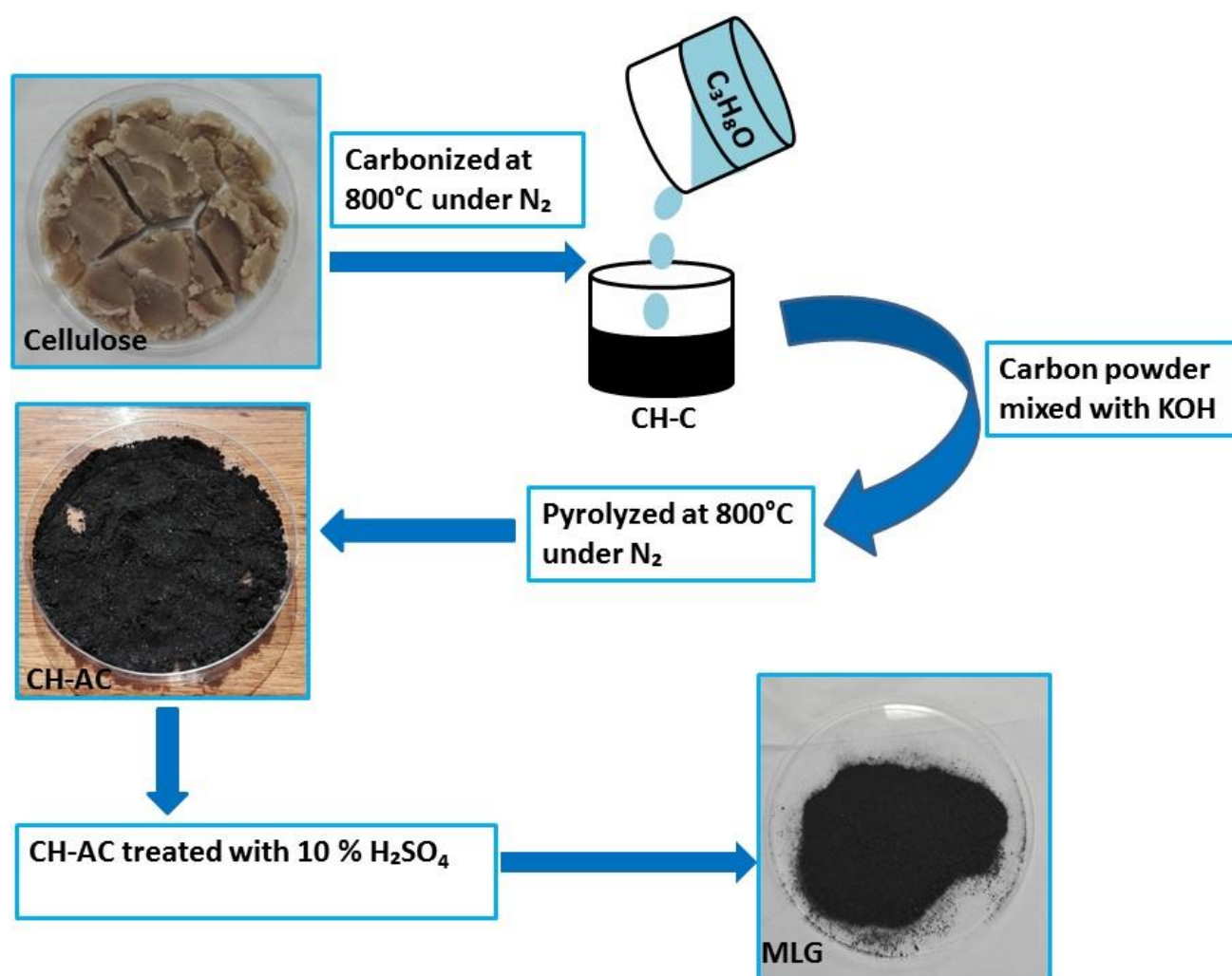


Figure 3.2: Schematic diagram for the synthesis of MLG.

3.1.2 Green Synthesis of ZnO

In this work, ZnO was synthesized using *A. Houstonianum*, a natural extract which is an efficient reduction/oxidizing agent.

The reagents used in this study include the following:

- Fresh *A. Houstonianum* leaves collected from around university campus
- Zinc nitrate hexahydrate salt, 99.99% purity
- Deionized water

3.1.2.1 Preparation of *A. Houstonianum*

The collected leaves were washed several times with deionized water to remove dust, then left in air to dry at room temperature. The leaves were then crushed using a mortar and pestle. The crushed leaves were mixed with deionized water at a volume per volume (v/v) ratio of 1:2 (424.87 g: 849.74 mL). The mixture was stirred for 24 h to fully extract the plant sap. The green plant extract was filtered with Whatman filter paper of diameter 90 mm and pore size 0.2 μm and centrifuged at 4200 rev/min to collect the liquid. The prepared leaf extract is displayed in Figure 3.3.



Figure 3.3: Prepared leaf extract.

3.1.2.2 Preparation of ZnO NPs

The synthesis of ZnO NPs was done by simple precipitation reaction process using zinc nitrate hexahydrate as a zinc source. 876 mL of 0.1M $\text{Zn}(\text{NO}_3)_2 \cdot 6\text{H}_2\text{O}$ solution was prepared. The following parameters were used.

- Volume of deionized water: 876mL
- Mass of $\text{Zn}(\text{NO}_3)_2 \cdot 6\text{H}_2\text{O}$ dissolved: 26.06g
- Concentration of $\text{Zn}(\text{NO}_3)_2 \cdot 6\text{H}_2\text{O}$: 0.1M

Zinc nitrate hexahydrate ($\text{Zn}(\text{NO}_3)_2 \cdot 6\text{H}_2\text{O}$) was dissolved in deionized water, the solution was heated at 60 °C under constant magnetic stirring for 30 min. The plant extract and the zinc nitrate solution were mixed at a v/v of 1:1. The mixture was stirred for 1 h while maintaining the same temperature. A precipitate was observed. The precipitate was heated in an oven at 60 °C for 5 h. The mixture was then centrifuged to collect the precipitate, which was then washed several times with deionized water to remove unreacted by-products. The precipitate was then dried overnight in an oven at 60 °C and calcinated in an open furnace at 700 °C for 3h to obtain highly crystalline ZnO NPs.

3.1.3 Preparation of Multilayer Graphene/Zinc Oxide (MLG/ZnO) nanocomposites

Ex-situ casting of the pre-synthesized ZnO (section 3.1.2.2) and MLG (section 3.1.1.2) were used to prepare MLG/ZnO nanocomposites

Three different ratios of MLG/ZnO nanocomposites were prepared with the ZnO content kept constant in all the composites. However, the amount of MLG was varied in all the composites as shown in Table 3.1.

Table 3.1: Preparation conditions for different ratios of MLG/ZnO nanocomposite.

Sample	MLG (mg)	ZnO (mg)
MLG/ZnO_1	75	75
MLG/ZnO_2	37.5	75
MLG/ZnO_3	25	75

The as-synthesized MLG powder was added to 100 mL deionized water, and then ultrasonically dispersed for 1 h, followed by addition of the desired amount of synthesized ZnO. Separate MLG/ZnO mixtures were stirred ultrasonically for 1 h to result in an even mixture, followed by mechanical stirring for 24 h. Finally, the mixture was centrifuged and dried overnight at 60 °C to obtain MLG/ZnO nanocomposites. Three composites of MLG/ZnO with ratios, 1:1, 1:2, 1:3 were synthesized. These samples were assigned abbreviations MLG/ZnO_1, MLG/ZnO_2 and MLG/ZnO_3 respectively.

3.2 Sample Characterization

Structural analysis was conducted by Powder X-ray Diffraction (XRD) using a Bruker D8 Advance equipped with a monochromatized Cu K α incident radiation of wavelength $\lambda = 1.54060 \text{ \AA}$. The Raman spectra were obtained using the LabRAM HR Evolution Raman Spectrometer with a laser excitation wavelength of 532 nm. The surface morphology of the samples was studied using Field Emission Scanning Electron Microscope (FESEM), (model JEOL 7100 Japan). The samples were coated with gold for SEM observation to prevent charging of surfaces. The instrument is also equipped with an Energy Dispersive Spectroscopy (EDS) for elemental analysis. The morphology of the samples was also

studied using High-Resolution Transmission Electron Microscope (HRTEM) Tecnai G2 F20 X-Twin fitted with digital micrograph software for studying Selected Area Electron Diffraction (SAED) pattern of the samples. Nitrogen adsorption (Brunauer Emmett Teller, BET) analysis was conducted in Micromeritics TriStar II 3020 version 2.00 at 77 K to obtain the specific surface area. The pore size distribution was obtained using the adsorption branch of the isotherm by Barret-Joyner-Halenda (BJH) model. The as-synthesized materials were degassed at 350 °C for 3 h. The optical absorbance of the samples was evaluated using UV-Vis spectroscopy (model Lambda 750, Perkin Elmer, USA).

3.3 Photocatalytic Assessment

3.3.1 Photocatalytic Degradation of Organic Dyes

The photocatalytic performance of the nanomaterials was investigated by studying the photodegradation of three dyes; BB, CR and RhB. 100 mL was used in the experiment for all the dyes with initial concentrations of 1.25×10^{-5} mol/L for BB, CR and RhB. It is easy to monitor the reduction in maximum characteristic absorption peak of BB hence was chosen for optimization of conditions to determine the material with higher photocatalytic efficacy. Therefore, four different photocatalysts; pristine ZnO, multilayer graphene, MLG/ZnO_1, MLG/ZnO_2 and MLG/ZnO_3 were used to degrade BB. The composite with the highest photocatalytic efficiency and pristine ZnO for comparison were further used for photocatalytic degradation of CR and RhB.

7.5 mg of the respective photocatalyst was added to 100 mL of the aqueous dye solution in labelled beakers. The mixtures were then magnetically stirred for 1 h in dark conditions to establish adsorption-desorption equilibrium between the photocatalyst and the dye solution. The solutions were then exposed to direct sunlight for irradiation (solar flux at 1000 W/m^2). The thermal effect of the sun was controlled by placing the reaction vessels in a bath sonicator with cold running water throughout

the experiment. The whole irradiation procedure was conducted for a total of 3 h. After every 30 min of irradiation, 3 mL of the solution was sampled and filtered through PES (0.05 μm) filters. The sampled solutions were analyzed for photocatalytic degradation by measuring the absorbance using a Perkin-Elmer Lambda 750 double beam spectrophotometer operating in the UV-Vis wavelength range of 200-800 nm for CR, 300-800 nm for BB and 400-700 nm for RhB. The experiments with all the three dyes were carried out under the same conditions.

3.3.2 Photocatalytic degradation of Doxycycline (a Common Antibiotic)

The photocatalytic degradation studies of a common antibiotic were conducted on DOX using MLG/ZnO₃ nanocomposite as a photocatalyst. The experiment was carried out at room temperature. 10 mg of the drug was dissolved in 100 mL of deionized water and stirred for several hours to obtain a homogeneous mixture. 400 mg of the catalyst was added to the drug solution. The mixture was then magnetically stirred in the dark for 30 min to attain the absorption-desorption equilibrium between the drug solution and the catalyst. Irradiation was carried out using a UV lamp (20 W) for 300 min under continuous stirring. The lamp was placed 5 cm away from the reactor vessel. The experiment was conducted in a dark box to exclude any external light. The solutions were sampled after every hour and analyzed as already stated.

3.4 Radical Scavenging Experiments

The main reactive species (positively charged holes and radicals) were detected through radical scavenging experiments in photocatalytic experiments. These experiments were done in order to investigate the photocatalytic mechanism of the most effective photocatalyst (MLG/ZnO₃) in degradation of all the four pollutants. The hydroxyl radical ($\cdot\text{OH}$), superoxide radical ($\text{O}_2^{\cdot-}$) and holes (h^+) were trapped by adding tert-butanol (t-BuOH) ($\cdot\text{OH}$ scavenger), p-benzoquinone (p-BQ) ($\text{O}_2^{\cdot-}$ scavenger) and Ethylenediaminetetraacetic

(EDTA) disodium salt dihydrate (h^+ scavenger) into the reaction solutions respectively. 7.5 mg of MLG/ZnO_3 and 10 mM of radical scavengers were mixed with prepared solutions of BB, CR, RhB and DOX respectively. The photocatalytic experiments on BB, CR, RhB and DOX by MLG/ZnO_3 photocatalyst were conducted parallel to the radical scavenging experiment under the same conditions as described in section 3.3.1. The percentage degradations of the dyes were then calculated to determine the main reactive species responsible for the degradation of the pollutants.

The next chapter presents the results and discussion of what have been achieved in this study.

CHAPTER 4: RESULTS AND DISCUSSION

4.1 Structural and Morphological Characterization

4.1.1 Powder X-ray Diffraction analysis

Powder X-ray Diffraction (XRD) measurements were used to identify the crystal phase as well as analyze the purity, composition and microstructure of the synthesized materials. The XRD profiles of multilayer graphene and its treatment stages (CH-C and CH-AC) are illustrated in Figure 4.1.

The (002) plane was observed at $2\theta=21.9$ and 20.7° and (100) plane at 43.3 and 43.1° for CH-C and CH-AC, respectively. The XRD peak shift of the two materials is due to structural alterations that can be introduced in the samples as a result of varied chemical activation conditions. The XRD profile of MLG exhibit two peaks at $2\theta= 21.0$ and 46.8° which correspond to (002) and (100) planes of graphene ,respectively, in agreement with previously reported findings [30,98,124]. The peak shift of the synthesized MLG from literature is due the difference in the type of precursor used and the synthetic method adopted in this study. The 002 MLG peak from other sources differs from 22° to 30° therefore the best instrument that is used to distinguish graphene from other materials is Raman relying on the 2D band from the Raman spectrum and HRTEM. The diffraction peaks matched ID number 9014004 of the 2013 COD database. The (002) peak resemble the graphitic features of the carbon materials. The observed structure for MLG was a hexagonal structure. The layer-to-layer distance and the interatomic (in-plane) distance between neighbouring carbon atoms in MLG sheets were calculated using Bragg's Law ($n\lambda=2d\sin\theta$) and were found to be $d_{002}=0.3368\text{nm}$ and $d_{100}=0.1768\text{nm}$. The graphitization degree of carbon materials can be calculated using equation (4.1).

$$G = \frac{0.3440 - d_{002}}{0.3440 - 0.3354} * 100\% \quad (4.1)$$

where 0.3440 represents the interlayer spacing of turbostratic graphite (nm), 0.3354 represents the interlayer spacing of single crystal graphite and d_{002} gives the interlayer spacing of the carbon material [98]. The calculated graphitization degree of the multilayer graphene material synthesized in this work was found to be 83.7%. This high degree of graphitization indicates its high electrical conductivity [98].

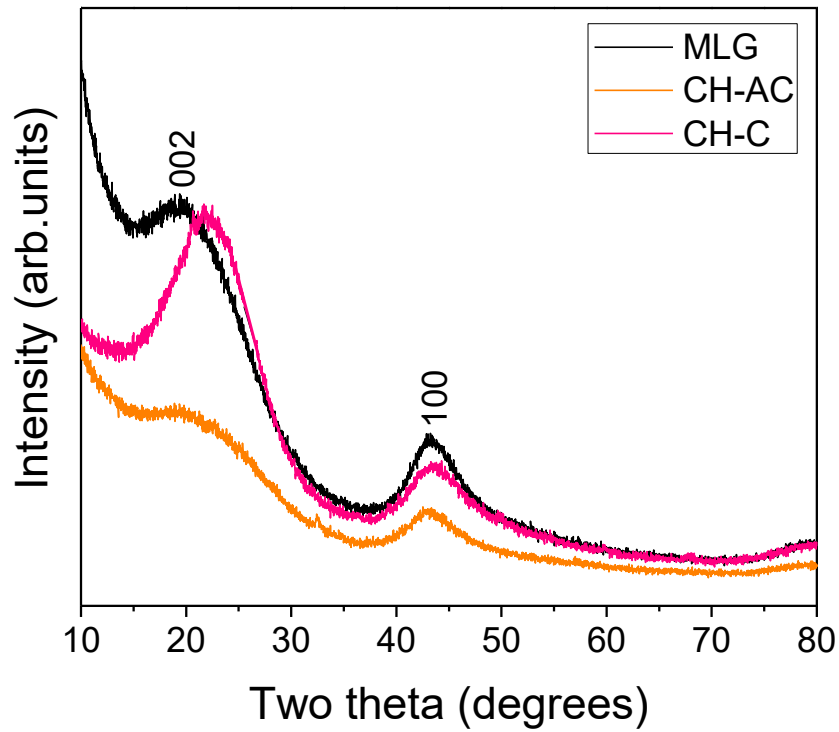


Figure 4.1: XRD patterns of MLG and its main predecessor stages (CH-C and CH-AC).

The XRD profile of ZnO and MLG/ZnO composites is illustrated in Figure 4.2. The XRD profile of the pristine ZnO shows nine Bragg diffractions. The XRD peaks observed at $2\theta=32.1, 34.8, 36.6, 48.1, 57.2, 63.6, 67.1, 68.7$ and 69.9° correspond to miller indices (100), (002), (101), (102), (110), (103), (200), (112) and (201), respectively and match

those previously reported in literature [24,61,73,75]. The obtained diffraction profiles were indexed to the hexagonal wurtzite structure of single phase ZnO in accordance with the 2013 COD database of ID number 2300114. The sharp XRD peaks indicates the crystalline nature of ZnO. The ZnO nanostructure had lattice constants $a=b=0.322$ nm and $c = 0.515$ nm.

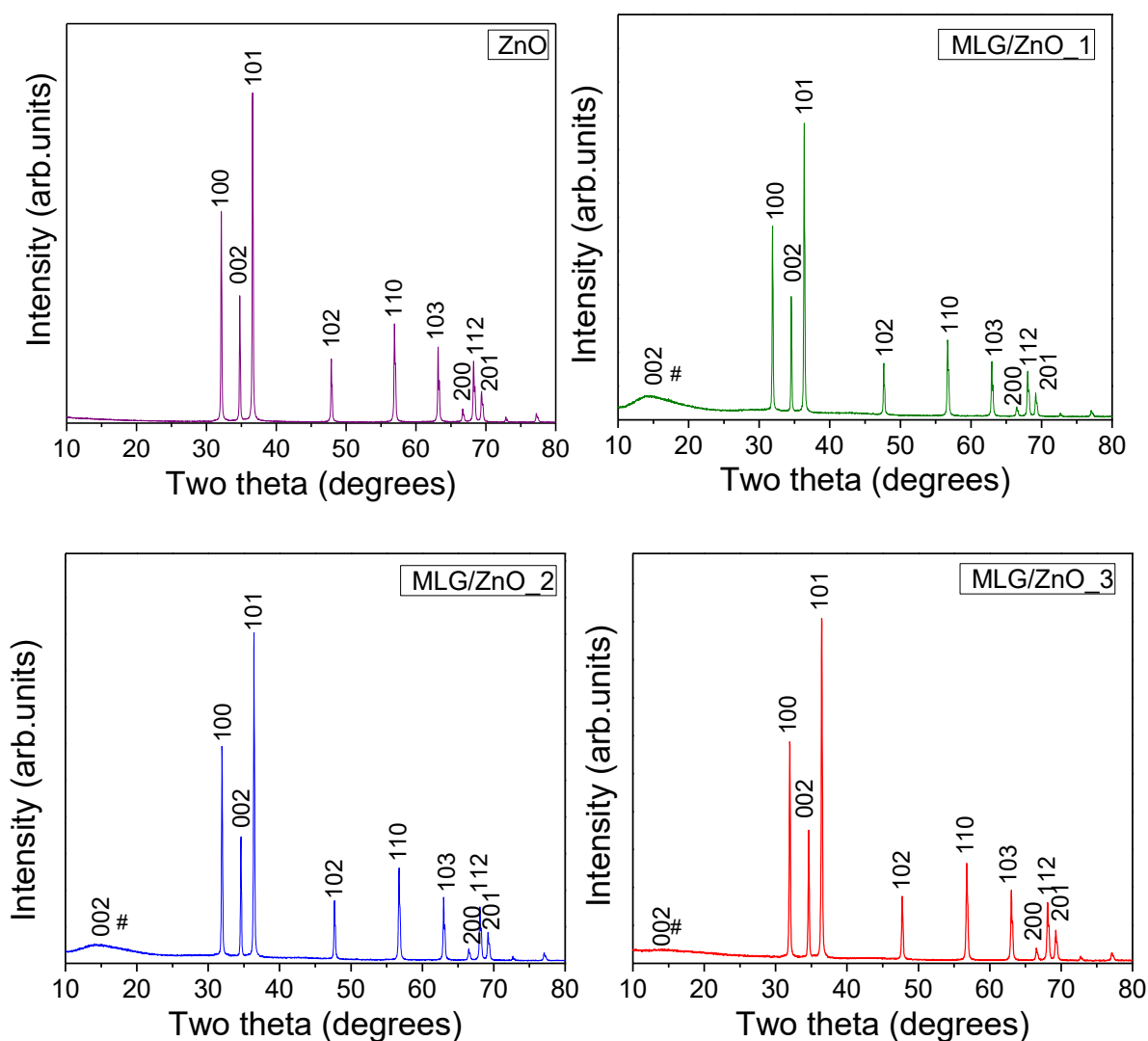


Figure 4.2: XRD patterns of ZnO and MLG/ZnO composites (# indicates the multilayer graphene peak in the composite).

The crystallographic analysis of the MLG/ZnO nanocomposites showed the presence of both MLG and ZnO. The indexed XRD peaks of MLG and ZnO corresponded to the hexagonal crystal structures. The angles shifted slightly in MLG/ZnO composites XRD patterns in comparison to pristine ZnO. The MLG and ZnO peaks were observed at almost the same angle positions in all the three MLG/ZnO composites with no impurity peaks present. Moreover, varying MLG: ZnO content ratio did not affect their structure. The presence of MLG was more evident in the MLG/ZnO_1 sample as it contained more MLG content than other nanocomposites. As expected an increase in the amount of ZnO led to a decrease in the relative intensity of multilayer graphene peaks relative to ZnO as also reported in literature [24]. The lattice parameters slightly increased in the composites with respect to those of pure ZnO. This indicates the stretching of unit cells. The lattice parameters for all the three composites were equal as shown in Table 4.1.

Miller indices (hkl) of the as-synthesized materials were used to find the crystallographic planes of the unit cell. Since the observed structures of ZnO and MLG had a hexagonal structure, equation (4.2) was used to calculate the lattice parameters (a, b and c) of the synthesized materials.

$$\frac{1}{d^2} = \frac{4}{3} \left(\frac{h^2 + hk + l^2}{a^2} \right) + \frac{l^2}{c^2} \quad (4.2)$$

The unit volume of ZnO in each sample containing ZnO was calculated using equation 4.3

$$V = \frac{\sqrt{3}a^2c}{2} \quad (4.3)$$

The lattice parameters, COD values, lattice constants and unit volume values of samples containing ZnO are presented in Table 4.1.

Table 4.1: Crystal lattice parameters and unit volume of ZnO and ZnO in MLG/ZnO nanocomposites determined from XRD analysis.

Sample	COD No	a=b (nm)	c (nm)	c/a (nm)	Vol (nm ³)
ZnO	2300114	0.3219	0.5149	1.5996	0.0462
MLG/ZnO_1	2300113	0.3234	0.5177	1.6008	0.0469
MLG/ZnO_2	2300113	0.3234	0.5177	1.6008	0.0469
MLG/ZnO_3	2300113	0.3234	0.5177	1.6008	0.0469

The average crystallite size of all the samples was calculated using the Scherrer equation [113,125,126]:

$$D = \frac{K\lambda}{\beta \cos\theta} \quad (4.4)$$

Where K=0.9 is the Scherrer's constant, D is the crystalline size, λ is the X-ray wavelength (1.54060 Å for Cu K_{α} radiation), β is the full width at half-maximum (FWHM) of the diffraction peak and θ is the Bragg diffraction angle. The average ZnO particle size was calculated using all the nine diffraction peaks. The average crystalline size calculated using Scherrer formula are as listed in Table 4.2.

4.1.1.1 Williamson Hall Analysis

The Scherrer formula does not cater for the micro-structures of the lattice, intrinsic strain which is found in the nanocrystals as a result of point defect, grain boundary, triple junction and stacking faults [127]. Williamson-Hall (W-H) method considers the contribution of the crystallite size (D) and the line broadening in XRD. The contribution from the crystallite size is given by Scherrer (equation 4.4), and the microstrain contribution relates to;

$$\beta_s = 4\epsilon \tan\theta \quad (4.5)$$

where K, λ and θ are as described in Scherrer's equation, β_s is the FWHM related to the line

broadening from microstrain and ε is the root mean square (RMS) value of the microstrain and is assumed to be the same in all diffraction peaks [128]. It can be assumed that the particle size and strain contributions to line broadening do not rely on each other hence Williamson's equation is given by summing equations (4.4) and (4.5) [129];

$$\beta_{hkl} = \beta + \beta_s \quad (4.6)$$

After substitution equation (4.6) becomes:

$$\beta_{hkl} = \frac{K\lambda}{D\cos\theta} + 4\varepsilon\tan\theta \quad (4.7)$$

By rearranging equation (4.7) the equation becomes:

$$\beta_{hkl}\cos\theta = \frac{K\lambda}{D} + 4\varepsilon\sin\theta \quad (4.8)$$

The equation (4.8) is referred to as the W-H equation. This equation resembles the uniform deformation model (UDM), where the strain was uniform in all crystallographic directions. The average crystalline size was obtained by plotting $4\varepsilon\sin\theta$ along the x-axis and $\beta_{hkl}\cos\theta$ along the y-axis for the materials as shown in Figure 4.3. The average crystalline size was obtained from the y-intercept of the best fit line. The strain ε was given by the gradient of the best fit line. The crystallite parameters, crystallite size and microstrain are given in Table 4.2. The crystallite size calculated from Scherrer's equation was compared with the one obtained from W-H equation. The W-H equation gave a value that is slightly higher than the Scherrer technique. This is because Scherrer method computes the coherence length of the X-rays hence any crystal disorder will give a smaller value than the actual size while W-H method involves the microstrain effect [130].

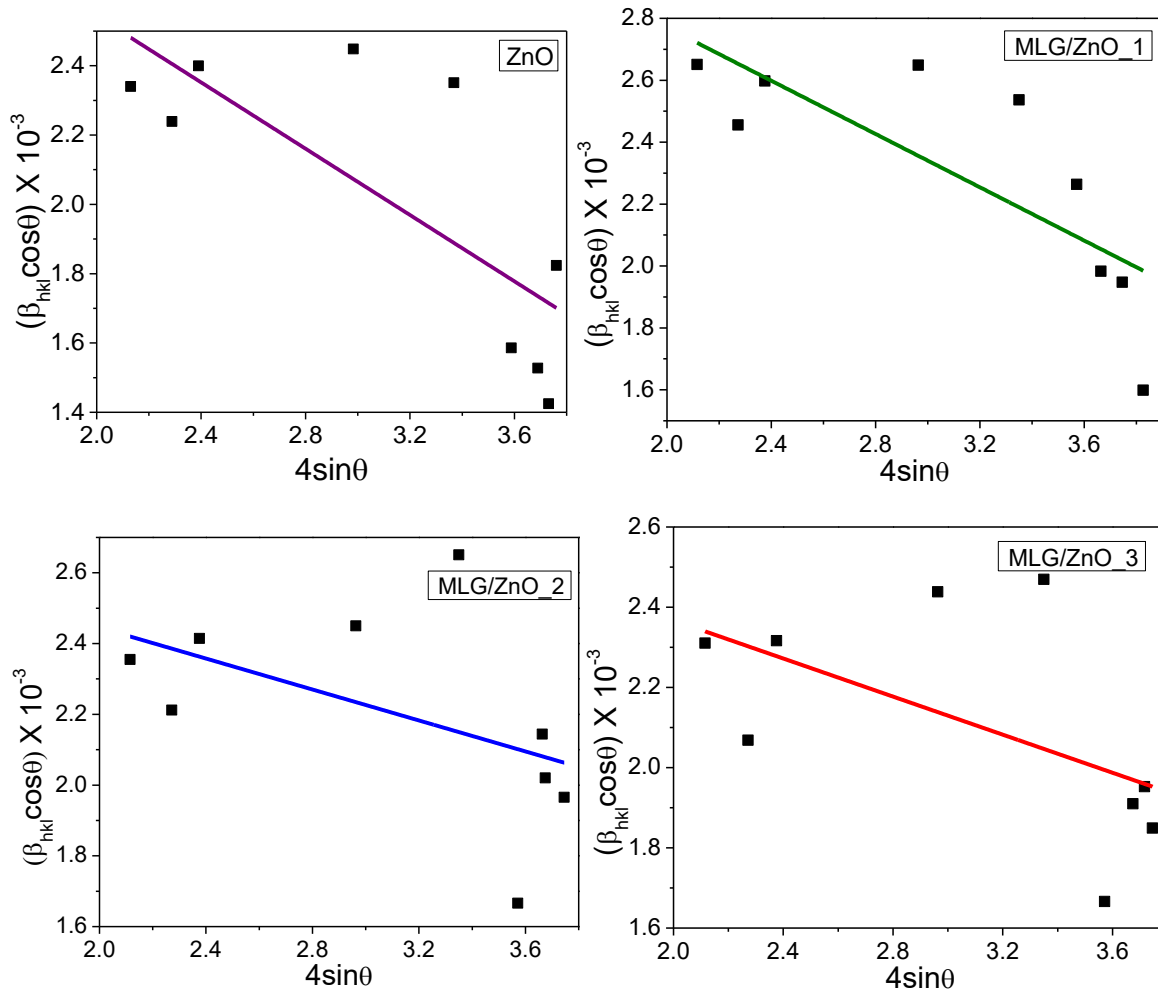


Figure 4.3: Williamson-Hall plots for pure ZnO and MLG nanocomposites.

Table 4.2: Crystallite sizes from W-H and Scherrer and lattice strain of ZnO and MLG/ZnO composites from XRD analysis.

Sample	Interplanar distance (d) (nm)	Crystallite size (nm)		Lattice strain ϵ
		W-H	Scherrer	
ZnO	0.2452	46.21	43.74	-4.69×10^{-4}
MLG/ZnO_1	0.2464	38.52	37.72	-4.30×10^{-4}
MLG/ZnO_2	0.2464	47.81	41.01	-2.19×10^{-4}
MLG/ZnO_3	0.2464	48.82	42.21	-2.37×10^{-4}

Addition of the MLG to the ZnO (ratio 1:1) slightly increased the lattice parameters, reduced the crystallite sizes and increased the lattice strain. However, the increase in MLG content in the composites did not alter the values of the three parameters, which may be attributed to saturation effects and the nature of the *ex-situ* casting method used. The crystallite sizes computed using the Scherrer equation increased with an increase in ZnO content in the composites.

4.1.1.2 Halder-Wagner Analysis

Halder and Wagner suggested an alternative equation for the calculation of D and ε , with the integral breadth, β^* and lattice-plane spacing d^* , of the reciprocal lattice point and reciprocal cell, respectively [131].

$$\left(\frac{\beta^*}{d^*}\right)^2 = \frac{K}{D} \cdot \frac{\beta^*}{(d^*)^2} + (2\varepsilon)^2 \quad (4.9)$$

and

$$\beta^* = \frac{\beta \cos \theta}{\lambda} \quad (4.10)$$

$$d^* = \frac{2 \sin \theta}{\lambda} \quad (4.11)$$

based on the theory that Gaussian and Lorentzian components of β^* are exclusively due to size and strain effects, respectively.

After substitution, equation (4.9) becomes;

$$\left(\frac{\beta}{\tan \theta}\right)^2 = \frac{K\lambda}{D} \cdot \frac{\beta}{\tan \theta \sin \theta} + 16\varepsilon^2 \quad (4.12)$$

Equation (4.12) is the Halder-Wagner (H-W) equation, where K, β , λ , D and ε have

same meaning as in Scherrer and W-H equations. Equation (4.12) is considered as a straight line, $y = ax + b$, where $y = (\beta/\tan \theta)^2$ plotted as a function of $x = \beta/(\tan\theta\sin\theta)$. Subsequently, the crystallite size and lattice strain are described by the slope ($K\lambda/D$) and intercept ($16\epsilon^2$), respectively. The H-W method has a great merit over W-H method because the data for small and intermediate angles is assigned more weight than those at higher diffraction angles [132]. H-W plots for ZnO and MLG/ZnO nanocomposites are illustrated in Figure 4.4. It is worth noting that all data points are less scattered about the least-square fit in H-W plots suggesting that lower angles of reflections corresponding to higher $(\beta/\tan\theta\sin\theta)$ values were indeed assigned more weight in the least-square fit. The crystallite sizes and lattice strain values determined from H-W plots are shown in Table 4.3.

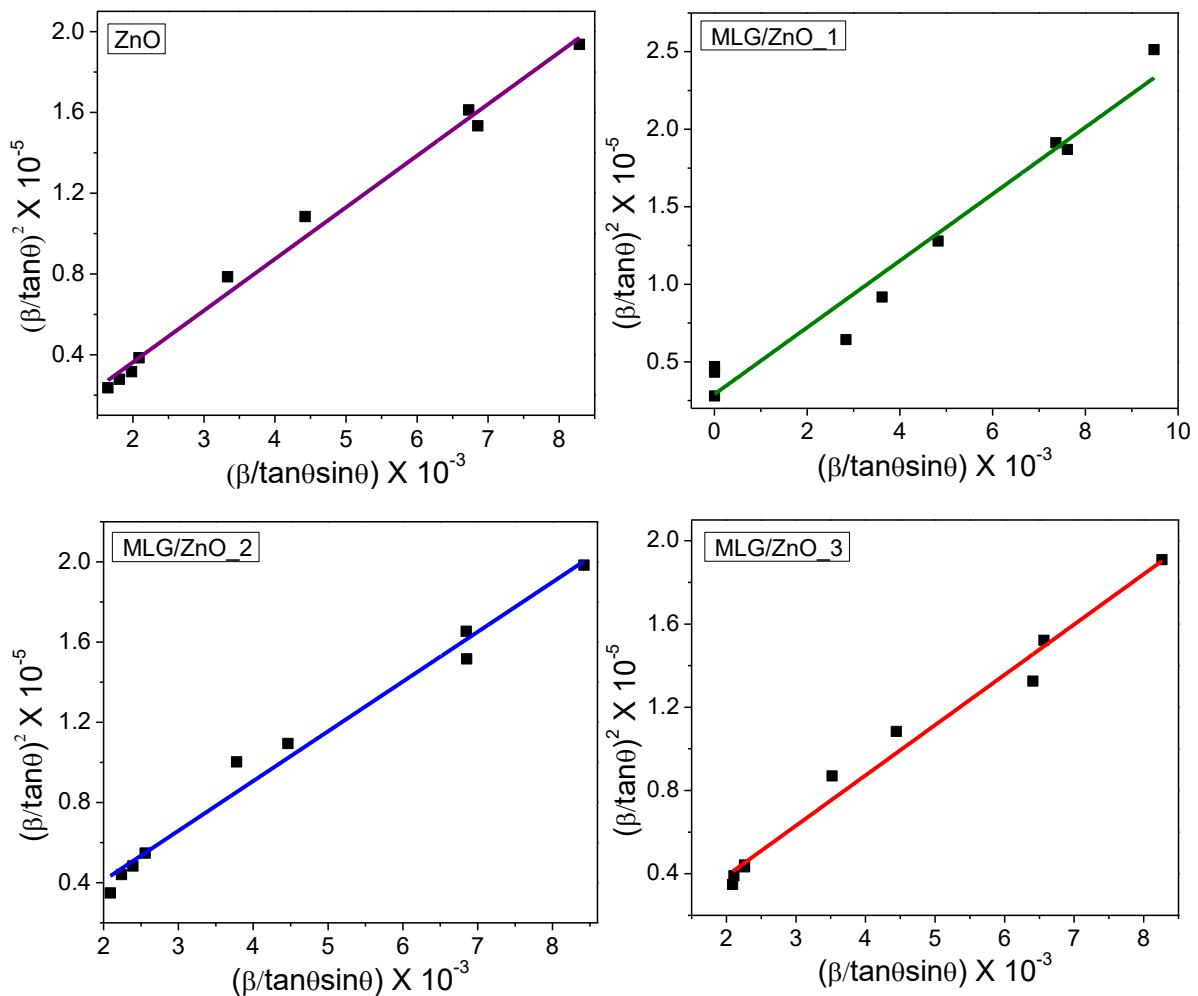


Figure 4.4: Halder-Wagner plots for pristine ZnO and MLG/ZnO nanocomposites.

Table 4.3: Crystallite size and lattice strain determined from H-W method.

Sample	H-W Crystallite size (nm)	$\epsilon \times 10^{-4}$
ZnO	54.16	-3.05
MLG/ZnO_1	49.34	-3.22
MLG/ZnO_2	55.46	-2.30
MLG/ZnO_3	57.30	-2.43

It was found that as the MLG content decreased in the composite the crystallite size increased, and the lattice strain also increased. In both W-H and H-W plots the scattering of data points increased as the lattice strain values increased, however H-W method displayed more consistent results than W-H method.

4.1.1.3 Wagner-Agua Analysis

Wagner and Agua also proposed an alternative technique for determination of crystallite size and lattice strain using the relation [133];

$$(\beta \cos \theta)^2 = (4\epsilon \sin \theta)^2 + \left(\frac{K\lambda}{D}\right)^2 \quad (4.13)$$

In the Wagner-Agua (W-A) plot, $y = (\beta \cos \theta)^2$ is plotted against $x = (4\sin \theta)^2$ as shown in Figure 4.5. Then, the slope and y intercept of the linear fits afford ϵ and $(K\lambda/D)^2$, respectively. The crystallite size and lattice strain have been evaluated and shown in Table 4.4.

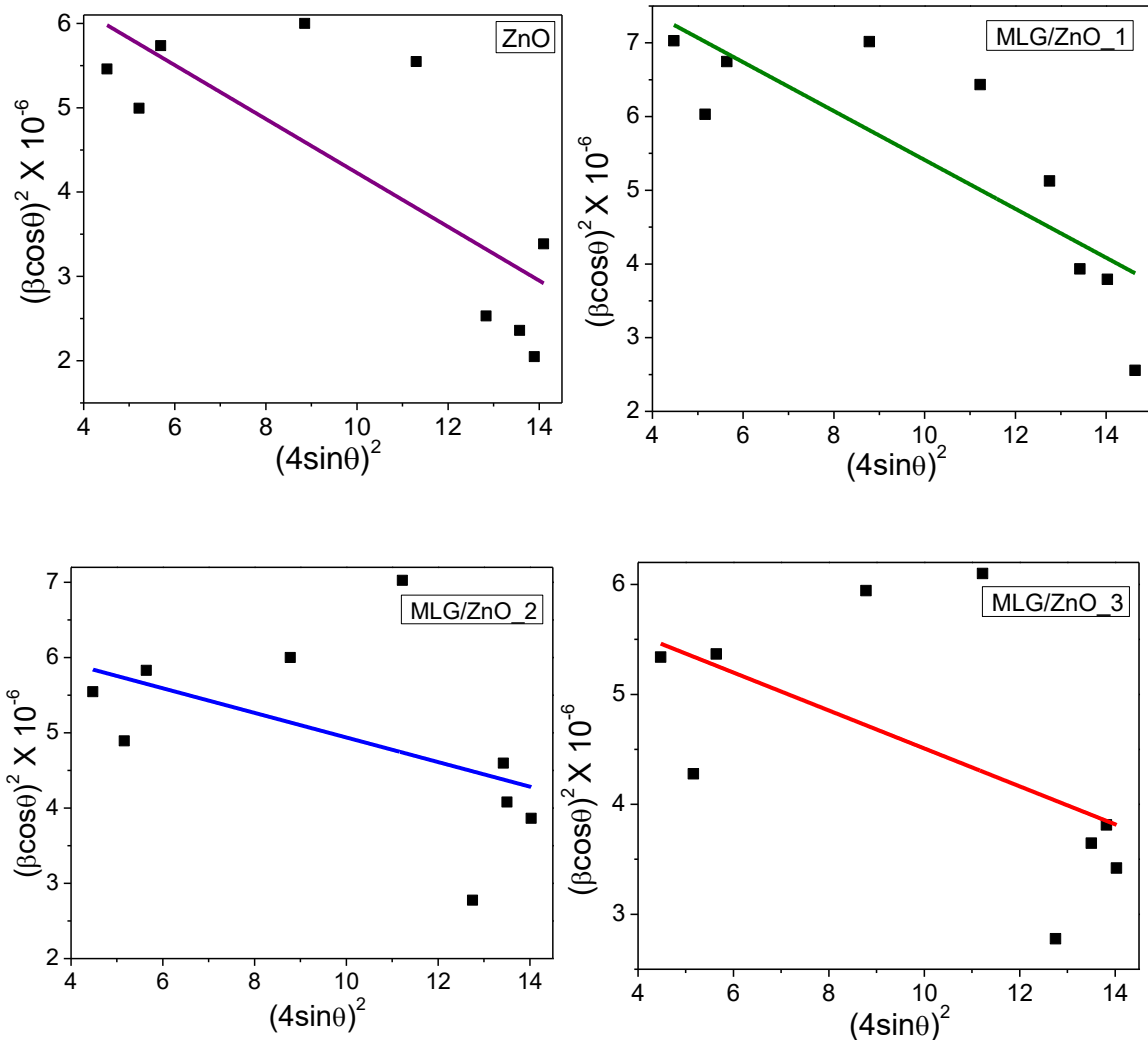


Figure 4.5: Wagner-Agua plots for pure ZnO and MLG/ZnO composites.

Table 4.4: Crystallite size and lattice strain determined from W-A plots.

Sample	W-A Crystallite size (nm)	$\epsilon \times 10^{-7}$
ZnO	50.90	-3.19
MLG/ZnO_1	46.94	-3.32
MLG/ZnO_2	54.08	-1.63
MLG/ZnO_3	55.53	-1.73

In the W-A method, the crystallite size increases with a decrease in the MLG content in the composites just like with Scherrer, W-H and H-W methods. The scattering of the data

points in W-A plots is like those in W-H plots. The lattice strains deduced using W-H, H-W and W-A methods were found to be negative this is because the ZnO contained in the composite was calcinated at high temperature (700 °C). The negative sign is also due to the compressive forces experienced by the crystal lattice.

4.1.2 Raman spectroscopy analysis

Raman spectroscopy was used to study the structural transformations of the as-synthesized nanomaterials. Raman spectroscopy is one of the best nondestructive techniques to study the structure and quality of carbon materials [134] and to confirm defects, ordered and disordered structures, and the number of layers in graphene. A Raman spectra of graphene exhibit two prominent bands, D-band and G-band [135]. The D-band reflects the disorder band or the defect band which symbolizes a ring breathing mode from sp^2 carbon rings of k-point phonons of A_{1g} symmetry and it was previously reported in literature [12,29,100]. The G-band is a vibrational mode that involves the sp^2 hybridized carbon atoms containing multilayer graphene sheet and is associated with first order scattering of E_{2g} phonon [98]. The D-bands for CH-C, CH-AC and MLG were observed at 1349, 1344 and 1343 cm^{-1} , respectively, in agreement with previous reports [136,137]. The G-band wavenumber decreased from 1591 cm^{-1} for CH-C, 1590 cm^{-1} for CH-AC to 1589 cm^{-1} for multilayer graphene, indicating a shift of the material in showing more graphitic features [12,103,138].

The graphene spectrum can also be described using the 2D band which is the second order of the D band. The 2D band at 2700 cm^{-1} and S3 (D+G) at 2929 cm^{-1} for graphene confirmed the degree of graphitization of the materials [139]. It is important when dealing with graphene-based catalysts to determine the number of graphene layers since they contribute to the surface area of the catalyst thus affecting the catalytic efficiency. The 2D band for graphene observed at 2700 cm^{-1} indicates multilayer structure of the synthesized graphene materials [100,136]. The crystallinity of the material corresponds to the intensity ratio of D and G peaks [140]. The ratio of

the integrated intensities I_D/I_G value increased from 0.96, 1.03 and 1.09 for CH-C, CH-AC and MLG, respectively showing an increase in crystalline nature of MLG an observation confirmed by other researchers [99,102,140]. It can be concluded that each treatment step affected the crystallinity of the material. The Raman spectra for CH-C, CH-AC and MLG are illustrated in Figure 4.6.

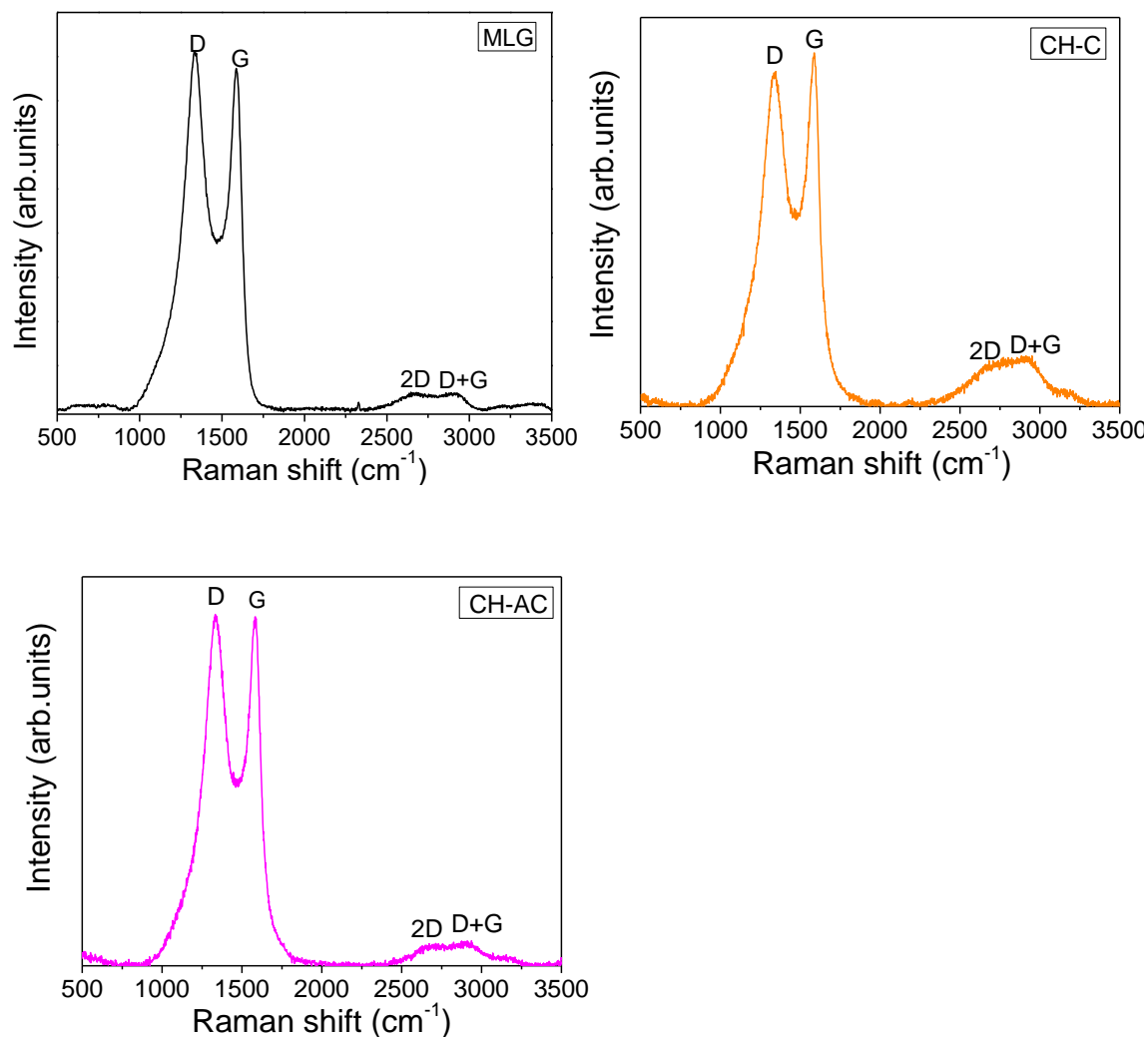


Figure 4.6: Raman spectra of MLG, CH-C and CH-AC.

The chemical reaction of graphene-based catalysts is influenced by the in-plane crystallite sizes (L_a) of graphene sheet. The L_a is the average distance of the inter-defects and can be used to study defects caused by heteroatoms doping. The L_a value from Raman spectroscopy can be determined using Tuinstra-Koeing (TK) relation [100]:

$$L_a(nm) = \frac{2.4 \times 10^{-10} \lambda^4}{I_D/I_G} \quad (4.14)$$

where λ is the Raman excitation wavelength, I_D/I_G is the intensity ratio of the D and G band in Raman spectra. The in-plane crystallite size L_a of multilayer graphene sheet was calculated to be 17.6 nm. Raman spectra can also be used to study the phonon modes. The Transverse (TO) and Longitudinal (LO) which are the optical modes splits into the axial and planar type modes. The atomic displacement takes place either along the c-axis or perpendicular to the c-axis [103]. The wurtzite structure of ZnO with four atoms per unit cell is assigned 12 phonon branches, 9 optical and 3 acoustic containing two E2 vibrations, one transverse A1, one transverse E1, one longitudinal A1 and one longitudinal E1, as discovered by Damen et al [141]. Figure 4.7 shows the Raman spectrum for pure ZnO showing characteristic Raman modes of E_2^{high} at 438 cm^{-1} which shows the formation of the pair Zn-O for the presence of wurtzite ZnO [142-145]. The vibrational mode at 203 cm^{-1} is assigned to the overtone of the E_2^{low} mode. ZnO vibrational signals below the wave number 300 cm^{-1} belong to the Zn sublattice and the ones between $300-700 \text{ cm}^{-1}$ are due to the oxygen atoms. The ZnO Raman modes at 378 and 582 cm^{-1} are assigned A1 (TO), and A1 (LO) respectively [24,75,146,147]. The Raman peaks for ZnO and MLG that were observed in the pure samples were displayed in the MLG/ZnO nanocomposites which agrees with XRD results. The Raman spectra for MLG/ZnO nanocomposites are displayed in Figure 4.7.

The presence of ZnO is more expressed in the MLG/ZnO_3 nanocomposite since it shows more intense ZnO Raman peaks. However, there was a slight shift in the observed wavenumbers for the nanocomposites. The ZnO Raman modes were observed in all the MLG/ZnO nanocomposites. The Raman mode at 438 cm^{-1} is assigned optical E_2^{high} . The wide band between 520 and 600 cm^{-1} are E1 (LO) and A1 (LO) vibrational modes [143] as already indicated with pure ZnO and these modes are also ascribed to defects due to oxygen vacancies. The peaks at 330 and 1127 cm^{-1}

symbolized the 2E1 (LO) which are due to the second order or multiple phonon scattering of the ZnO Raman modes. The three predominant features of Raman spectrum for multilayer graphene were observed in MLG/ZnO nanocomposites. The D-band, G-band, 2D and S3 (D+G) bands located at 1335, 1586, 2709 and 2915 cm^{-1} , respectively, were observed in all the MLG/ZnO nanocomposites. The ratio of I_{2D}/I_G was less than 1 for all the MLG/ZnO nanocomposites which indicates multilayer structure for graphene [148]. The value of I_D/I_G for MLG/ZnO_1 was calculated to be 1.04 which was the highest compared to other MLG/ZnO composites indicating high graphitization degree of the material [12,149,150], which is in agreement with the XRD results. The I_D/I_G were 1.02 and 1.00 for MLG/ZnO_2 and MLG/ZnO_3 respectively.

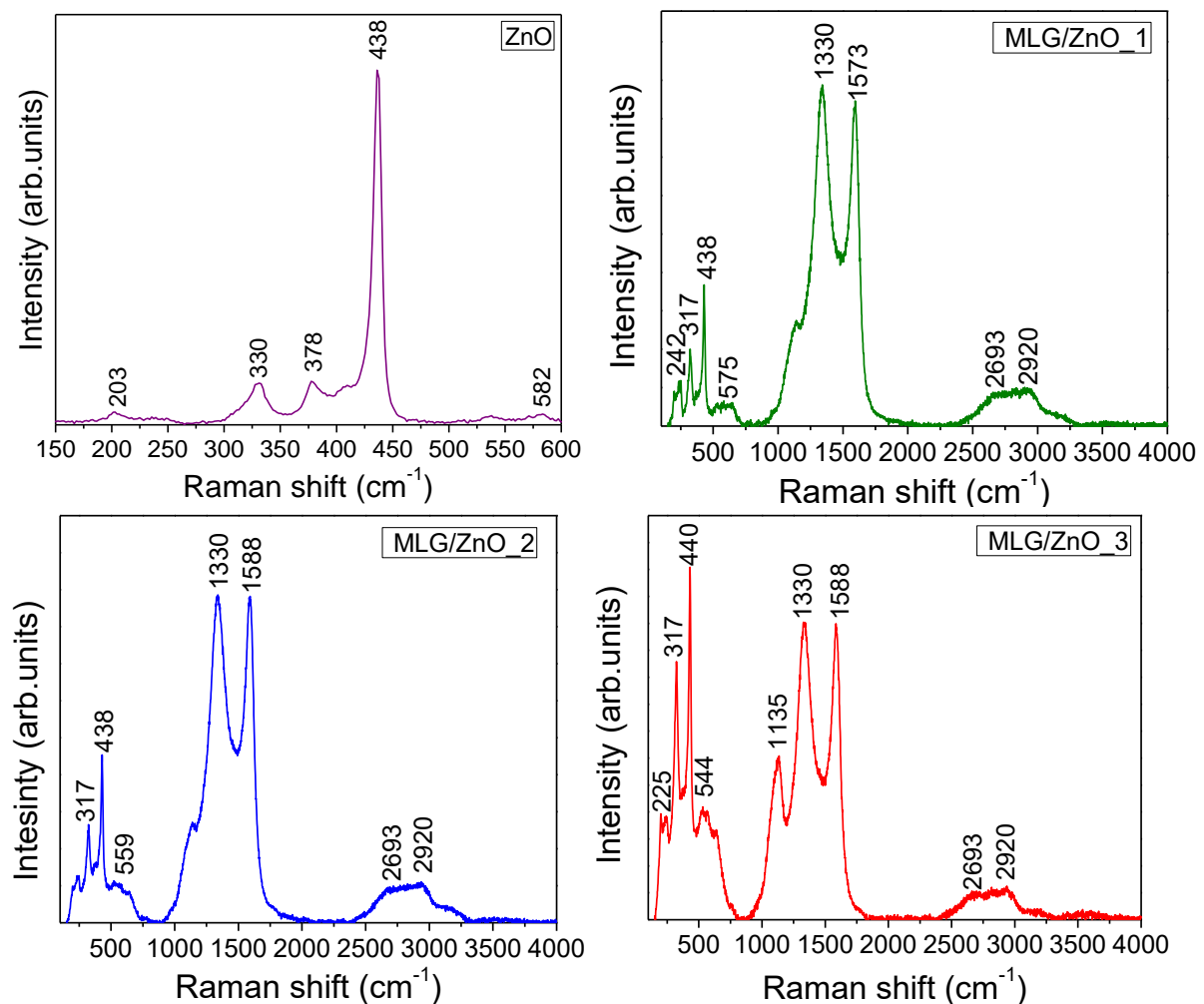
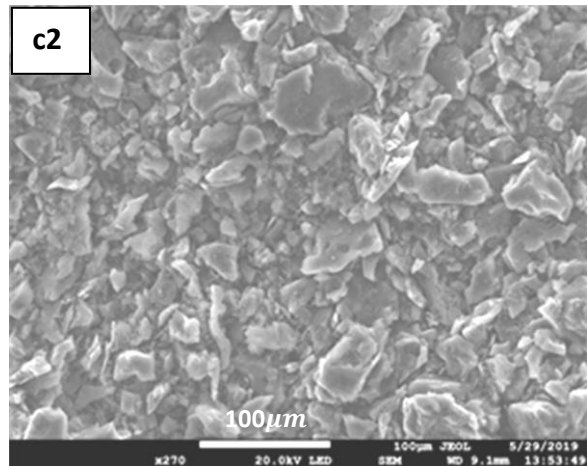
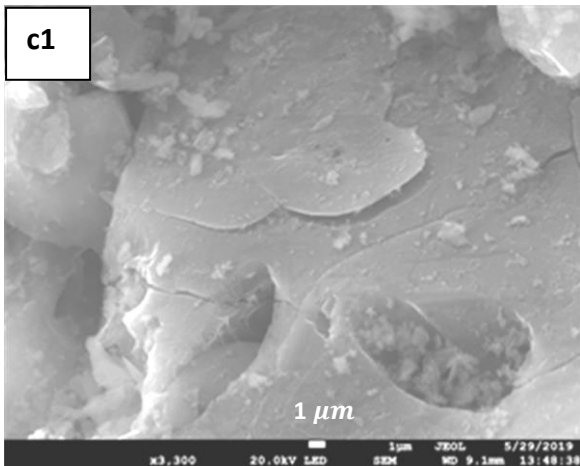
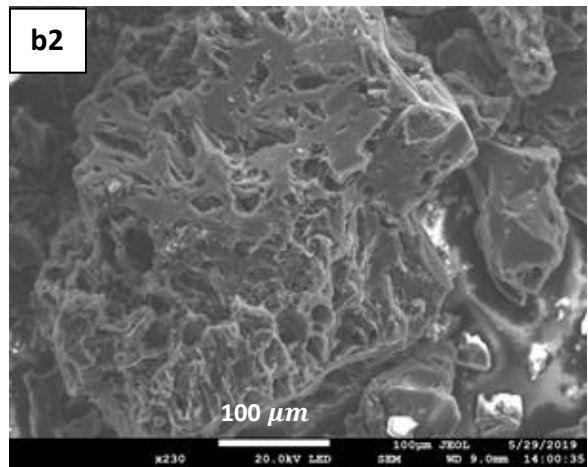
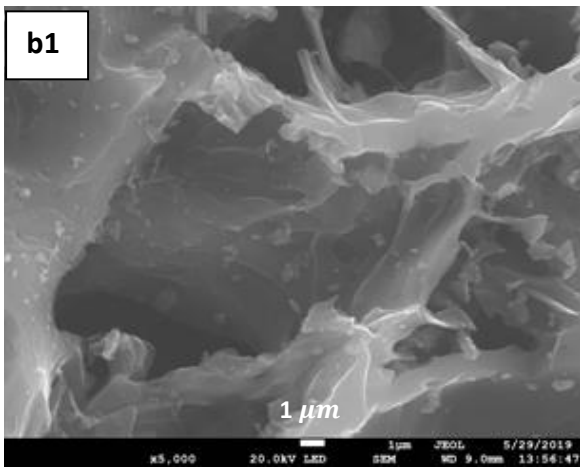
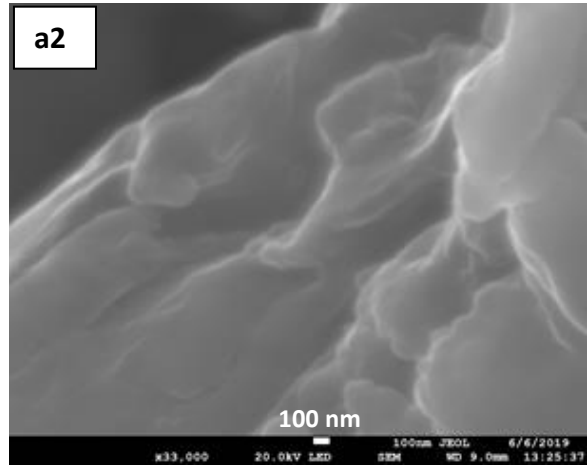
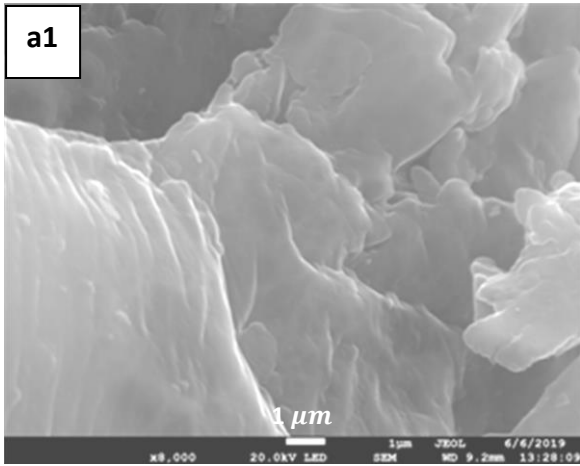


Figure 4.7: Raman spectra of pure ZnO and MLG/ZnO nanocomposites.

4.1.3 SEM AND HRTEM analysis

The surface morphology of the as-synthesized materials were examined by scanning electron microscope (SEM) and High resolution-TEM (HRTEM). The SEM micrographs of the samples are shown in Figure 4.8. The morphology of MLG synthesized from corn husk was best illustrated by following its transformation from the raw material. The raw corn husk structure in Figure 4.8a1 shows evidence of naturally abundant lignocellulosic microfibril networks. This gives it a rough surface morphology. The CH-C material in Figure 4.8b1 display evidence of open pores caused by loosening of the cellulose microfibrils. The carbonized materials activated with KOH in Figure 4.8c1 transformed to a sheet-like structure. The KOH creates micro and mesoporosity by burning some of the carbon in the cellulose network reducing thickness of carbon layers hence stacked sheet-like structures were transformed into a multilayer sheet-like structure, graphene. The ripples and crinkles on the edge of these sheets observed in Figure 4.8d1 symbolize multilayer graphene sheets [98]. The SEM of pure ZnO in Figure 4.8e2 revealed short hexagonal nanorods of the synthesized ZnO. ZnO NPs were well dispersed on the surface and edges of the multilayer graphene as displayed in Figure 4.8f1, 2. The particle size distribution of the ZnO is illustrated using frequency distribution histogram shown in Figure 4.9a. The average particle size of the ZnO nanostructures was 194 nm. The chemical composition of MLG/ZnO composite was determined by energy dispersive spectroscopy (EDS). The EDS spectrum confirmed the presence of C, O and Zn in the composite hence verified the successful incorporation of multilayer graphene and ZnO. The peaks at 2 keV were identified as gold since it was used for coating the surfaces of the samples. The spectrum of the sample is shown in Figure 4.9b. The inset in Figure 4.9b shows a report of the percentage weight composition of elements in the MLG/ZnO composite.



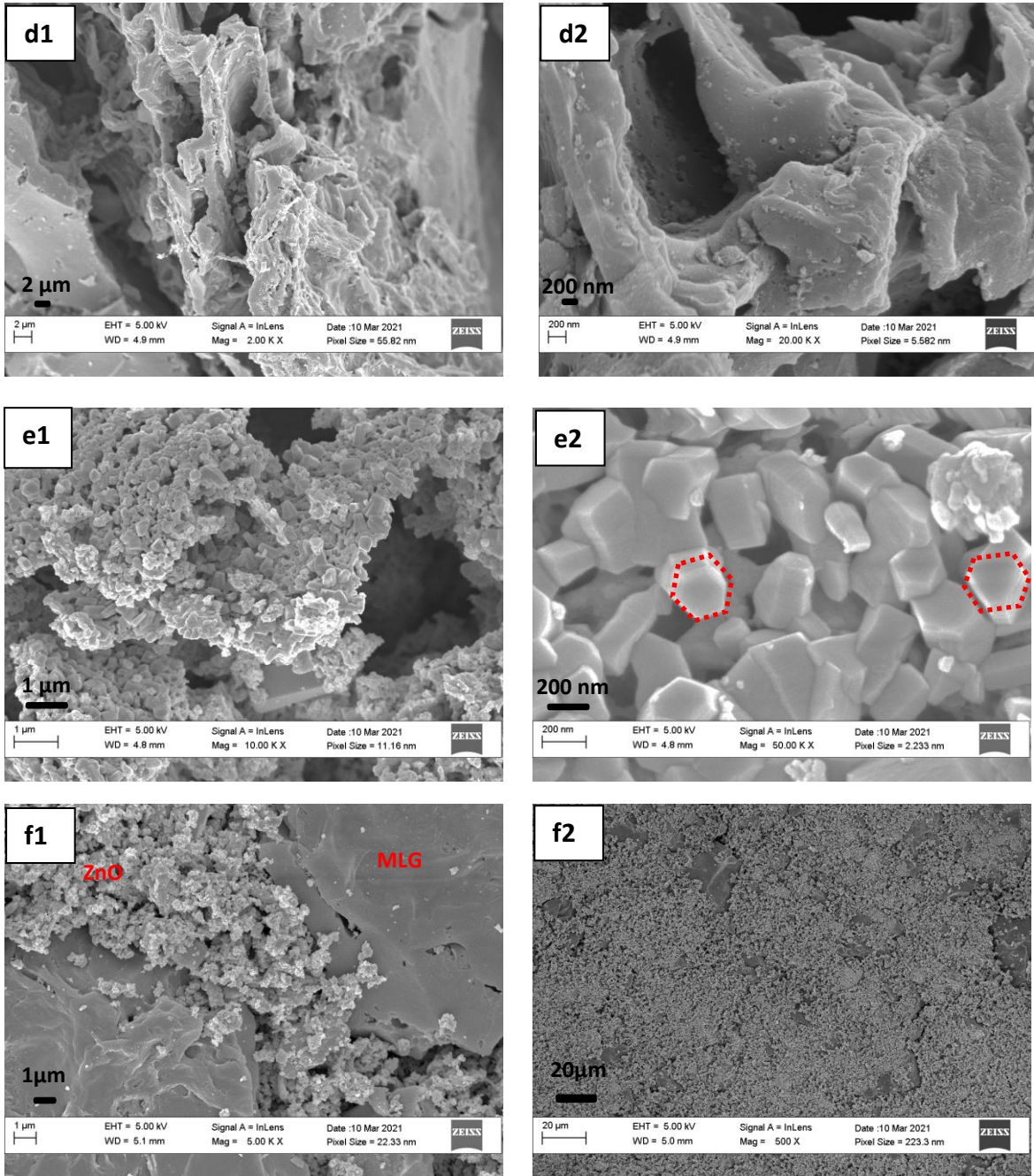


Figure 4.8: SEM micrographs of MLG and its treatment stages (a-d) and pristine ZnO (e), f) MLG/ZnO₃ nanocomposite taken at low and high magnifications.

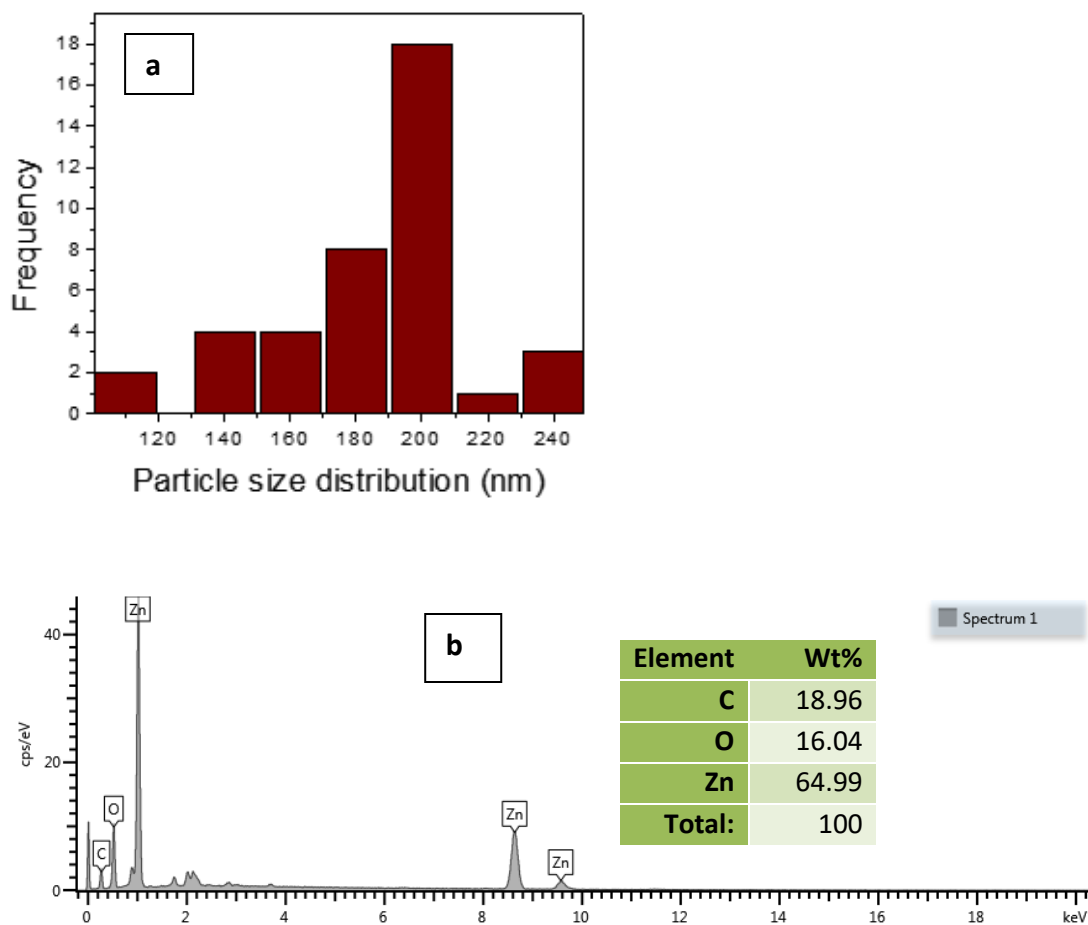
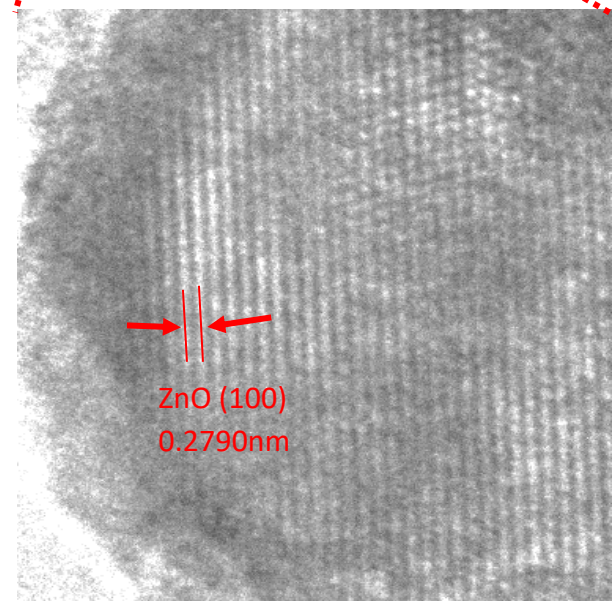
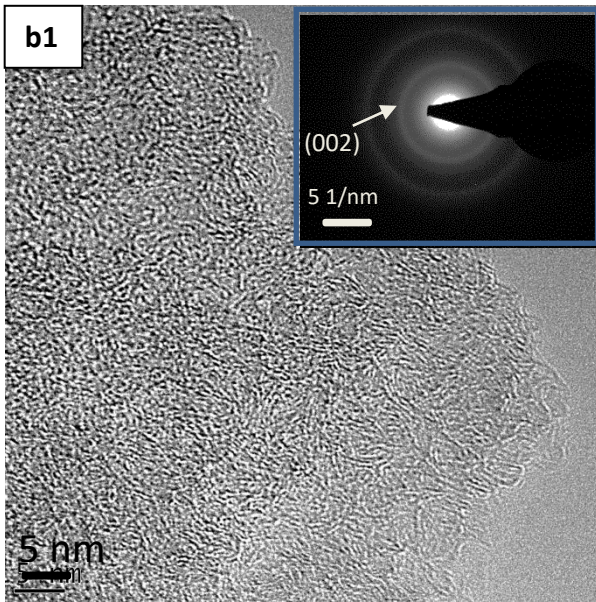
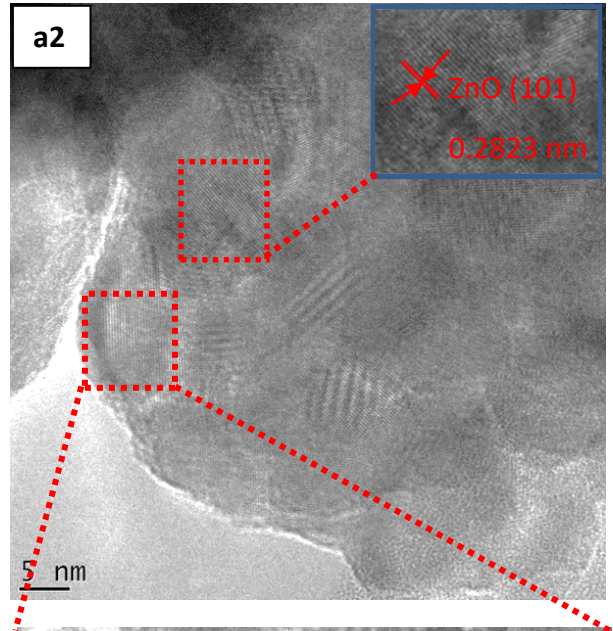
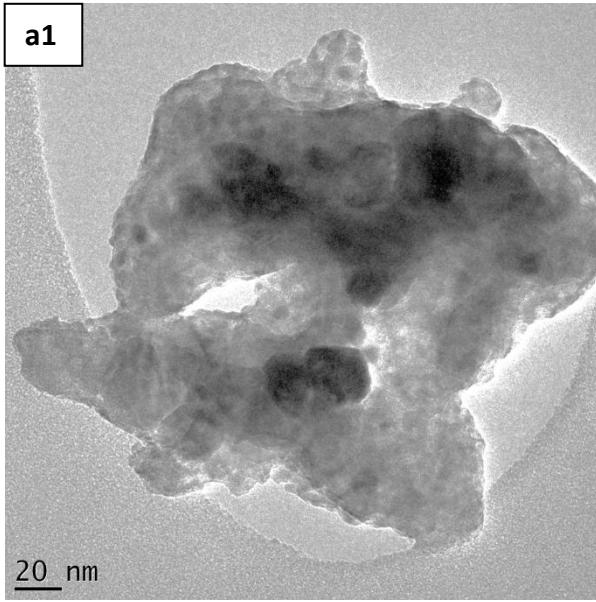


Figure 4.9: a) particle size histogram of ZnO NPs b) EDS spectrum of MLG/ZnO₃ nanocomposite.

Figure 4.10a2 display lattice fringes spacing of 0.2823 and 0.2790 nm corresponding to (100) planes of ZnO hexagonal wurtzite structure. Figure 4.10b1 display a wrinkled/wormy fringe of MLG. The SAED pattern (as inset) in Figure 4.10b1 revealed that most of the MLG particles were amorphous. HRTEM depict hexagonal shape of ZnO particles (as inset in Figure 4.10c1) which supports SEM results. Figure 4.10c1,2 show well dispersed agglomerated ZnO particles on the MLG surfaces. Lattice fringes observed from MLG/ZnO composite in Figure 4.10c2 displayed d-spacing of 0.2818 nm corresponding to (100) ZnO diffraction peak. The diffraction rings observed from SAED pattern of the synthesized ZnO Figure 4.9d are in good agreement with XRD results since they reveal polycrystalline structure of ZnO with rings assigned (100), (101), (102), (110), (103) and (200).



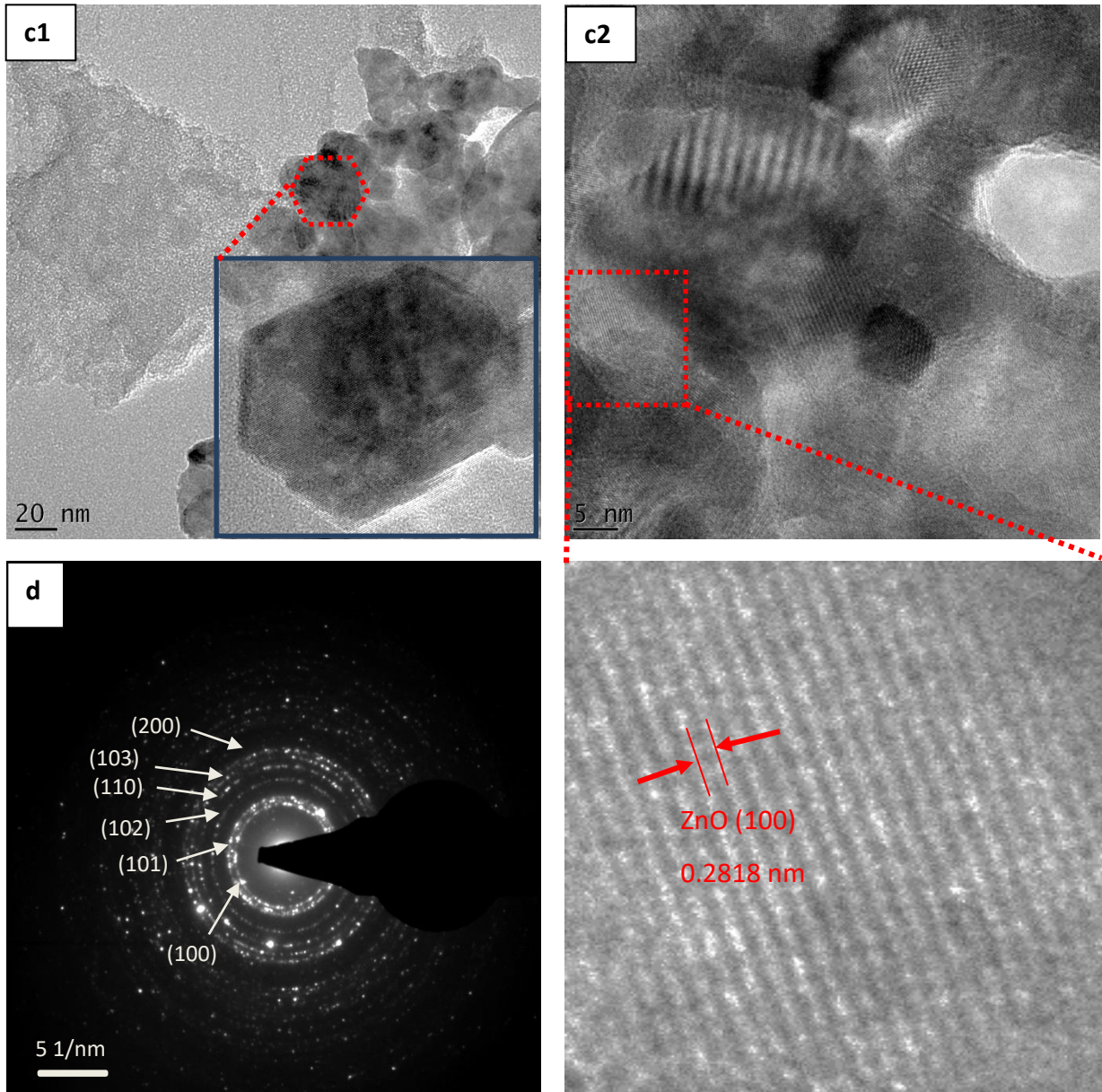


Figure 4.10: HRTEM images of a) ZnO, b) MLG. Inset is SAED patterns of MLG and c) MLG/ZnO_3 composite with calculated d-spacing using lattice fringes d) SAED patterns of MLG/ZnO_3.

4.1.4 BET analysis

The nitrogen adsorption-desorption isotherms of MLG and MLG/ZnO_3 displayed as insets in Figure 4.10a and c show a typical type I curve with a relative pressure (P/P_0) not exceeding 1, hence revealing the microporous nature of the materials. The t-plot method was used to calculate the specific surface area of the microporous materials. The thickness (t) values were calculated using Harkins and Jura model [151];

$$t \text{ (nm)} = 0.1 \left[\frac{13.99}{0.034 - \log(P/P_0)} \right]^{1/2} \quad (4.15)$$

The points at relative pressure between $0.05 < P/P_0 < 0.35$ were selected for determination of the surface area. The micropore volume was given by the vertical intercept and the external surface area was calculated from the slope using equation (4.17).

$$V_{\text{micro}} = I * 0.001547 \text{ (cm}^3\text{)} \quad (4.16)$$

$$S_t \text{ (m}^2\text{/g)} = 15.47 * s \quad (4.17)$$

$$S_t = S_{\text{ext}} \quad (4.18)$$

$$S_{\text{micro}} = S_{\text{BET}} - S_{\text{ext}} \quad (4.19)$$

where P and P_0 are equilibrium and saturation pressures of adsorbate, I is the intercept, s is the slope of the straight line fitted to the t-plot, S_{micro} is micropore surface area and 15.47 is the constant for the conversion of the gas to the liquid volume, S_t represents the total surface area of the sample, S_{BET} is the BET surface area.

The isotherm for ZnO was classified as non-porous according to IUPAC. Figure 4.11b shows a typical type II curve hence the surface area of ZnO was calculated using the BET equation [152,153];

$$\frac{1}{Q\left[\left(\frac{P_0}{P}\right) - 1\right]} = \frac{c-1}{Q_m c} \left(\frac{P}{P_0}\right) + \frac{1}{Q_m c} \quad (4.20)$$

$$S_t = \frac{Q_m N S}{V} \quad (4.21)$$

$$S_{BET} = \frac{S_t}{a} (m^2/g) \quad (4.22)$$

where Q is quantity of gas adsorbed, Q_m is adsorbed gas quantity, and c is the BET constant. P, P_0 , S_t , and S_{BET} are as described in the t-plot method. N is Avogadro's number = 6.02×10^{23} molecules/mol, S is cross-sectional area of adsorbed gas molecule and a is the mass of sample. Using t-plot method, the surface area was determined by plotting volume adsorbed as a function of the thickness (t) of the adsorbed film as illustrated in Figure 4.11a and c.

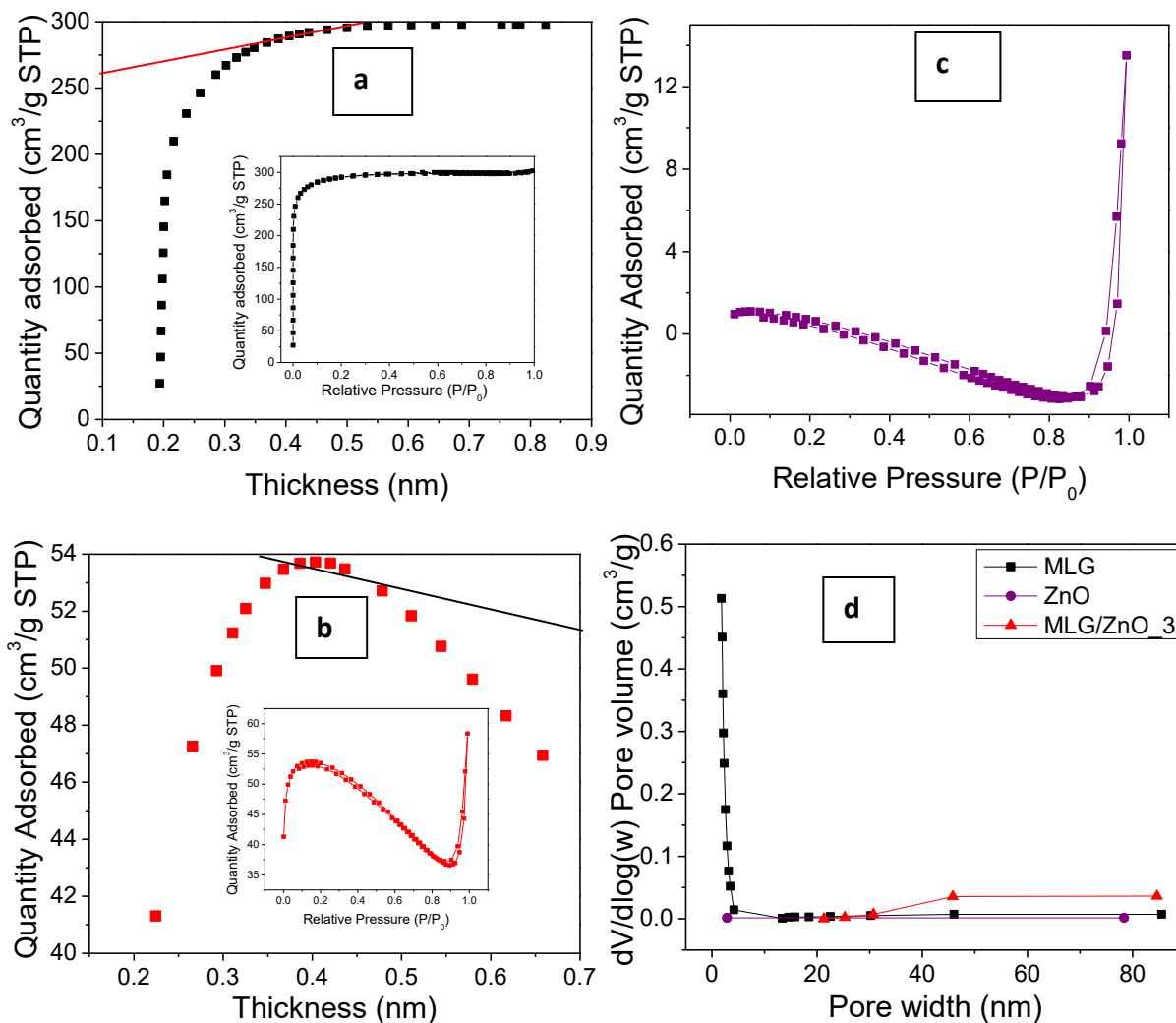


Figure 4.11: t-plots for a) MLG and b) MLG/ZnO₃ (inset shows N₂ adsorption-desorption isotherm plots at 77 K for the two materials which were used to acquire the t-plot) c) N₂ adsorption-desorption isotherm plot at 77 K for ZnO and d) Pore size distribution curves for the three materials as labelled.

The BET surface area of MLG, ZnO and MLG/ZnO₃ were computed to be 1144.52, 0.42 and 148.74 m²/g, respectively as illustrated in Table 4.5. The pore size distribution plot in Figure 4.11d was calculated using the adsorption branch of the isotherm by Barret-Joyner-Halenda (BJH) model. The adsorption average pore diameter for MLG, ZnO and MLG/ZnO₃ were computed to be 0.15, 14.32 and 1.71 nm, respectively revealing the microporous nature of MLG and MLG/ZnO₃ with pore diameters less than 2 nm. The BJH

adsorption cumulative volume of pores between 1.7 and 300 nm was 0.071285, 0.022653 and 0.036881 cm³/g for MLG, ZnO and MLG/ZnO_3, respectively. The results showed less surface area for bare ZnO and increased surface area in the composite (MLG/ZnO_3) as expected. Therefore, the presence of MLG in the composite increased the surface area of the material.

Table 4.5: BET Surface area and pore diameters of MLG, ZnO and MLG/ZnO nanocomposite.

Sample	BET Surface area (m ² /g)	Pore diameter (nm)
MLG	1144.52	0.15
ZnO	0.42	14.32
MLG/ZnO_3	148.74	1.71

The high surface area of MLG contributes to easy adsorption of pollutants to the surface, therefore facilitating better interaction between the catalyst and the pollutant resulting in improved photocatalytic activity.

4.2 Optical Characterization Results

4.2.1 Absorbance and optical band gap energy

The UV-Vis analysis is the principal tool to investigate the changes in the prepared semiconductor materials. The energy band gap influences the optical properties of semiconductors hence can be determined by measuring the absorbance of the as-synthesized materials. It is crucial to study the band gap of the semiconductors to determine their potential applications especially in photocatalysis.

4.2.1.1 Absorbance measurements

The UV-Vis absorbance spectra of pure ZnO and MLG/ZnO nanocomposites are as exhibited by Figure 4.12. The measurements were obtained by dispersing the fine powders in distilled water and ultrasonicating for several hours. A cuvette containing the dispersed NPs was loaded in a UV-Vis spectrophotometer to measure the absorbance of the as-synthesized materials. The ZnO absorption peak observed at 367 nm is in agreement with previous researchers [58,154] and symbolizes the wurtzite hexagonal structure of pure ZnO. A blue shift is observed in the MLG/ZnO nanocomposites absorption peaks, this is due to the close conjugation of the ZnO NPs and the multilayer graphene sheets that lead to high electron transfer which improved transition energy [155].

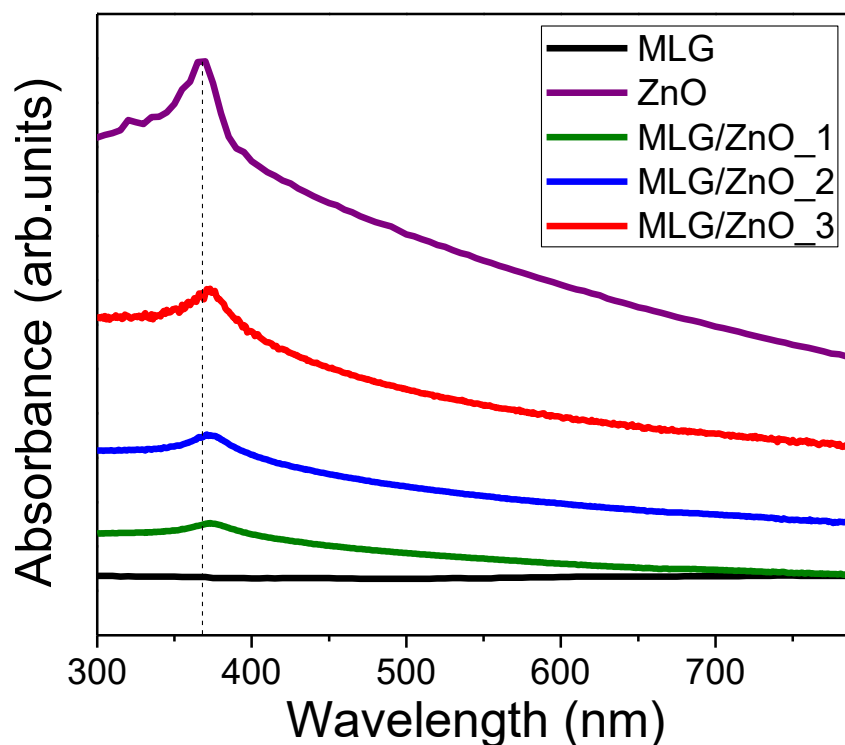


Figure 4.12: UV-Vis absorption spectra of MLG, ZnO and MLG/ZnO nanocomposites.

4.2.1.2 Determination of the optical band gap

The optical band gap of the samples was calculated using Tauc formula [156,157] that gives the relationship between absorption coefficient and the incident photon energy of the ZnO NPs:

$$\alpha h\nu = A (h\nu - E_g)^n \quad (4.23)$$

where α is the absorption coefficient, h is Planck's constant (6.625×10^{-34} J s), ν is the frequency obtained using the formula $\nu = \frac{c}{\lambda}$ where c is the velocity of light (3×10^8 m/s) and λ is the wavelength obtained from the spectra, and n is $1/2$ for direct semiconductor ZnO. The value of the direct band gap was calculated by extrapolating the linear part of the graph to $(\alpha h\nu)^2 = 0$ as shown in Figure 4.13. The energy band gap (E_g) of pure ZnO was found to be 3.09 eV. The band gap values of the MLG and MLG/ZnO composites red shifted from the pure ZnO to 2.08, 2.66, 2.75 and 2.80 eV for MLG, MLG/ZnO_1, MLG/ZnO_2 and MLG/ZnO_3, respectively. The results indicate that more of MLG content to ZnO lowers the band gap of the semiconductor hence improves visible light absorption [158]. Durmus et al [93], suggested that a decrease in the band gap of the composites might be due to the change in crystallite sizes of ZnO in MLG/ZnO nanocomposites.

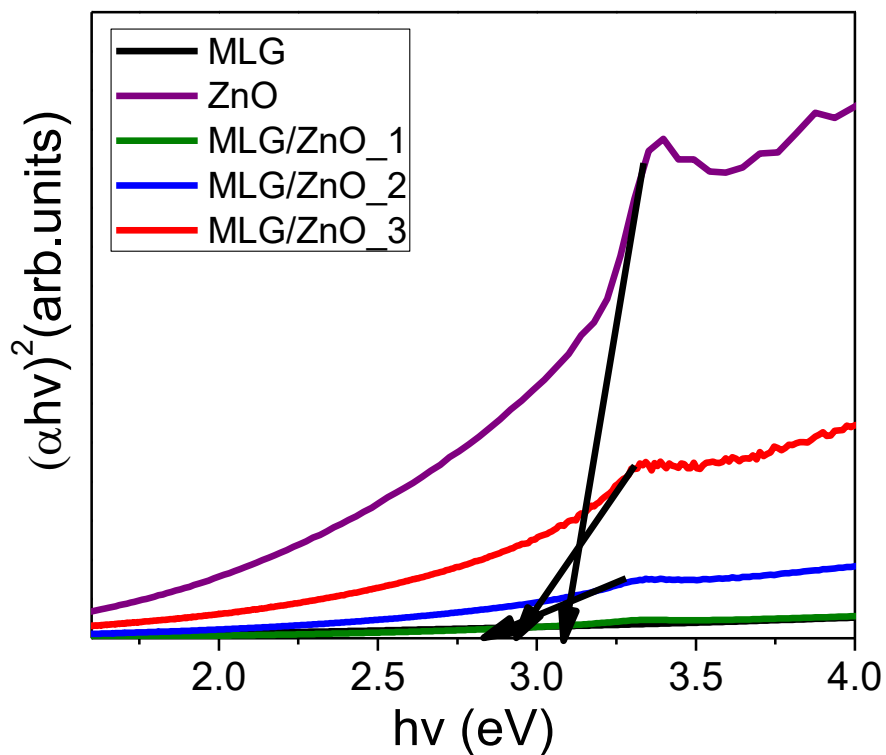


Figure 4.13: Evaluation of plotted $(\alpha hv)^2$ against photon energy ($h\nu$) for determining the optical energy band gap of MLG, ZnO and MLG/ZnO nanocomposites.

4.3 Photocatalytic Assessment

4.3.1 Photocatalytic degradation of organic dyes

The photocatalytic performance of the prepared samples was investigated by monitoring the photocatalytic degradation of BB for 3 h under sunlight irradiation. The photocatalytic activity of all the nanocomposites was conducted under the same conditions for comparison. The sampled dye solutions changed from purple to colorless/clear solution depending on the photocatalyst used as shown in Figure 4.14. The discoloration implies the degradation of the molecular structure of BB.

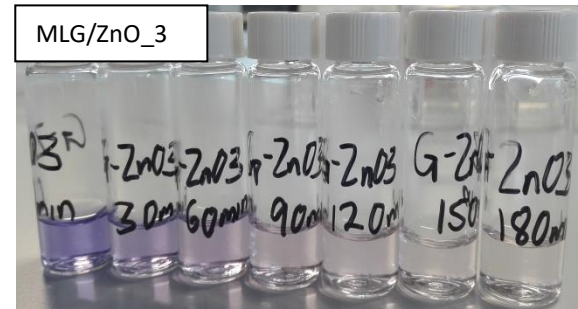
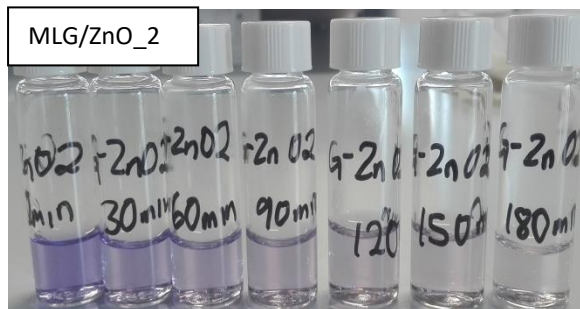
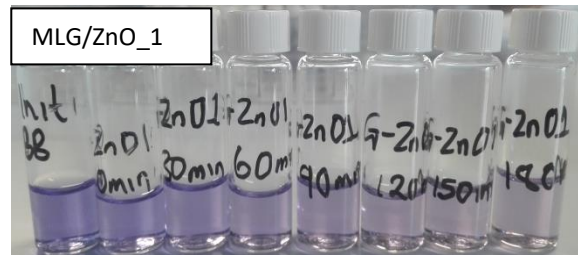
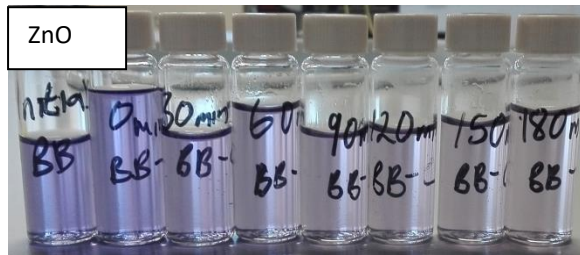


Figure 4.14: Evidence of dye colour change due to the photocatalysts as indicated in the pictures.

BB had a maximum characteristic absorption peak λ_{\max} at wavelength of 570 nm, which was monitored throughout the experiment to note its degradation. As already mentioned in detail in the methodology section 3.3.1, photocatalytic experiments were conducted on pristine ZnO and MLG/ZnO nanocomposites. Three different ratios of MLG to ZnO were prepared by varying the content of MLG to investigate the effect of multilayer graphene loading on the photocatalytic activity of MLG/ZnO nanocomposite. This was done to achieve optimum conditions of the samples so that high degradation rate of the samples could be met.

In Figure 4.15a graph named BB ONLY shows the absorption spectrum of BB after sunlight irradiation in the absence of a photocatalyst. It was observed that there was an insignificant change in the absorption peak of BB in the absence of the photocatalyst after 180 min of sunlight irradiation. Therefore, it can be concluded that photolysis of organic pollutants is negligible since these dyes are highly stable and remain unchanged even after they are exposed to direct sunlight for chemical treatment. This step was necessary in order to perfectly assess the impact of the photocatalyst in degrading the organic pollutant and to observe the degree of photolysis. For all measurements the adsorption desorption condition conducted in the dark was labeled 0 min in the plots. Figure 4.15 shows the absorption spectra of BB irradiated in the presence of the catalysts as labelled.

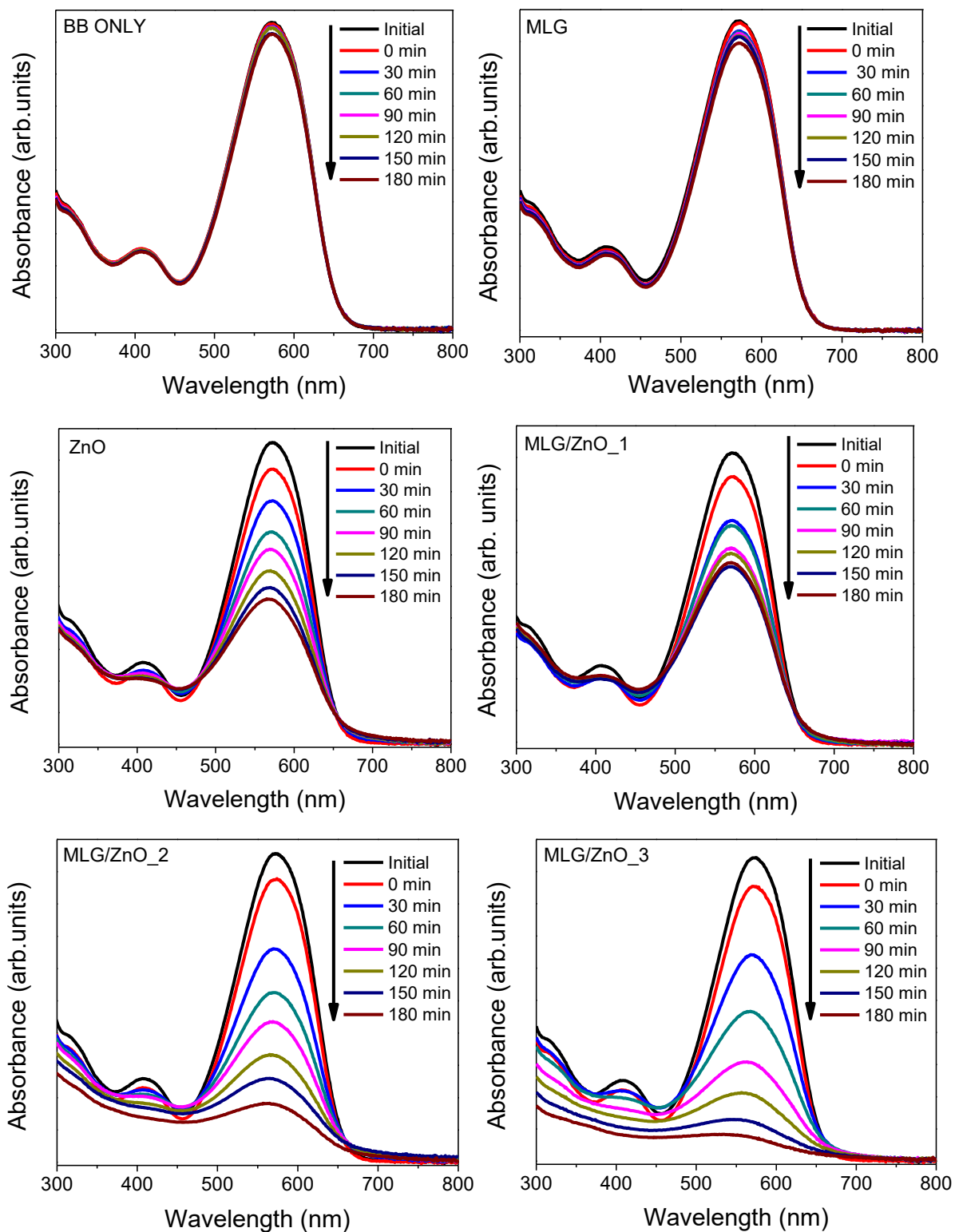


Figure 4.15: Absorbance spectra for the degradation of BB in the absence of a catalyst and in the presence of MLG, ZnO, MLG/ZnO_1, MLG/ZnO_2 and MLG/ZnO_3.

The percentage degradation of the dye was calculated using:

$$\%degradation = \frac{C_0 - C_t}{C_0} * 100 \quad (4.24)$$

where C_t is the concentration of BB after sampling time, t in min and C_0 is the initial concentration of the dye before degradation. The percentage degradation of BB against time of irradiation using different photocatalysts is shown in Figure 4.16. The calculated percentage degradations of BB by all photocatalysts after 30 and 180 min are illustrated in Table 4.6. The percentages of degradation by MLG, ZnO, MLG/ZnO_1, MLG/ZnO_2 and MLG/ZnO_3 were 7.0, 63, 39.1, 82 and 93% respectively.

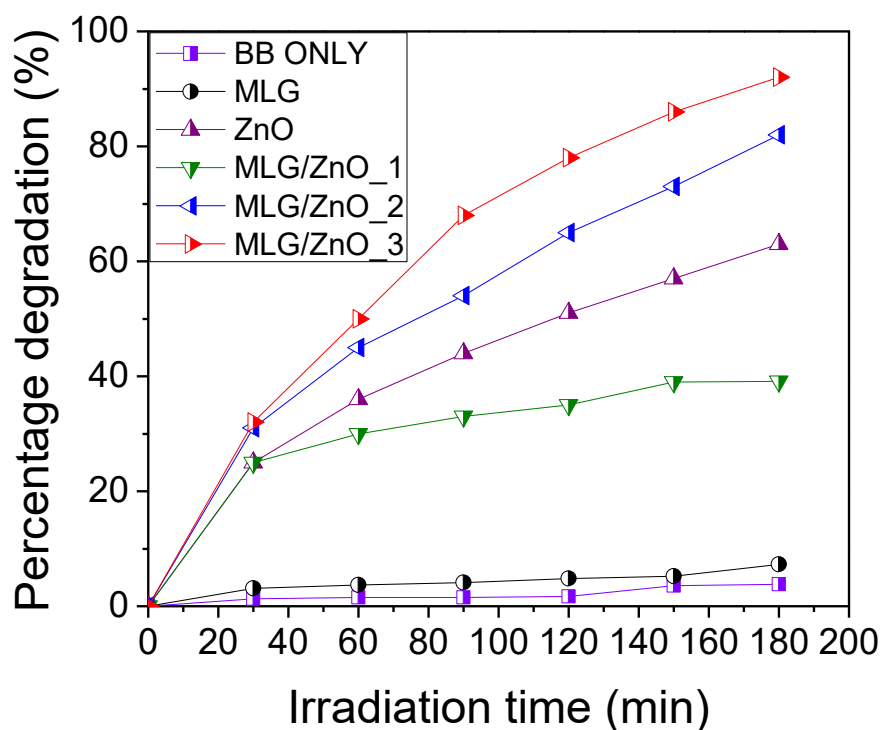


Figure 4.16: A graph of percentage degradation of BB as a function of time photocatalyzed by different samples as indicated.

Table 4.6: Percentage degradation after 30 and 180 min of sunlight irradiation

Photocatalyst	Percentage Degraded (%)	
	30 min	180 min
BB ONLY	1.5	3.8
MLG	3	7
ZnO	25	63
MLG/ZnO_1	25	39
MLG/ZnO_2	31	82
MLG/ZnO_3	32	93

In the absence of the catalyst, only 3.8% of BB was degraded after 3 h of sunlight irradiation. MLG/ZnO_3 showed a better photocatalytic performance than pure ZnO registering a greater photodegradation efficiency of 93% as compared to pure ZnO at 63%. It was clear that there was insignificant photolysis of the dye in the presence of MLG implying that bare MLG was a poor photocatalyst for the dye. The quantitative photocatalytic efficiency of BB by the different samples was evaluated by plotting the absorbance C_t/C_0 against irradiation time as shown in Figure 4.17.

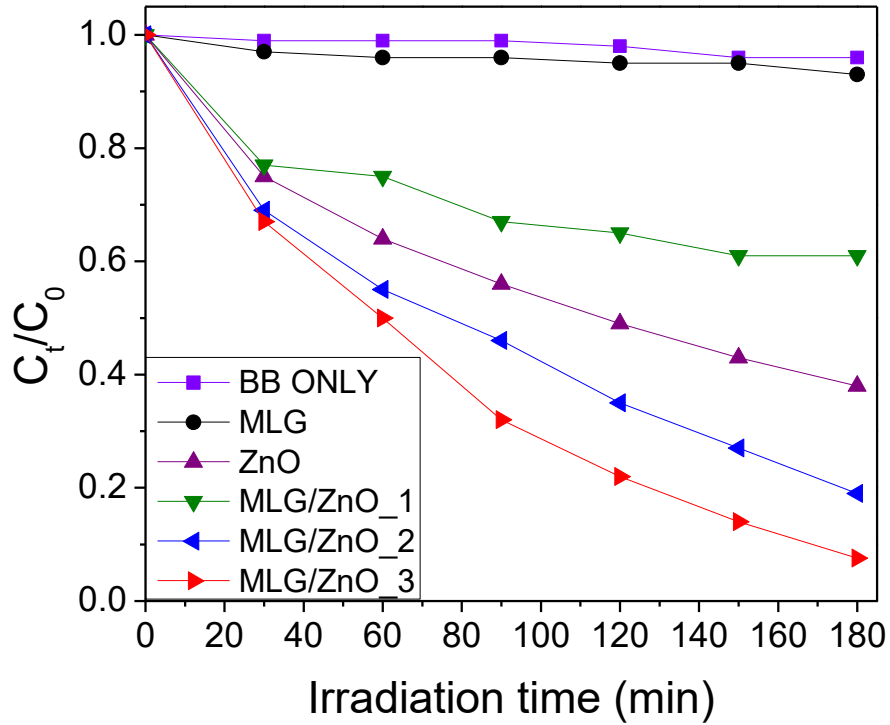


Figure 4.17: Photocatalytic degradation of BB by different photocatalysts as indicated.

The photocatalytic degradation kinetics of BB by as-synthesized materials were studied using Langmuir-Hinshelwood model [159]. The Langmuir-Hinshelwood (LH) expression explains the kinetics of heterogeneous catalytic systems and is given by;

$$r = -\frac{dC}{dt} = \frac{k_r KC}{1+KC} \quad (4.25)$$

where r represents the rate of reaction that changes with time, k_r is the reaction rate constant, C is the concentration of BB at any time t during degradation and K is the equilibrium constant for adsorption of the substrate onto the catalyst.

The concentration of BB used was 10.85 mg/L, which is relatively low. If the concentration is low K is small and negligible. Therefore, $KC \ll 1$ then equation (4.25) becomes;

$$r = k_r KC \quad (4.26)$$

Integrating equation (4.26) using limits of $C=C_0$, $t=0$ and $C=C$ at $t=t$, the LH expression reduces to a first order kinetics and is given by;

$$-\ln\left(\frac{C_t}{C_0}\right) = k_{app}t \quad (4.27)$$

where C_0 is the initial concentration of the azo dye in mg/L, k_{app} is the rate constant of the pseudo first order reaction. The reaction rate (k) was calculated by plotting the graph of $-\ln(C_t/C_0)$ against irradiation time, t in min as illustrated in Figure 4.18. The perfect linear fit shows that the photodegradation of BB was a pseudo first order kinetic reaction. The rate constant was calculated to be 0.0003, 0.0049, 0.0021, 0.0084 and 0.0137 min^{-1} for MLG, ZnO, MLG/ZnO_1, MLG/ZnO_2 and MLG/ZnO_3 respectively as presented in Table 4.7.

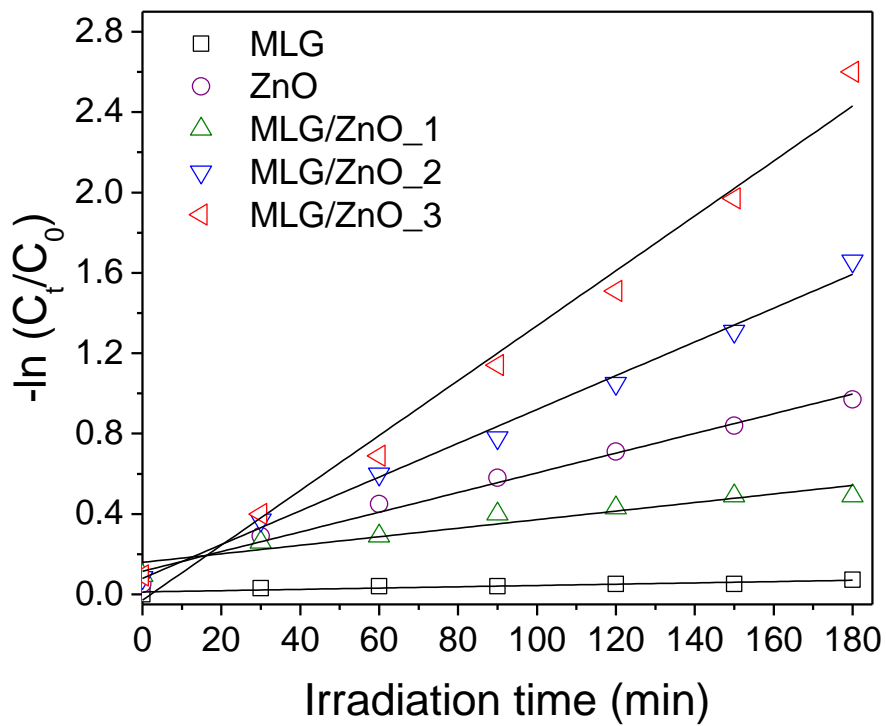


Figure 4.18: A Langmuir-Hinshelwood plot for obtaining the reaction rate.

Table 4.7: Apparent rate constants for photodegradation of BB.

Photocatalyst	Photodegradation rate (K_{app}) (min^{-1})
BB ONLY	0.00018
MLG	0.0003
ZnO	0.0049
MLG/ZnO_1	0.0021
MLG/ZnO_2	0.0084
MLG/ZnO_3	0.0137

According to literature [24,29,113] an increase in surface area provides more active sites on the surface of the nanomaterials thus increasing the photocatalytic activity. Previous reporters [24,28], have indicated that heterogeneous photocatalysis occurs on the surface of a photocatalyst. However, photocatalytic activity of metal oxides does not depend on surface area only but on several factors including particle size, crystallinity, phase structures and photo-quantum efficiency. MLG had the least percentage degradation of BB compared to other samples besides having a larger surface area hence proving that photocatalytic activity is not a function of surface area alone [25]. Similar results have been reported by Atchudan et al [160]. The lower reaction rate of MLG is due to the accumulation of electrons on the multilayer graphene surface and electron-active dye recombination [22]. The experiment with MLG/ZnO_1 as the photocatalyst shows a decreased photocatalytic dye degradation activity this is because increase in MLG content reduces accessibility of ZnO active sites available for visible light irradiation leading to deficiency of electrons which results in lower photocatalytic activity [161]. Bare ZnO had a lower reaction rate of 0.0049 cm^{-1} as compared to when dispersed in a composite (MLG/ZnO_2 and MLG/ZnO_3). This is because of less surface area in the bare ZnO due to agglomeration and increased surface area after dispersing in the composites. This agrees with BET results which showed an increase of surface area of ZnO from 0.42 to $148.74 \text{ m}^2/\text{g}$ in MLG/ZnO_3 composite. The low reaction rate of ZnO may also be due to the fast recombination of

the photogenerated charge carriers as well as its slow photo-response towards solar spectrum light [162]. The optimized incorporation of MLG and ZnO in a composite prevents charge carriers recombination on the surface of ZnO NPs [22,160] hence an improved photocatalytic performance of MLG/ZnO_2 and MLG/ZnO_3. The MLG/ZnO_2 and MLG/ZnO_3 nanocomposites showed a significant higher photocatalytic activity due to the increased surface area contributed by the multilayer graphene sheets. The SEM images revealed well dispersed ZnO nanorods on the multilayer graphene sheets. It is evident that multilayer graphene sheets inhibit ZnO agglomeration and this promotes effective photo-generated charge transfer and hinders electron-hole pair recombination, which improves photocatalytic efficiency [93,163]. As already mentioned, that this study focused on improving the photocatalytic activity of ZnO by incorporating it with multilayer graphene at different ratios of MLG to ZnO for optimum conditions. The percentage degradation of BB increased with an increase in the ZnO content in the MLG/ZnO nanocomposite. The results are supported by previous researchers [24,29] who reported improved photocatalytic efficiency when the content of carbon-based materials was lower than that of the semiconductor metal oxide (SMO) under study.

Furthermore, enhanced photocatalytic activity of the composites is also due to the contribution of both the SMO photocatalyst and the carbon-based material. The presence of ZnO leads to generation of electrons that can be transferred from the excited dye (dye*) to multilayer graphene or from the conduction band of ZnO to multilayer graphene and can generate massive reactive oxygen species (ROs) that oxidize the dye molecules [164]. Graphene was chosen as an ideal carbon material because of its large surface area (1144.52 m²/g from BET results), enhanced electrical and thermal conductivity, high charge carrier mobility thus it is an electron acceptor and hence prevents e-/h+ recombination [103,165-167]. The nanocomposite MLG/ZnO_3 exhibited faster photodegradation of BB because it possessed optimum value of surface area which accounts for enhanced photodegradation of the dye with maximum efficiency. Therefore, there was a need to optimize the concentration of

MLG to ZnO ratio since both surface area and recombination rates are crucial in photocatalytic degradation process.

As indicated in Chapter 3, section 3.3.1, the CR and RhB were also used as model organic pollutants in this study. CR was selected as a second model pollutant because is an anionic diazo dye with a complex molecular structure hence making it more stubborn to degrade. It has always been a major concern to remove CR from the environment and would be wiser to explore potential photocatalysts with higher degradation efficiencies for this dye. As mentioned before RhB is one of the highly stable, toxic dyes that causes irritation to eyes and skin hence should be removed from the environment [118]. Pristine ZnO and MLG/ZnO_3 were further used to degrade these pollutants to study their photocatalytic efficiency. The MLG/ZnO_3 was chosen as it was observed as the optimum composite. The photocatalytic potentials of the two samples on CR and RhB was examined by monitoring their absorbance profiles. CR and RhB dye degradations were carried out in the absence and presence of the photocatalysts. Figure 4.19a-f shows the absorption profiles of the degraded pollutants in the presence of sunlight for 180 min.

The CR absorption profiles (Figure 4.19c and d) displayed absorption peaks at 235, 347 and 497 nm. It is worth to note that there was no obvious absorption peak shift of the dye. The small absorption bands at 235 and 347 nm symbolize the benzene and naphthalene rings while the one at 497 nm corresponds to the azo bond of CR [168]. However, the photocatalytic degradation of CR was monitored by observing the decrease in the absorption band located at $\lambda=497\text{nm}$. The dye degradation was also observed from the discoloration of the dye. It changed from reddish to colourless depending on the catalyst used. It is worth to note that ZnO and MLG/ZnO_3 showed differences in the degradation of CR dye. The percentage degradations of CR and RhB after 30 and 180 min are illustrated in Table 4.7. 71% and 86% degradation were calculated for ZnO and MLG/ZnO_3 photocatalysts, respectively after 180 min of degradation.

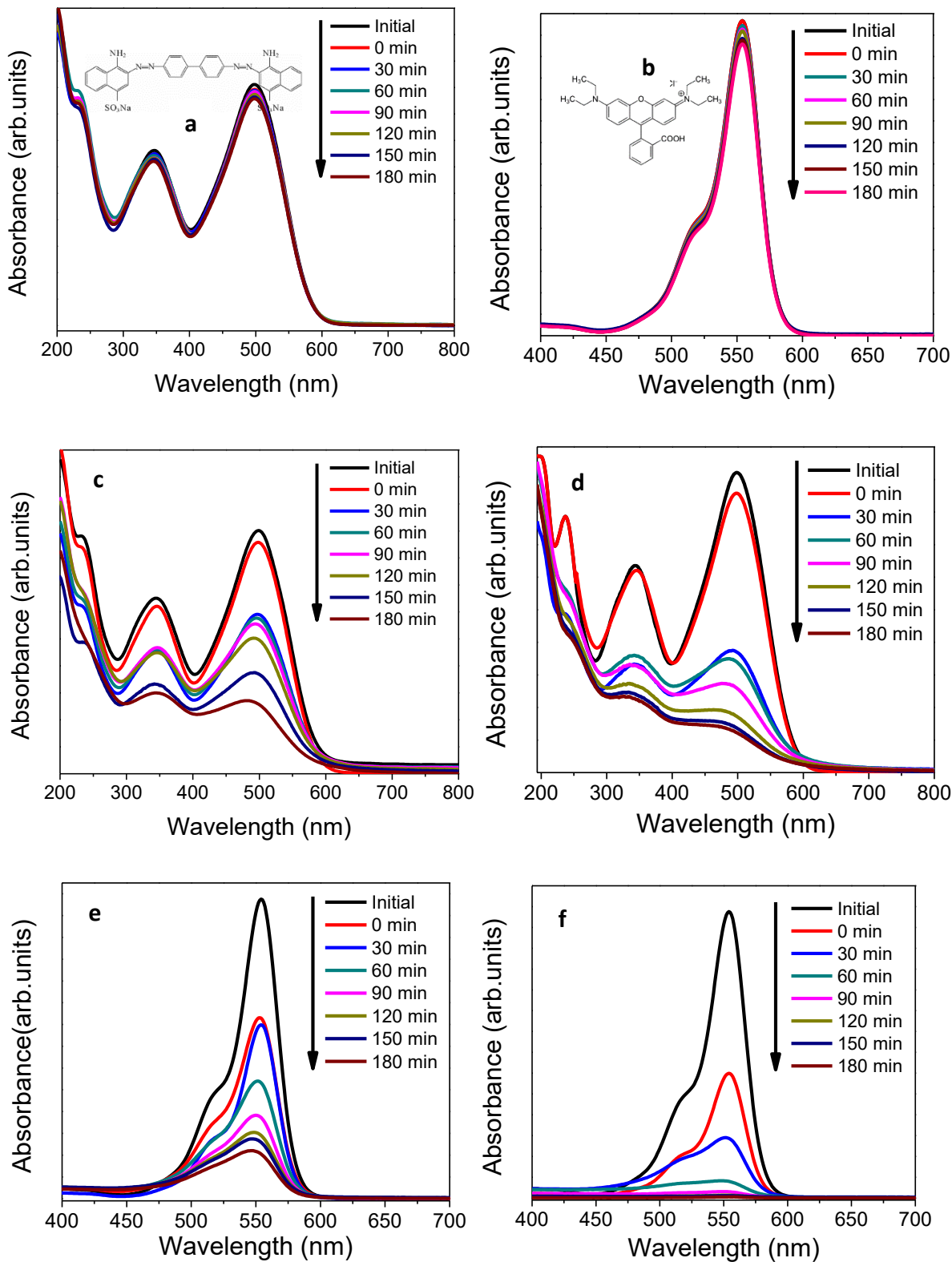


Figure 4.19: Absorption profiles of CR and RhB in a) and b) absence of catalysts, c) and e) presence of ZnO, d) and f) presence of MLG/ZnO₃.

The molecular structural property of the dye changes as a function of degradation time. The decrease in the concentration of the dye with increase in irradiation time indicates the destruction of CR chromophoric structure in the vicinity of azo linkage. Moreover, the decrease in the absorbance values is ascribed to the attack by the $\cdot\text{OH}$ radicals.

As evident from the absorption spectra, RhB displayed a maximum absorption peak at 554 nm. According to Figure 4.19, the absorption peak intensity gradually decreases during photodegradation of the dye molecule through aromatic ring opening. The use of both ZnO and MLG/ZnO₃ did not result in any wavelength shift during the degradation of RhB and this shows that the degradation involved destruction of aromatic chromophore and not de-ethylation of RhB [95]. It is worth to note that in the absence of the photocatalysts, the photodegradation rate of both pollutants was extremely low with percentage degradations of 6.0% and 7.5% for CR and RhB, respectively. This indicates that the photo-induced photolysis of both pollutants was negligible. ZnO showed a greater photocatalytic degradation of RhB at 85% after 180 min as compared to 71% for CR. Furthermore, MLG/ZnO₃ nanocomposite displayed a remarkable improvement in the photodegradation of RhB as its absorption peak totally disappeared after 180 min of sunlight irradiation with a percentage degradation of 100%. MLG/ZnO₃ still proved to be the best photocatalyst in degrading CR and RhB than pure ZnO. The degradation percentages of CR and RhB against time of irradiation using ZnO and MLG/ZnO₃ as photocatalysts are shown in Figure 4.20. The photocatalytic degradation of CR and RhB by the two photocatalysts is displayed in Figure 4.21.

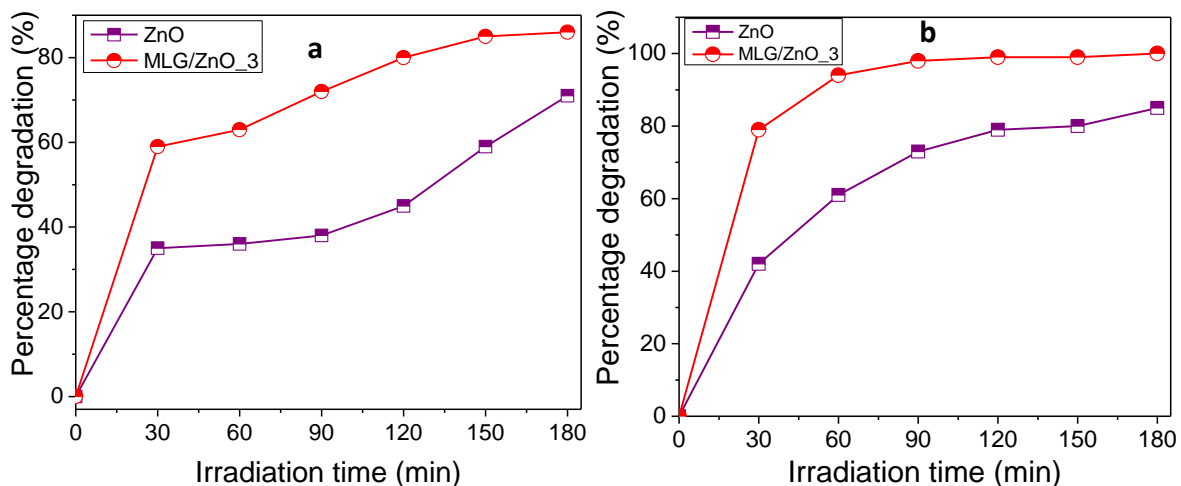


Figure 4.20: Percentage degradation of a) CR and RhB by ZnO and MLG/ZnO₃.

Table 4.8: Percentage degradations of CR and RhB after 30 and 180 min of sunlight irradiation.

Photocatalyst	Dye	Percentage Degraded (%)	
		30 min	180 min
ZnO	CR	25	71
	RhB	25	85
MLG/ZnO ₃	CR	25	86
	RhB	25	100

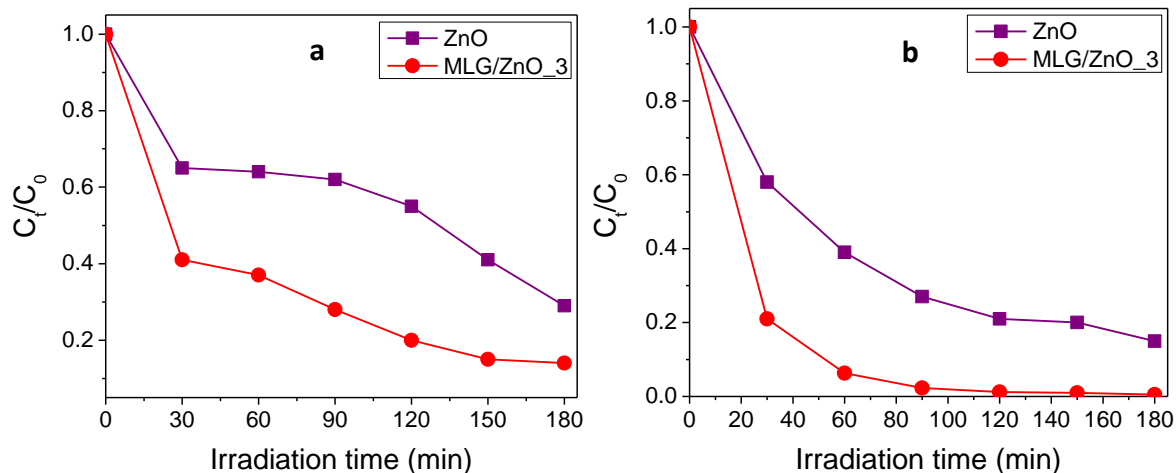


Figure 4.21: Photocatalytic degradation of a) CR and b) RhB by ZnO and MLG/ZnO₃.

The photocatalytic degradation kinetics of CR and RhB by ZnO and MLG/ZnO₃ was studied using Langmuir-Hinshelwood model (equation 4.25). Equation (4.27) was used to show the relationship between photocatalytic degradation of CR and RhB as a function of irradiation time which mimics the kinetics of the reaction. The kinetic analysis of CR and RhB photodegradations are illustrated in Figure 4.22. A straight line was obtained giving a linear relationship suggesting that the photocatalytic degradation of CR and RhB follows the first-order kinetics. Pristine ZnO NPs exhibited a k_{app} of 0.006 and 0.008 min^{-1} for CR and RhB, respectively. Moreover, the rate constants for degradation of CR and RhB by MLG/ZnO₃ were calculated to be 0.01 and 0.028 min^{-1} , respectively as shown in Table 4.9.

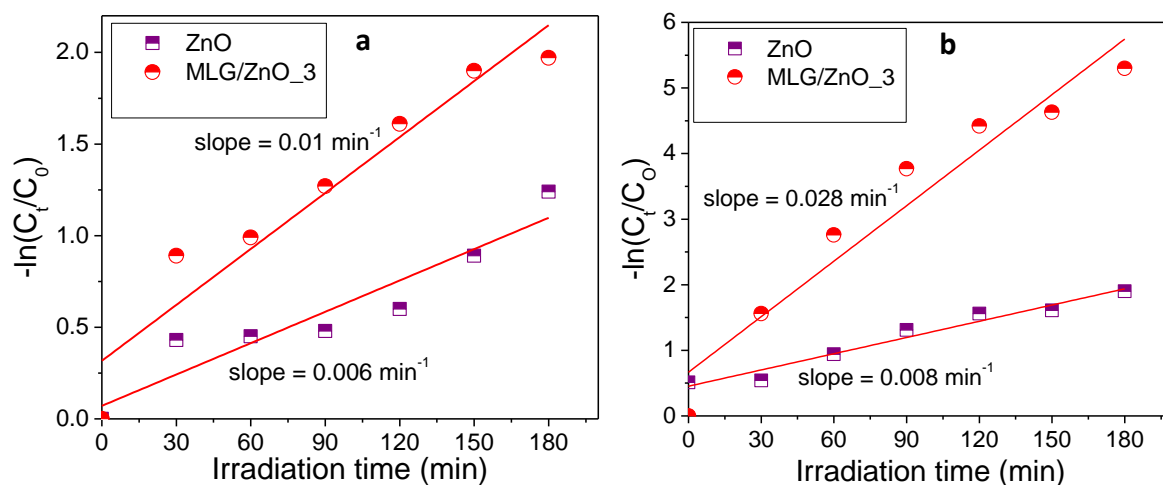


Figure 4.22: Kinetic plots for the photocatalytic degradation of a) CR and b) RhB.

Table 4.9: Apparent rate constants for photodegradation of CR and RhB.

Photocatalyst	Dye	Photodegradation rate (K_{app}) (min^{-1})
ZnO	CR	0.006
	RhB	0.008
MLG/ZnO_3	CR	0.01
	RhB	0.028

It is worth to note that the photodegradation of RhB by both ZnO and MLG/ZnO_3 was faster than the degradation of CR. It was easy to degrade RhB since it is a cationic xanthene dye, and these kinds of dyes have poor lightfastness as compared to other chromophores [169]. The cationic xanthenes therefore discolor easily when exposed to light. Again, the oxidation of RhB was easier than of CR because of its lower molecular weight and simpler structure of the dye molecule compared to CR. It was difficult to degrade CR because of its complex diazo bond. The photodegradation results showed that MLG/ZnO_3 nanocomposite is the most effective catalyst to degrade various pollutants as it showed an enhanced photocatalytic efficiency than pristine ZnO in

degrading BB, CR and RhB.

4.3.2 Recyclability test

The photochemical stability of photocatalysts is very crucial for practical applications. The recyclability experiments were conducted on ZnO and MLG/ZnO₃ using BB as a model pollutant. A set of 3 tests were performed to study the photostability of ZnO and MLG/ZnO₃ and the results are illustrated in Figure 4.23. The photocatalyst was recovered after each cycle, washed, centrifuged and dried before reuse. A decrease in photocatalytic activity of ZnO was observed after 3 cycles due to photo-corrosion effect of BB on the ZnO [29,170]. It was noted that the photodegradation activity of MLG/ZnO₃ was more stable with maximum efficiency decreasing from 93% to 90% compared to 63% to 47% for pure ZnO. This indicates that the incorporation of ZnO with MLG does not only enhance its photocatalytic activity but also boosts its stability during photodegradation experiments.

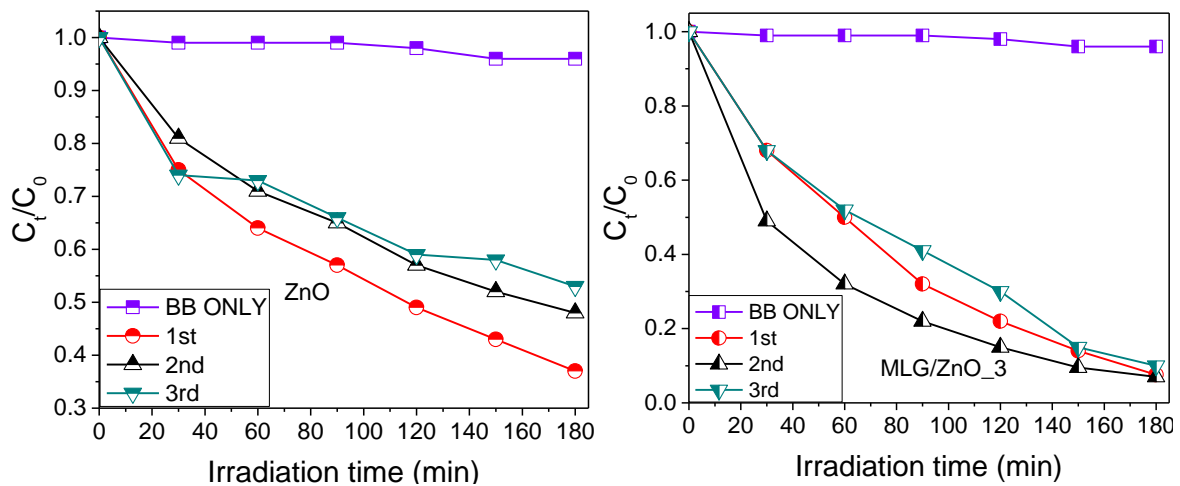


Figure 4.23: Recyclability test for ZnO and MLG/ZnO₃ photocatalysts.

4.3.4 Photocatalytic degradation of DOX, a common antibiotic

DOX is one of the most consumed drugs hence is one of the major environmental contaminants. Therefore, this study also focuses on using cheap and efficient methods to remove it from wastewaters. The photodegradation efficacy of MLG/ZnO₃ nanocomposite was further studied by using DOX solution as a model contaminant. The photocatalytic degradation reaction was conducted under UV irradiation for 300 min and the outcome is illustrated in Figure 4.24.

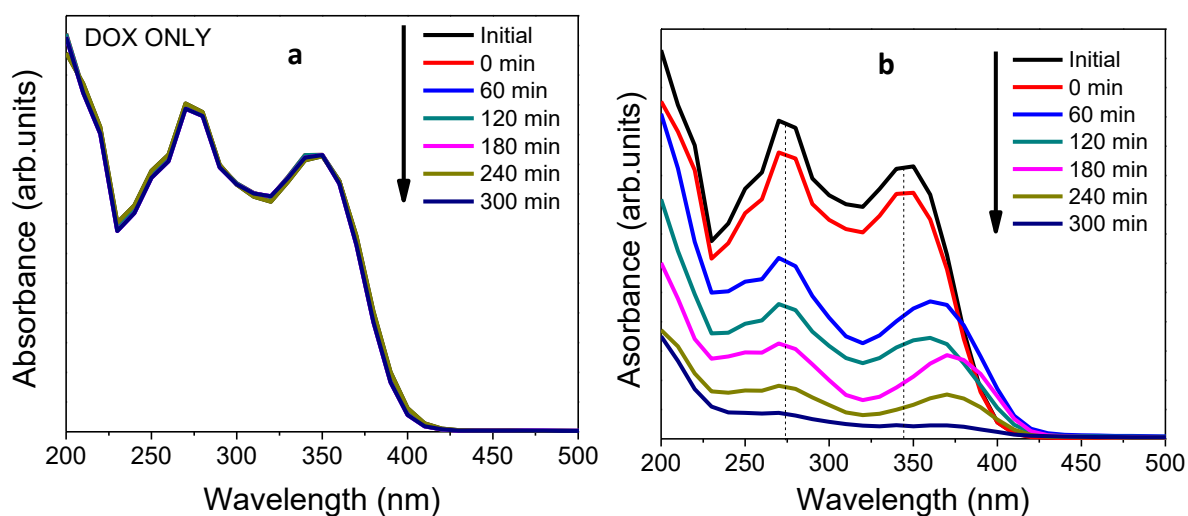


Figure 4.24: Changes in UV-Vis absorption spectrum of aqueous DOX solution under UV irradiation a) without catalyst and b) in the presence of MLG/ZnO₃.

The absorption spectra of DOX before irradiation exhibit two major absorption peaks at 273 and 344 nm. The absorption band at 344 nm red shifts to 363 and 374 nm after 60 and 180 min of irradiation, respectively. This red shift is due to the interaction of DOX solution with MLG/ZnO₃ NPs. The absorption bands slowly decreased with increase in irradiation time indicating the degradation of the drug. The disappearance of the absorption band at 273 nm was ascribed to the production of acylamino and

hydroxyl groups [13,171]. The photodegradation efficiency of DOX was computed using equation (4.24). The percentage degradation of DOX as a function of irradiation time is illustrated in Figure 4.25. DOX solution was found to be stable in the absence of the photocatalyst even after 300 min of UV irradiation with an insignificant degradation efficiency of 1.3%. Furthermore, the photodegradation of DOX was found to be 95% after 300 min of irradiation in the presence of MLG/ZnO₃ composite.

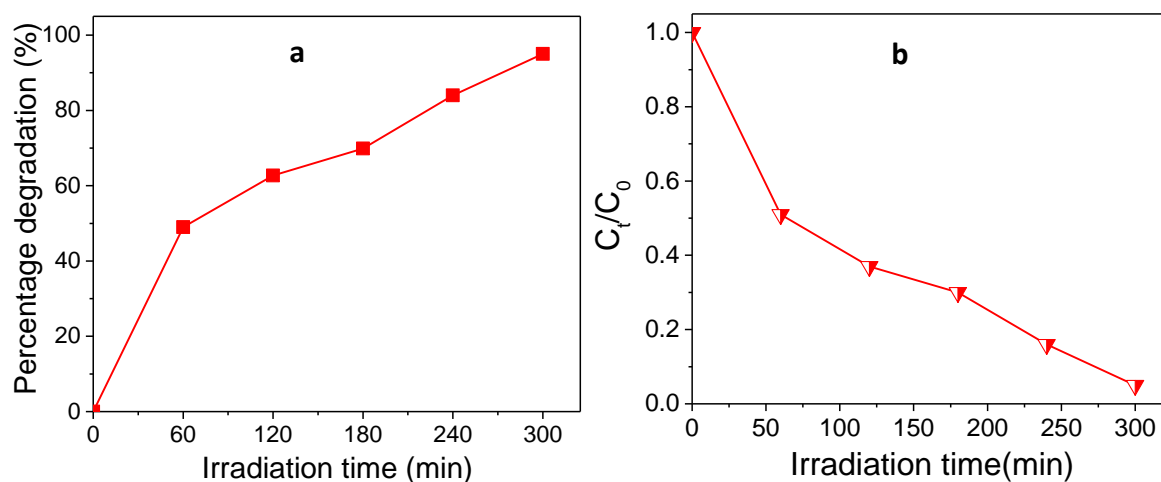


Figure 4.25: a) Percentage degradation of DOX as a function of time photocatalyzed by MLG/ZnO₃ and b) Photocatalytic degradation of DOX by MLG/ZnO₃.

The photocatalytic degradation kinetics of DOX were also studied using LH model and were fitted using the first order rate equation (4.27). The rate constant was calculated to be 0.0086 min^{-1} for the degradation of the drug. The rate constant graph is shown in Figure 4.26. According to Klauson et al [172] DOX is a tetracycline antibiotic. Addamo et al [173] states that when tetracycline photo decomposes, it forms many decomposition compounds which includes side chain degradations by deamination, desulfuration and dealkylation. Moreover, the degradation of volatile dimethylane requires the loss of only 2 carbon atoms according to the 22 atoms of tetracycline [13].

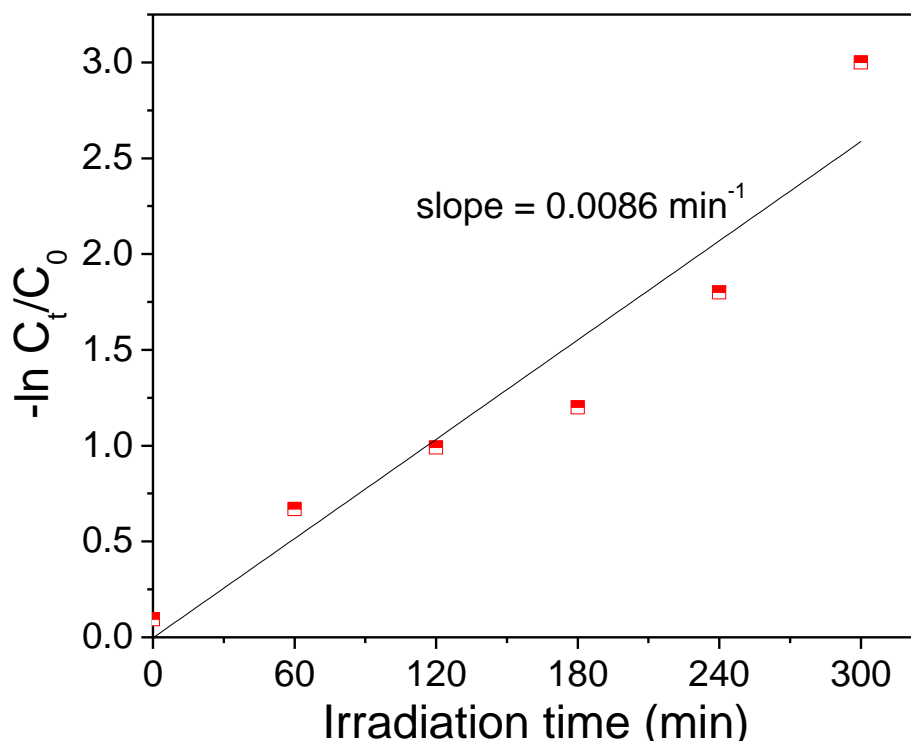


Figure 4.26: Kinetic plot for the photodegradation of DOX.

It is worth to note that the MLG/ZnO₃ nanocomposite can be used to degrade various pollutants with a remarkable photocatalytic efficiency including DOX. Furthermore, the results are in agreement with previous researchers [24,30,106,162,174] who conducted similar experiments for removal of various pollutants by incorporating MLG with ZnO for enhanced photocatalytic activity. As already mentioned with organic dyes MLG sheets promote efficient and selective adsorption of the pollutant molecules on its surface. Incorporation of ZnO and MLG in a composite structure allow adsorption of the photogenerated electron from valence band of ZnO by MLG. This hinders the recombination of the generated holes and electrons subsequently allowing the hole to produce enough hydroxyl radicals to degrade the pollutant molecules [16]. The increase in the photocatalytic activity can also be due to the contribution of the MLG surfaces of injecting a photo-induced electron to the conduction band of ZnO NPs. The generated electron can trigger formation of reactive superoxide radical ions and hydroxyl radicals [175].

4.3.3 Mechanism of photocatalytic degradation

The photodegradation mechanism for this study was demonstrated on one model pollutant (BB). A mechanism for the photodegradation of BB was proposed and is shown in Figure 4.27. When the semiconductor, ZnO is exposed to sunlight the photon energy excites the electron in the valence band (VB) to jump to the conduction band (CB) creating holes in the valence band. The excitation of the electron results in generation of a pair of charge carriers (e^-/h^+ pairs) on the surface of ZnO. The minimum energy required for excitation of an electron is equivalent to the band gap energy. The produced charge carriers can undergo recombination, or directly interact with the organic pollutant or react further on the surface of the photocatalyst to result in secondary products. The photogenerated electrons reacts with oxygen (O_2) to produce superoxide anion radicals ($O_2^{\cdot-}$). The generated holes (h^+) react with water molecules (H_2O) to form hydroxyl radicals ($\cdot OH$). The adsorbed pollutants onto the surface of MLG/ZnO nanocomposite are then degraded by the generated radicals to nontoxic products like CO_2 and H_2O [18,162].

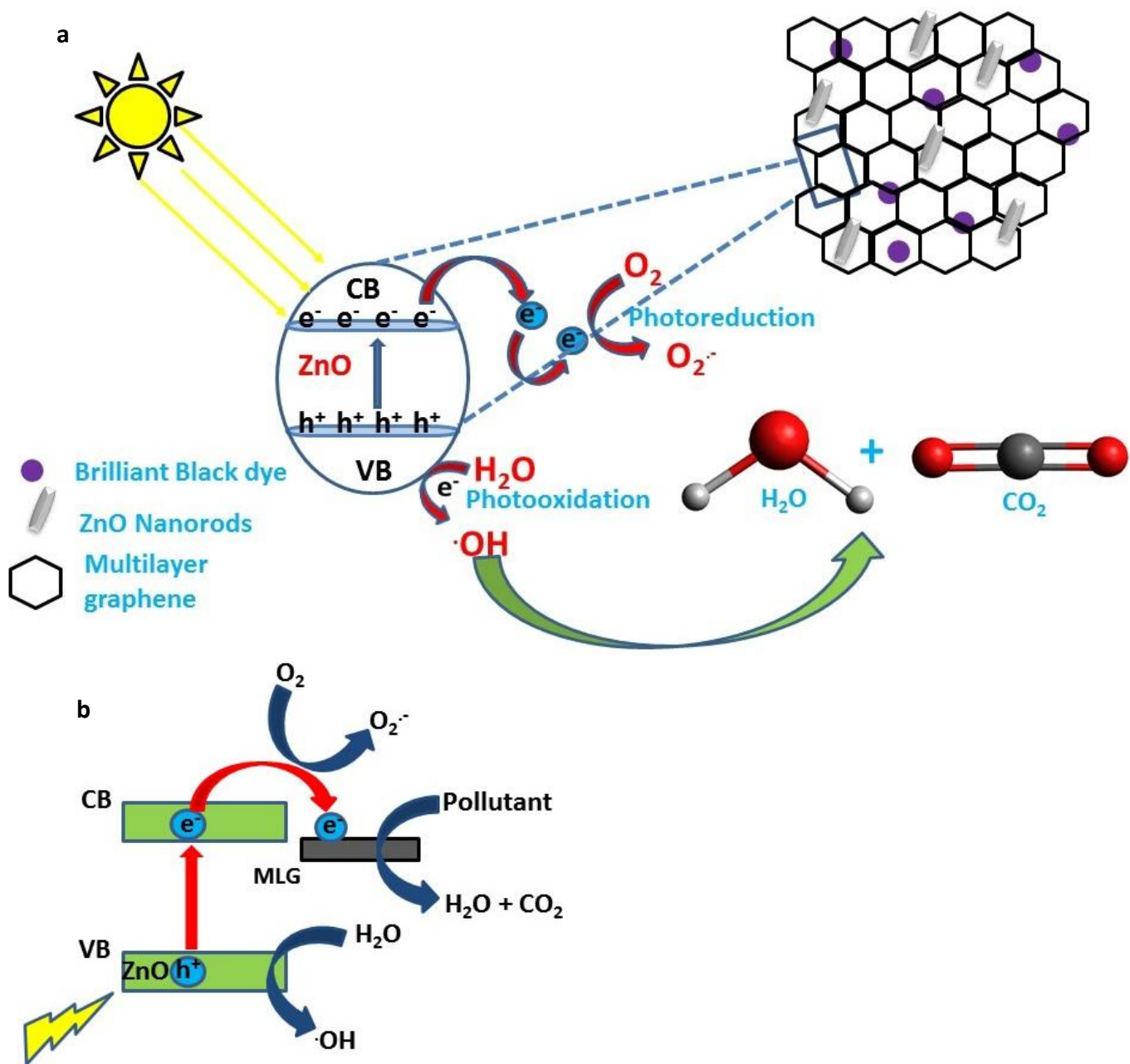


Figure 4.27: a) Mechanism of photocatalytic reaction of MLG/ZnO and b) band gap diagram for MLG/ZnO composite.

Scavenging experiments were conducted to detect the reactive species that played the major role in photocatalytic activities for easy understanding of the photocatalytic mechanism of MLG/ZnO_3 in degradation of the four pollutants. The reactive species were

eliminated by adding t-BuOH ($\cdot\text{OH}$ scavenger), EDTA (h^+ scavenger) and p-BQ ($\text{O}_2^{\cdot-}$) into the reaction solution, respectively. The degradation percentages of the pollutants in the presence and absence of scavengers is shown in Figure 4.28 and summarized in Table 4.10. The percentage degradation of BB, CR, RhB and DOX without scavengers were computed to be 93, 86, 100 and 95% respectively but reduced to 76, 82, 96 and 89% after EDTA was added to the reaction solution. The degradation percentages further decreased to 81, 76, 98 and 90% for BB, CR, RhB and DOX, respectively after addition of t-BuOH. A minimum degradation percentage was calculated for CR, RhB and DOX at 42, 85 and 86%, respectively after addition of p-BQ. But a percentage degradation of 81% was recorded with BB in the presence of p-BQ. It can be concluded that superoxide radicals were the major reactive radical species for the degradation of CR, RhB and DOX. Furthermore, it was established that holes play a major role in the degradation of BB. Therefore, a decrease in the percentage degradation of BB in the presence of scavengers is described by the trend: EDTA > p-BQ > t-BuOH. Moreover, CR and DOX experienced photodegradation decrease of the following trend: p-BQ > t-BuOH > EDTA, whereas the decrease in the percentage degradation of RhB was p-BQ > EDTA > t-BuOH. In conclusion the scavenging experiments revealed that the mechanism of MLG/ZnO_3 for the degradation of CR, RhB and DOX is the same since the major degradation pathway of MLG/ZnO_3 is through the decomposition of all the three pollutants by ($\text{O}_2^{\cdot-}$). It is also worth to note that BB was mainly decomposed by holes.

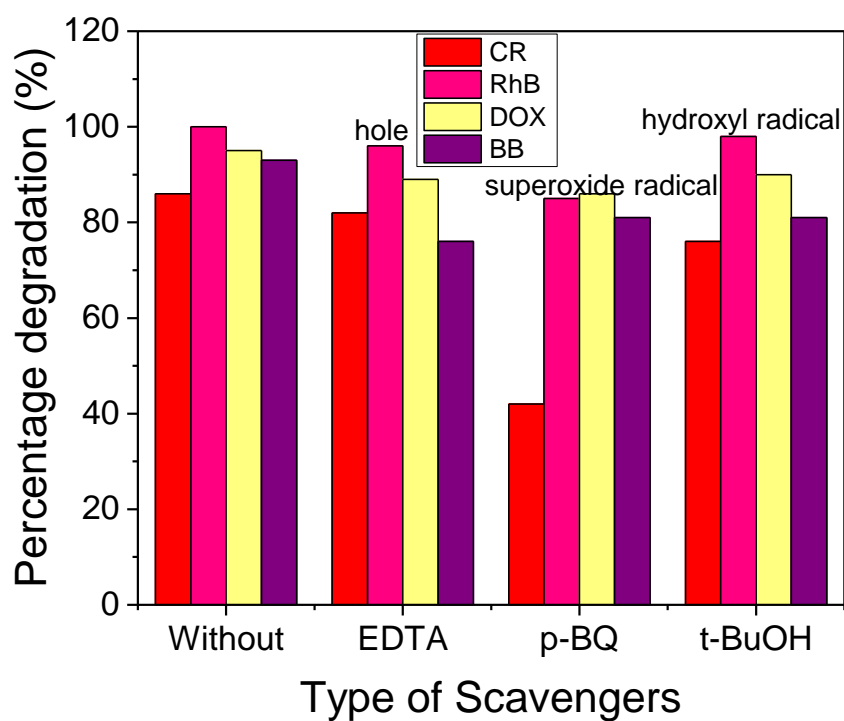


Figure: 4.28: Percentage degradation of CR, RhB, DOX and BB by MLG/ZnO₃ nanocomposite in the absence and presence of various scavengers.

Table 4.10: Percentage degradation of BB, CR, RhB and DOX by MLG/ZnO nanocomposite in the absence and presence of various scavengers.

Pollutant	Percentage Degraded (%)			
	Without Scavenger	EDTA	p-BQ	t-BuOH
BB	93	76	81	81
CR	86	82	42	76
RhB	100	96	85	98
DOX	95	89	86	90

CONCLUSION AND RECOMMENDATIONS

5.1 Conclusion

This study demonstrated a simple and cost-effective green method to synthesize ZnO NPs using *A. Houstonianum* leaf extract as a natural precursor. MLG was successfully synthesized from cellulose extracted from corn husk. Three MLG/ZnO nanocomposites with different concentrations of MLG to ZnO content were successfully synthesized through *ex-situ* casting of the materials to eliminate use of capping agents and for energy saving purposes and to further demonstrate the spirit of green nanotechnology. The presence of MLG and ZnO in the composites was confirmed by XRD, Raman, SEM, HRTEM and BET. XRD and Raman analysis shows that ZnO particles in all the samples were of single phase of wurtzite, therefore the presence of MLG in the composite did not change the hexagonal wurtzite structure of ZnO. The Scherrer, Williamson-Hall, Halder-Wagner and Wagner-Agua equations were used to analyze and compare the crystallite sizes and lattice strains. It was found that the crystallite sizes increased with the increase in the ZnO content in the composites.

Short hexagonal nanorods and sheet-like structure with ripples and crinkles on the edges were observed through SEM and HRTEM analysis of ZnO and MLG, respectively. HRTEM analysis also revealed polycrystalline structure of ZnO with SAED diffraction rings matching XRD results. The EDS spectrum confirmed the presence of C, O and Zn in the composites hence verified the successful incorporation of MLG and ZnO. The BET surface area of MLG, ZnO and MLG/ZnO_3 were computed to be 1144.52, 0.42 and 148.74 m²/g. The optical band gap computed based on Tauc's plots were 2.08, 3.09, 2.66, 2.75 and 2.80 eV for MLG, ZnO, MLG/ZnO_1, MLG/ZnO_2 and MLG/ZnO_3, respectively implying it increased with increase in ZnO content in the nanocomposites. The photocatalytic degradation of three organic dyes, Brilliant black, Congo red and Rhodamine B was investigated in the presence and absence of photocatalysts under sunlight irradiation.

BB was initially used for optimization to determine the best catalyst amongst the three composites. The reaction rate constant of MLG, ZnO, MLG/ZnO_1, MLG/ZnO_2 and MLG/ZnO_3 were 0.003, 0.0049, 0.0021, 0.0084 and 0.0137 cm^{-1} , respectively. The photocatalytic experiments showed that MLG/ZnO_3 had higher photocatalytic degradation (93%) of BB than pure ZnO (63%). The photocatalytic efficiency of the best composite (MLG/ZnO_3) and pristine ZnO were further explored on CR and RhB. The photocatalytic degradation of CR and RhB by MLG/ZnO_3 gave maximum degradations of 86 and 100%, respectively while pure ZnO gave degradations of 71 and 85% for CR and RhB, respectively. The reaction rate constants of CR and RhB by MLG/ZnO_3 were found to be 0.01 and 0.028 min^{-1} , respectively, whereas the reaction rate constants of CR and RhB by ZnO were 0.006 and 0.008 min^{-1} , respectively. MLG/ZnO_3 was further used to degrade DOX under UV light with percentage degradations of 95% after 300 min of irradiation and reaction rate constant of 0.0086 min^{-1} . Moreover, radical scavenging experiments by MLG/ZnO_3 photocatalyst were conducted on all the four pollutants. The main radical species in decomposition of BB were found to be positively charged photogenerated holes while for CR, RhB and DOX was discovered to be superoxide ions.

It can be concluded that the photocatalytic activity is influenced by the rate of electron-hole recombination as well as the surface area of the photocatalyst. The large surface area and dispersion of ZnO contributed by MLG promoted easy adsorption of organic molecules on the MLG sheets increasing photocatalytic activity. In addition, high electron conductivity of MLG promoted movement of electrons hence accelerating charge transfer. Therefore, MLG provides an invaluable support in promoting the photocatalytic process. This study shows that MLG/ZnO nanocomposite is a potential candidate to be used as a reliable and more effective method for applications in industrial wastewater purifications due to the combined amazing properties of the carbon and semiconductor nanomaterials.

5.2 Recommendations for Future Work

The aims and objectives of this study were successfully achieved, however few suggestions are recommended for future work;

- Experiments should be performed under different solar light conditions to ascertain the effect of weather conditions on the performance of the renewable energy activated photocatalysts especially during winter or cloudy days.
- Optimization of the temperature and pH of the pollutants should also be considered to study their effects on photocatalytic applications.
- Evaluation of the performance of the nanocomposites can be performed on real textile industrial wastewater to assess the efficacy of the materials.
- Other photocatalysts can be anchored on green synthesized multilayer graphene and evaluated for their performance as visible light active photocatalysts.

REFERENCES

- [1] M. Rai, A. Yadav, A. Gade, CRC 675 - Current trends in phytosynthesis of metal nanoparticles, *Crit. Rev. Biotechnol.* 28 (2008) 277–284. <https://doi.org/10.1080/07388550802368903>.
- [2] A. Kumar, K. Gupta, S. Dixit, K. Mishra, S. Srivastava, A review on positive and negative impacts of nanotechnology in agriculture, *Int. J. Environ. Sci. Technol.* 16 (2019) 2175–2184. <https://doi.org/10.1007/s13762-018-2119-7>.
- [3] N.S. El-Gendy, B.A. Omran, Green Synthesis of Nanoparticles for Water Treatment, *Nano Bio-Based Technol. Wastewater Treat.* (2019) 205–263. <https://doi.org/10.1002/9781119577119.ch7>.
- [4] I. Khan, K. Saeed, I. Khan, Nanoparticles: Properties, applications and toxicities, *Arab. J. Chem.* 12 (2019) 908–931. <https://doi.org/10.1016/j.arabjc.2017.05.011>.
- [5] A. Eatemadi, H. Daraee, H. Karimkhanloo, M. Kouhi, N. Zarghami, A. Akbarzadeh, M. Abasi, Y. Hanifehpour, S.W. Joo, Carbon nanotubes: Properties, synthesis, purification, and medical applications, *Nanoscale Res. Lett.* 9 (2014) 1–13. <https://doi.org/10.1186/1556-276X-9-393>.
- [6] S. Ahmed, Annu, S.A. Chaudhry, S. Ikram, A review on biogenic synthesis of ZnO nanoparticles using plant extracts and microbes: A prospect towards green chemistry, *J. Photochem. Photobiol. B Biol.* 166 (2017) 272–284. <https://doi.org/10.1016/j.jphotobiol.2016.12.011>.
- [7] D. Nath, P. Banerjee, Green nanotechnology - A new hope for medical biology, *Environ. Toxicol. Pharmacol.* 36 (2013) 997–1014. <https://doi.org/10.1016/j.etap.2013.09.002>.
- [8] A.M. El Shafey, Green synthesis of metal and metal oxide nanoparticles from plant leaf extracts and their applications: A review, *Green Process. Synth.* 9 (2020) 304–339. <https://doi.org/10.1515/gps-2020-0031>.
- [9] T. Varadavenkatesan, E. Lyubchik, S. Pai, A. Pugazhendhi, R. Vinayagam, R. Selvaraj, Photocatalytic degradation of Rhodamine B by zinc oxide nanoparticles synthesized using the leaf extract of *Cyanometra ramiflora*, *J. Photochem. Photobiol. B Biol.* 199 (2019) 111621. <https://doi.org/10.1016/j.jphotobiol.2019.111621>.
- [10] A.M. Ealias, M.P. Saravanakumar, A review on the classification, characterisation, synthesis of nanoparticles and their application, *IOP Conf. Ser. Mater. Sci. Eng.* 263 (2017). <https://doi.org/10.1088/1757-899X/263/3/032019>.
- [11] S. Sathiyavimal, S. Vasantharaj, D. Bharathi, M. Saravanan, E. Manikandan, S.S. Kumar, A. Pugazhendhi, Biogenesis of copper oxide nanoparticles (CuONPs) using *Sida acuta* and their incorporation over cotton fabrics to prevent the pathogenicity of Gram negative

- and Gram positive bacteria, *J. Photochem. Photobiol. B Biol.* 188 (2018) 126–134. <https://doi.org/10.1016/j.jphotobiol.2018.09.014>.
- [12] T. Purkait, G. Singh, M. Singh, D. Kumar, R.S. Dey, Large area few-layer graphene with scalable preparation from waste biomass for high-performance supercapacitor, *Sci. Rep.* 7 (2017) 1–14. <https://doi.org/10.1038/s41598-017-15463-w>.
- [13] G.H. Safari, M. Hoseini, M. Seyedsalehi, H. Kamani, J. Jaafari, A.H. Mahvi, Photocatalytic degradation of tetracycline using nanosized titanium dioxide in aqueous solution, *Int. J. Environ. Sci. Technol.* 12 (2014) 603–616. <https://doi.org/10.1007/s13762-014-0706-9>.
- [14] E. Moctezuma, E. Leyva, C.A. Aguilar, R.A. Luna, C. Montalvo, Photocatalytic degradation of paracetamol: Intermediates and total reaction mechanism, *J. Hazard. Mater.* 243 (2012) 130–138. <https://doi.org/10.1016/j.jhazmat.2012.10.010>.
- [15] W.Z. Khan, Photodegradation of Real Pharmaceutical Wastewater with Titanium Dioxide, Zinc Oxide, and Hydrogen Peroxide During UV Treatment, *IOSR J. Eng.* 06 (2016) 36–46. <https://doi.org/10.9790/3021-067013646>.
- [16] A. Mohammadi, S. Pourmoslemi, Enhanced photocatalytic degradation of doxycycline using a magnetic polymer-ZnO composite, *Water Sci. Technol.* 2017 (2018) 791–801. <https://doi.org/10.2166/wst.2018.237>.
- [17] A.A. Borghi, M.F. Silva, S. Al Arni, A. Converti, M.S.A. Palma, Doxycycline degradation by the oxidative Fenton process, *J. Chem.* 2015 (2015). <https://doi.org/10.1155/2015/492030>.
- [18] P. Raizada, A. Sudhaik, P. Singh, Photocatalytic water decontamination using graphene and ZnO coupled photocatalysts: A review, *Mater. Sci. Energy Technol.* 2 (2019) 509–525. <https://doi.org/10.1016/j.mset.2019.04.007>.
- [19] S. Prabhu, S. Megala, S. Harish, M. Navaneethan, P. Maadeswaran, S. Sohila, R. Ramesh, Enhanced photocatalytic activities of ZnO dumbbell/reduced graphene oxide nanocomposites for degradation of organic pollutants via efficient charge separation pathway, *Appl. Surf. Sci.* 487 (2019) 1279–1288. <https://doi.org/10.1016/j.apsusc.2019.05.086>.
- [20] V.Q. Nguyen, M.L. Baynosa, V.H. Nguyen, D. Tuma, Y.R. Lee, J.J. Shim, Solvent-driven morphology-controlled synthesis of highly efficient long-life ZnO/graphene nanocomposite photocatalysts for the practical degradation of organic wastewater under solar light, *Appl. Surf. Sci.* 486 (2019) 37–51. <https://doi.org/10.1016/j.apsusc.2019.03.262>.
- [21] M. Samadi, M. Zirak, A. Naseri, E. Khorashadizade, A.Z. Moshfegh, Recent progress on doped ZnO nanostructures for visible-light photocatalysis, *Thin Solid Films.* 605 (2016) 2–19. <https://doi.org/10.1016/j.tsf.2015.12.064>.

- [22] B. Li, T. Liu, Y. Wang, Z. Wang, ZnO/graphene-oxide nanocomposite with remarkably enhanced visible-light-driven photocatalytic performance, *J. Colloid Interface Sci.* 377 (2012) 114–121. <https://doi.org/10.1016/j.jcis.2012.03.060>.
- [23] S. N. Ahmed, W. Haider, Heterogeneous photocatalysis and its potential applications in water and wastewater treatment: a review, *J. Nanot.* 29 (2020) 0–31. <http://doi.org/10.1088/1361-6528/aac6ea>.
- [24] R. Beura, P. Thangadurai, Structural, optical and photocatalytic properties of graphene-ZnO nanocomposites for varied compositions, *J. Phys. Chem. Solids.* 102 (2017) 168–177. <https://doi.org/10.1016/j.jpss.2016.11.024>.
- [25] A.O. Ibhaddon, P. Fitzpatrick, Heterogeneous photocatalysis: Recent advances and applications, *Catalysts.* 3 (2013) 189–218. <https://doi.org/10.3390/catal3010189>.
- [26] H. Dong, G. Zeng, L. Tang, C. Fan, C. Zhang, X. He, Y. He, An overview on limitations of TiO₂-based particles for photocatalytic degradation of organic pollutants and the corresponding countermeasures, *Water Res.* 79 (2015) 128–146. <https://doi.org/10.1016/j.watres.2015.04.038>.
- [27] J. Luo, X. Zhou, L. Ma, X. Ning, L. Zhan, X. Xu, L. Xu, L. Zhang, H. Ruan, Z. Zhang, Fabrication of WO₃/Ag₂CrO₄ composites with enhanced visible-light photodegradation towards methyl orange, *Adv. Powder Technol.* 28 (2017) 1018–1027. <https://doi.org/10.1016/j.apt.2017.01.006>.
- [28] F. Achouri, S. Corbel, L. Balan, K. Mozet, E. Giro, G. Medjahdi, M. Ben Said, A. Ghrabi, R. Schneider, Porous Mn-doped ZnO nanoparticles for enhanced solar and visible light photocatalysis, *Mater. Des.* 101 (2016) 309–316. <https://doi.org/10.1016/j.matdes.2016.04.015>.
- [29] H. Fan, X. Zhao, J. Yang, X. Shan, L. Yang, Y. Zhang, X. Li, M. Gao, ZnO-graphene composite for photocatalytic degradation of methylene blue dye, *Catal. Commun.* 29 (2012) 29–34. <https://doi.org/10.1016/j.catcom.2012.09.013>.
- [30] L. Wang, Z. Li, J. Chen, Y. Huang, H. Zhang, H. Qiu, Enhanced photocatalytic degradation of methyl orange by porous graphene/ZnO nanocomposite, *Environ. Pollut.* 249 (2019) 801–811. <https://doi.org/10.1016/j.envpol.2019.03.071>.
- [31] V. Singh, D. Joung, L. Zhai, S. Das, Progress in Materials Science Graphene based materials : Past, present and future, *Prog. Mater. Sci.* 56 (2011) 1178–1271. <https://doi.org/10.1016/j.pmatsci.2011.03.003>.
- [32] T.J.M. Fraga, M.N. Carvalho, M.G. Ghislandi, A. Maurício, M. Sobrinho, Functionalized Graphene-based materials as innovative adsorbents of organic pollutants: A concise overview, *Braz. J. Chem* (2019) 36. <https://doi.org/10.1590/0104-6632.20190361s20180283>.

- [33] X. Chen, Z. Wu, D. Liu, Z. Gao, Preparation of ZnO Photocatalyst for the Efficient and Rapid Photocatalytic Degradation of Azo Dyes, (2017) 4–13. <https://doi.org/10.1186/s11671-017-1904-4>.
- [34] M. I. Litter, N. Quici, Photochemical Advanced Oxidation Processes for Water and Wastewater Treatment, *Recent Patents Eng.* 4 (2011) 217–241. <https://doi.org/10.2174/187221210794578574>.
- [35] Y.H. Chiu, T.M. Chary, C.Y. Chen, M.Sone, Y. Hsu, Mechanistic Insights into Photodegradation of Organic Dyes Using Heterostructure Photocatalysts, *Catalysts*. 9 (2019) 430. <https://doi.org/10.3390/catal9050430>
- [36] J.L. Wang, L.J. Xu, Advanced oxidation processes for wastewater treatment: Formation of hydroxyl radical and application, *Crit. Rev. Environ. Sci. Technol.* 42 (2012) 251–325. <https://doi.org/10.1080/10643389.2010.507698>.
- [37] G. Kiriakidis, V. Binas, Metal oxide semiconductors as visible light photocatalysts, *J. Korean Phys. Soc.* 65 (2014) 297–302. <https://doi.org/10.3938/jkps.65.297>.
- [38] N. Sutin, P. Gülich, Comments[®] on inorganic chemistry: A Journal of Critical Discussion of the Current Literature, *Comments Inorg. Chem.* 4 (1985) a. <https://doi.org/10.1080/02603598508072259>.
- [39] T. Hisatomi, J. Kubota, K. Domen, Recent advances in semiconductors for photocatalytic and photoelectrochemical water splitting, *Chem. Soc. Rev.* 43 (2014) 7520–7535. <https://doi.org/10.1039/c3cs60378d>.
- [40] M.M. Khan, S. F. Adil, A. Al-Mayouf, Metal oxides as photocatalysts, *Journal of Saudi Chemical Society.* 19 (2015) 462–464. <https://doi.org/10.1016/j.jscs.2015.04.003>.
- [41] S.H.S. Chan, T.Y. Wu, J.C. Juan, C.Y. Teh, Recent developments of metal oxide semiconductors as photocatalysts in advanced oxidation processes (AOPs) for treatment of dye waste-water, *J. Chem. Technol. Biotechnol.* 86 (2011) 1130–1158. <https://doi.org/10.1002/jctb.2636>.
- [42] A.V. Salker, Solar-Light-Assisted Photo-degradation of Azo Dyes Using Some Transition Metal Oxides, *Sol. Radiat. Appl.* (2015). <https://doi.org/10.5772/59962>.
- [43] M. Pirhashemi, A. Habibi-Yangjeh, Ultrasonic-assisted preparation of novel ternary ZnO/Ag₃VO₄/Ag₂CrO₄ nanocomposites and their enhanced visible-light activities in degradation of different pollutants, *Solid State Sci.* 55 (2016) 58–68. <https://doi.org/10.1016/j.solidstatesciences.2016.02.006>.
- [44] L. Zhu, D. Huang, J. Ma, D. Wu, M. Yang, S. Komarneni, Fabrication of AgBr/Ag₂CrO₄ composites for enhanced visible-light photocatalytic activity, *Ceram. Int.* 41 (2015) 12509–12513. <https://doi.org/10.1016/j.ceramint.2015.05.118>.
- [45] D. Xu, B. Cheng, S. Cao, J. Yu, Enhanced photocatalytic activity and stability of Z-scheme

- Ag₂CrO₄-GO composite photocatalysts for organic pollutant degradation, *Appl. Catal. B Environ.* 164 (2015) 380–388. <https://doi.org/10.1016/j.apcatb.2014.09.051>.
- [46] M. Pirhashemi, A. Habibi-Yangjeh, Novel ZnO/Ag₂CrO₄ nanocomposites with n–n heterojunctions as excellent photocatalysts for degradation of different pollutants under visible light, *J. Mater. Sci. Mater. Electron.* 27 (2016) 4098–4108. <https://doi.org/10.1007/s10854-015-4269-4>.
- [47] S. Klosek, D. Raftery, Visible Light Driven V-Doped TiO₂ Photocatalyst and Its Photooxidation of Ethanol, *J. Phys. Chem. B.* 105(2001) 2815–2819. <https://doi.org/10.1021/jp004295e>.
- [48] V. Binas, D. Venieri, D. Kotzias, G. Kiriakidis, Modified TiO₂ based photocatalysts for improved air and health quality, *J. Mater.* 3 (2017) 3–16. <https://doi.org/10.1016/j.jmat.2016.11.002>.
- [49] B. Guan, J. Yu, S. Guo, S. Yu, S. Han, Porous nickel doped titanium dioxide nanoparticles with improved visible light photocatalytic activity, *Nanoscale Adv.* 2 (2020) 1352–1357. <https://doi.org/10.1039/c9na00760a>.
- [50] S. Hernández, D. Hidalgo, A. Sacco, A. Chiodoni, A. Lamberti, V. Cauda, E. Tresso, G. Saracco, Comparison of photocatalytic and transport properties of TiO₂ and ZnO nanostructures for solar-driven water splitting, *Phys. Chem. Chem. Phys.* 17 (2015) 7775–7786. <https://doi.org/10.1039/c4cp05857g>.
- [51] A.A. Yaqoob, T. Parveen, K. Umar, M.N.M. Ibrahim, Role of Nanomaterials in the Treatment of Wastewater, *Water.* 12(2020) 495. <https://doi.org/10.3390/w12020495>.
- [52] A. Kolodziejczak-Radzimska, T. Jesionowski, Zinc oxide-from synthesis to application: A review, *Materials (Basel).* 7 (2014) 2833–2881. <https://doi.org/10.3390/ma7042833>.
- [53] A.M. Díez-pascual, *Biodegradable Food Packaging Nanocomposites Based on ZnO-reinforced Polyhydroxyalkanoates*, Elsevier Inc., 2017. <https://doi.org/10.1016/B978-0-12-804302-8.00006-6>
- [54] E. Kärber, T. Raadik, T. Dedova, J. Krustok, A. Mere, V. Mikli, M. Krunks, Photoluminescence of spray pyrolysis deposited ZnO nanorods, *Nanoscale Res. Lett.* 6 (2011) 1–7. <https://doi.org/10.1186/1556-276X-6-359>.
- [55] A.R. Nanakkal, L.K. Alexander, Photocatalytic Activity of Graphene/ZnO Nanocomposite Fabricated by Two-step Electrochemical Route, *J. Chem. Sci.* 129 (2017) 95–102. <https://doi.org/10.1007/s12039-016-1206-x>.
- [56] T. Van Khai, L. Van Thu, L. Thi, T. Ha, V. Minh, T. Dai, Materials Characterization Structural , optical and gas sensing properties of vertically well-aligned ZnO nanowires grown on graphene / Si substrate by thermal evaporation method, *Mater. Charact.* 141 (2018) 296–317. <https://doi.org/10.1016/j.matchar.2018.04.047>.

- [57] Ü. Özgür, Y.I. Alivov, C. Liu, A. Teke, M.A. Reshchikov, M.A. Reshchikov, S. Dogan, V. Avrutin, S-J. Cho, H. Morkoc, A comprehensive review of ZnO materials and devices, *Journal of Applied Physics*. 98, 041301 (2005). <https://doi.org/10.1063/1.1992666>.
- [58] K. Davis, R. Yarbrough, M. Froeschle, J. White, H. Rathnayabe, Band gap engineered zinc oxide nanostructures via a sol-gel synthesis of solvent driven shape- controlled crystal growth†, *RSC Adv*. 9 (2019) 14638–14648. <https://doi.org/10.1039/c9ra02091h>.
- [59] S. Talam, S.R. Karumuri, N. Gunnam, Synthesis, Characterization, and Spectroscopic Properties of ZnO Nanoparticles, *ISRN Nanotechnol*. 2012 (2012) 1–6. <https://doi.org/10.5402/2012/372505>.
- [60] K.S. Siddiqi, A. ur Rahman, Tajuddin, A. Husen, Properties of Zinc Oxide Nanoparticles and Their Activity Against Microbes, *Nanoscale Res. Lett*. 13 (2018). <https://doi.org/10.1186/s11671-018-2532-3>.
- [61] A. Diallo, B.D. Ngom, E. Park, M. Maaza, Green synthesis of ZnO nanoparticles by *Aspalathus linearis* : Structural & optical properties, *J. Alloys Compd*. 646 (2015). <https://doi.org/10.1016/j.jallcom.2015.05.242>.
- [62] S. Iravani, Green synthesis of metal nanoparticles using plants, *Green Chem*. 13 (2011) 2638–2650. <https://doi.org/10.1039/c1gc15386b>.
- [63] R. Mohammadinejad, S. Karimi, S. Iravani, R.S. Varma, Plant-derived nanostructures: types and applications, *Green Chem*. 18 (2015) 20–52. <https://doi.org/10.1039/c5gc01403d>.
- [64] S. Ahmed, M. Ahmad, B.L. Swami, S. Ikram, A review on plants extract mediated synthesis of silver nanoparticles for antimicrobial applications: A green expertise, *J. Adv. Res*. 7 (2016) 17–28. <https://doi.org/10.1016/j.jare.2015.02.007>.
- [65] R. Prasad, M. Kumar, V. Kumar, Green Nanotechnology: Biomimetic Synthesis of Metal Nanoparticles Using Plants and Their Application in Agriculture and Forestry, *Nanotechnology*. (2017). <https://doi.org/10.1007/978-981-10-4573-8>.
- [66] M. Soković, H. Skaltsa, I.C.F.R. Ferreira, Editorial: Bioactive Phytochemicals in Asteraceae: Structure, Function, and Biological Activity, *Front. Plant Sci*. 10 (2019) 1–2. <https://doi.org/10.3389/fpls.2019.01464>.
- [67] H. Fouad, E.S. Habib, S.A. Ahmed, Phytochemistry and Pharmacological Effects of Plants in Genus *Sonchus* (Asteraceae), *Records of pharmaceutical and biomedical sciences* (2011). <http://dx.doi.org/10.21608/rpbs.2019.18952.1046>
- [68] S.K. Chandraker, M. Lal, M.K. Ghosh, V. Tiwari, T.K. Ghorai, R. Shukla, Green synthesis of copper nanoparticles using leaf extract of *Ageratum houstonianum* Mill. and study of their photocatalytic and antibacterial activities , *Nano Express*. 1 (2020) 010033. <https://doi.org/10.1088/2632-959x/ab8e99>.

- [69] E.S. Madivoli, P.G. Kareru, E.G. Maina, A.O. Nyabola, S.I. Wanakai, J.O. Nyang'au, Biosynthesis of iron nanoparticles using *Ageratum conyzoides* extracts, their antimicrobial and photocatalytic activity, *SN Appl. Sci.* 1 (2019) 1–11. <https://doi.org/10.1007/s42452-019-0511-7>.
- [70] E.E. Elemike, D.C. Onwudiwe, A.C. Ekennia, C.U. Sonde, R.C. Ehiri, Green synthesis of Ag/Ag₂O nanoparticles using aqueous leaf extract of *Eupatorium odoratum* and its antimicrobial and mosquito larvicidal activities, *Molecules.* 22 (2017) 1–15. <https://doi.org/10.3390/molecules22050674>.
- [71] J. Karimi Andeani, S. Mohsenzadeh, Phytosynthesis of cadmium oxide nanoparticles from *Achillea wilhelmsii* flowers, *J. Chem.* 2013 (2013). <https://doi.org/10.1155/2013/147613>.
- [72] M. Zeeshan, S.M.D. Rizvi, M.S. Khan, A. Kumar, Isolation, partial purification and evaluation of bioactive compounds from leaves of *Ageratum houstonianum*, *EXCLI J.* 11 (2012) 78–88. <https://doi.org/10.17877/DE290R-4911>.
- [73] N. Matinise, X.G. Fuku, K. Kaviyarasu, N. Mayedwa, M. Maaza, Applied Surface Science ZnO nanoparticles via *Moringa oleifera* green synthesis : Physical properties & mechanism of formation, *Appl. Surf. Sci.* 406 (2017) 339–347. <https://doi.org/10.1016/j.apsusc.2017.01.219>.
- [74] M. Naseer, U. Aslam, B. Khalid, B. Chen, Green route to synthesize Zinc Oxide Nanoparticles using leaf extracts of *Cassia fistula* and *Melia azadarach* and their antibacterial potential. *Sci Rep* 10, 9055 (2020). <https://doi.org/10.1038/s41598-020-65949-3>
- [75] F.T. Thema, E. Manikandan, M.S. Dhlamini, M. Maaza, Green synthesis of ZnO nanoparticles via *Agathosma betulina* natural extract, *Mater. lett.* 161 (2015) 124–127. <https://doi.org/10.1016/j.matlet.2015.08.052>.
- [76] K.M. Ezealisiji, X. Siwe-Noundou, B. Maduelosi, N. Nwachukwu, R.W.M. Krause, Green synthesis of zinc oxide nanoparticles using *Solanum torvum* (L) leaf extract and evaluation of the toxicological profile of the ZnO nanoparticles–hydrogel composite in Wistar albino rats, *Int. Nano Lett.* 9 (2019) 99–107. <https://doi.org/10.1007/s40089-018-0263-1>.
- [77] G. Sharmila, M. Thirumarimurugan, C. Muthukumar, Green synthesis of ZnO nanoparticles using *Tecoma castanifolia* leaf extract: Characterization and evaluation of its antioxidant, bactericidal and anticancer activities, *Microchem. J.* 145 (2019) 578–587. <https://doi.org/10.1016/j.microc.2018.11.022>.
- [78] N. Abdullah, N.A. Al-Dhabi, M.V. Arasu, Environmentally-Friendly Green Approach for the Production of Zinc Oxide Nanoparticles and Their Anti-Fungal, Ovicidal, and Larvicidal Properties, *J. nanomat.* 7 (2018). <https://doi.org/10.3390/nano8070500>.
- [79] S. Vijayakumar, C. Krishnakumar, P. Arulmozhi, S. Mahadevan, N. Parameswari,

- Biosynthesis, characterization and antimicrobial activities of zinc oxide nanoparticles from leaf extract of *Glycosmis pentaphylla* (Retz.) DC, *Microb. Pathog.* 116 (2018) 44–48. <https://doi.org/10.1016/j.micpath.2018.01.003>.
- [80] S.K. Chaudhuri, L. Malodia, Biosynthesis of zinc oxide nanoparticles using leaf extract of *calotropis gigantea*: Characterization and its evaluation on tree seedling growth in nursery stage, *Appl. Nanosci.* 7 (2017) 501–512. <https://doi.org/10.1007/s13204-017-0586-7>.
- [81] M.G. Demissie, F.K. Sabir, G.D. Edossa, B.A. Gonfa, Synthesis of Zinc Oxide Nanoparticles Using Leaf Extract of *Lippia adoensis* (Koseret) and Evaluation of Its Antibacterial Activity, *J. Chem.* 2020 (2020). <https://doi.org/10.1155/2020/7459042>.
- [82] S.P. Rajendran, K. Sengodan, Synthesis and Characterization of Zinc Oxide and Iron Oxide Nanoparticles Using *Sesbania grandiflora* Leaf Extract as Reducing Agent, *J. Nanosci.* 2017 (2017). <https://doi.org/10.1155/2017/8348507>.
- [83] A. Abdelkhalek, A.A. Al-Askar, Green synthesized ZnO nanoparticles mediated by *Mentha spicata* extract induce plant systemic resistance against Tobacco mosaic virus, *Appl. Sci.* 10 (2020). <https://doi.org/10.3390/app10155054>.
- [84] T. Uyen, D. Thi, T. Nguyen, Y.D. Thi, H. Ta, Green synthesis of ZnO nanoparticles using orange fruit peel extract for antibacterial activities, *RSC Adv.* 10 (2020) 23899–23907. <https://doi.org/10.1039/d0ra04926c>.
- [85] D. Sharma, M.I. Sabela, S. Kanchi, P.S. Mdluli, G. Singh, T.A. Stenström, K. Bisetty, *Journal of Photochemistry & Photobiology, B: Biology* Biosynthesis of ZnO nanoparticles using *Jacaranda mimosifolia* flowers extract: Synergistic antibacterial activity and molecular simulated facet specific adsorption studies, *JPB.* 162 (2016) 199–207. <https://doi.org/10.1016/j.jphotobiol.2016.06.043>.
- [86] P. Jamdagni, P. Khatri, J.S. Rana, Green synthesis of zinc oxide nanoparticles using flower extract of *Nyctanthes arbor-tristis* and their antifungal activity, *J. King Saud Univ. - Sci.* 30 (2018) 168–175. <https://doi.org/10.1016/j.jksus.2016.10.002>.
- [87] N.R. Subhash, C. Arvind, Green synthesis of zinc oxide nano-sized spherical particles using *Terminalia chebula* fruits extract for their photocatalytic applications, *Int. Nano Lett.* (2016). <https://doi.org/10.1007/s40089-015-0171-6>.
- [88] L. Chen, I. Batjikh, J. Hurh, Y. Han, Y. Huo, H. Ali, J. Feng, E. Jahan, J. Chan, R. Mathiyalagan, Optik Green synthesis of zinc oxide nanoparticles from root extract of *Scutellaria baicalensis* and its photocatalytic degradation activity using methylene blue, *Opt. - Int. J. Light Electron Opt.* 184 (2019) 324–329. <https://doi.org/10.1016/j.ijleo.2019.03.051>.
- [89] S.S. Dogan, A. Kocabas, Green synthesis of ZnO nanoparticles with *Veronica multifida* and their antibiofilm activity, *J. Hum Exp Toxicol.* (2019) 1-9.

<https://doi.org/10.1177/0960327119888270>.

- [90] C. Joel, M.S.M. Badhusha, S. John, Green synthesis of ZnO Nanoparticles using *Phyllanthus embilica* Stem extract and their Antibacterial activity, *J. Der Pharmacia Lettre.* 8 (2016) 218–223. <http://scholarsresearchlibrary.com/archive.html>.
- [91] A. Escobar, A. Vladimir, D. Verónica, S. Rodríguez, N. Ayerim, Modified Metallic Oxides for Efficient Photocatalysis, (2018). <https://doi.org/10.5772/intechopen.80834>.
- [92] S.P. Meshram, P. V. Adhyapak, S.K. Pardeshi, I.S. Mulla, D.P. Amalnerkar, Sonochemically generated cerium doped ZnO nanorods for highly efficient photocatalytic dye degradation, *Powder Technol.* 318 (2017) 120–127. <https://doi.org/10.1016/j.powtec.2017.05.044>.
- [93] Z. Durmus, B.Z. Kurt, A. Durmus, Synthesis and Characterization of Graphene Oxide/Zinc Oxide (GO/ZnO) Nanocomposite and Its Utilization for Photocatalytic Degradation of Basic Fuchsin Dye, *ChemistrySelect.* 4 (2019) 271–278. <https://doi.org/10.1002/slct.201803635>.
- [94] M.S. Nasrollahzadeh, M. Hadavifar, S.S. Ghasemi, M. Arab Chamjangali, Synthesis of ZnO nanostructure using activated carbon for photocatalytic degradation of methyl orange from aqueous solutions, *Appl. Water Sci.* 8 (2018) 1–12. <https://doi.org/10.1007/s13201-018-0750-6>.
- [95] H. Yao, F. Li, J. Lutkenhaus, M. Kotaki, H.J. Sue, High-performance photocatalyst based on nanosized ZnO-reduced graphene oxide hybrid for removal of Rhodamine B under visible light irradiation, *AIMS Mater. Sci.* 3 (2016) 1410–1425. <https://doi.org/10.3934/matersci.2016.4.1410>.
- [96] H. Bozetine, Q. Wang, A. Barras, M. Li, T. Hadjersi, S. Szunerits, R. Boukherroub, Green chemistry approach for the synthesis of ZnO-carbon dots nanocomposites with good photocatalytic properties under visible light, *J. Colloid Interface Sci.* 465 (2016) 286–294. <https://doi.org/10.1016/j.jcis.2015.12.001>.
- [97] S.P. Lonkar, V. Pillai, A. Abdala, Solvent-free synthesis of ZnO-graphene nanocomposite with superior photocatalytic activity, *Appl. Surf. Sci.* 465 (2019) 1107–1113. <https://doi.org/10.1016/j.apsusc.2018.09.264>.
- [98] F. Chen, J. Yang, T. Bai, B. Long, X. Zhou, Facile synthesis of few-layer graphene from biomass waste and its application in lithium ion batteries, *J. Electroanal. Chem.* 768 (2016) 18–26. <https://doi.org/10.1016/j.jelechem.2016.02.035>.
- [99] W. Yuan, Y. Gu, L. Li, Green synthesis of graphene/Ag nanocomposites, *Appl. Surf. Sci.* 261 (2012) 753–758. <https://doi.org/10.1016/j.apsusc.2012.08.094>.
- [100] M. Hu, Z. Yao, X. Wang, Characterization techniques for graphene-based materials in

- catalysis, *AIMS Mater. Sci.* 4 (2017) 755–788.
<https://doi.org/10.3934/materci.2017.3.755>.
- [101] J. Phiri, P. Gane, T.C. Maloney, General overview of graphene: Production, properties and application in polymer composites, *Mater. Sci. Eng. B Solid-State Mater. Adv. Technol.* 215 (2017) 9–28. <https://doi.org/10.1016/j.mseb.2016.10.004>.
- [102] P.K. Sandhya, J. Jose, M.S. Sreekala, M. Padmanabhan, N. Kalarikkal, S. Thomas, Reduced graphene oxide and ZnO decorated graphene for biomedical applications, *Ceram. Int.* 44 (2018) 15092–15098. <https://doi.org/10.1016/j.ceramint.2018.05.143>.
- [103] S.S.P. Haghshenas, A. Nemati, R. Simchi, C.U. Kim, Photocatalytic and photoluminescence properties of ZnO/graphene quasi core-shell nanoparticles, *Ceram. Int.* 45 (2019) 8945–8961. <https://doi.org/10.1016/j.ceramint.2019.01.226>.
- [104] S.S. Shams, L.S. Zhang, R. Hu, R. Zhang, J. Zhu, Synthesis of graphene from biomass: A green chemistry approach, *Mater. Lett.* 161 (2015) 476–479.
<https://doi.org/10.1016/j.matlet.2015.09.022>.
- [105] J. Hao, L. Ji, K. Wu, N. Yang, Electrochemistry of ZnO@reduced graphene oxides, *Carbon N. Y.* 130 (2018) 480–486. <https://doi.org/10.1016/j.carbon.2018.01.018>.
- [106] N. Karimizadeh, M. Babamoradi, R. Azimirad, M. Khajeh, Synthesis of Three-Dimensional Multilayer Graphene Foam/ZnO Nanorod Composites and Their Photocatalyst Application, *J. Electron. Mater.* 47 (2018) 5452–5457. <https://doi.org/10.1007/s11664-018-6427-y>.
- [107] X. Zhu, X. Xu, F. Liu, J. Jin, L. Liu, Y. Zhi, Z.W. Chen, Z.S. Zhou, J. Yu, Green synthesis of graphene nanosheets and their in vitro cytotoxicity against human prostate cancer (DU 145) cell lines, *Nanomater. Nanotechnol.* 7 (2017) 1–7.
<https://doi.org/10.1177/1847980417702794>.
- [108] Z. Anwar, M. Gulfranz, M. Irshad, Agro-industrial lignocellulosic biomass a key to unlock the future bio-energy: A brief review, *J. Radiat. Res. Appl. Sci.* 7 (2014) 163–173.
<https://doi.org/10.1016/j.jrras.2014.02.003>.
- [109] C.A. De Carvalho Mendes, F.A. De Oliveira Adnet, M.C.A.M. Leite, C.R.G. Furtado, A.M.F. De Sousa, Chemical, physical, mechanical, thermal and morphological characterization of corn husk residue, *Cellul. Chem. Technol.* 49 (2015) 727–735.
<https://www.semanticscholar.org/paper/CHEMICAL-%2C-PHYSICAL-%2C-MECHANICAL-%2C-THERMAL-AND-OF-Mendes-Adnet/5034807d533b0cc5909c7d89822a49c6641645f2>
- [110] M. Szymanska-Chargot, M. Chylinska, K. Gdula, A. Koziol, A. Zdunek, Isolation and characterization of cellulose from different fruit and vegetable pomaces, *Polymers (Basel)*. 9 (2017). <https://doi.org/10.3390/polym9100495>.
- [111] L.A. Larissa, A.F. Fonsêca, F. V. Pereira, J.I. Druzian, Extraction and characterization of

- cellulose nanocrystals from corn stover, *Cellul. Chem. Technol.* 49 (2015) 127–133.
<https://doi.org/10.1016/j.matpr.2015.04.045>
- [112] B.L. Gbenga, Q.W. Gbemi, A. Bamiro Oluyemisi, Evaluation of cellulose obtained from maize husk as compressed tablet excipient, *Der Pharm. Lett.* 5 (2013) 12–17.
<https://www.scholarsresearchlibrary.com/articles/evaluation-of-cellulose-obtained-from-maize-husk-as-compressed-tabletexcipient.pdf>
- [113] K. Lefatshe, C.M. Muiva, L.P. Kebaabetswe, Extraction of nanocellulose and in-situ casting of ZnO/cellulose nanocomposite with enhanced photocatalytic and antibacterial activity, *Carbohydr. Polym.* 164 (2017) 301–308. <https://doi.org/10.1016/j.carbpol.2017.02.020>.
- [114] Y. Hu, O. Hamed, R. Salghi, N. Abidi, S. Jodeh, R. Hattb, Extraction and Characterization of Cellulose From Agricultural Waste Argan Press Cake, *Cellul. Chem. Technol. Cellul. Chem. Technol.* 51 (2017) 263–272. [http://www.cellulosechemtechnol.ro/pdf/CCT3-4\(2017\)/p.263-272.pdf](http://www.cellulosechemtechnol.ro/pdf/CCT3-4(2017)/p.263-272.pdf).
- [115] P. Kampeerappun, Extraction and Characterization of Cellulose Nanocrystals Produced by Acid Hydrolysis from Corn Husk, *J. Met. Mater. Miner. J. Met. Mater. Min.* 25 (2015) 19–26. <https://doi.org/10.14456/jmmm.2015.3>.
- [116] X. feng Zeng, J. sheng Wang, Y. na Zhao, W. li Zhang, M. huan Wang, Construction of TiO₂-pillared multilayer graphene nanocomposites as efficient photocatalysts for ciprofloxacin degradation, *Int. J. Miner. Metall. Mater.* 28 (2021) 503–510.
<https://doi.org/10.1007/s12613-020-2193-y>.
- [117] S. Steplin Paul Selvin, A. Ganesh Kumar, L. Sarala, R. Rajaram, A. Sathiyam, J. Princy Merlin, I. Sharmila Lydia, Photocatalytic Degradation of Rhodamine B Using Zinc Oxide Activated Charcoal Polyaniline Nanocomposite and Its Survival Assessment Using Aquatic Animal Model, *ACS Sustain. Chem. Eng.* 6 (2018) 258–267.
<https://doi.org/10.1021/acssuschemeng.7b02335>.
- [118] X. Wang, Y. Wang, Z. Yan, Photocatalytic degradation of rhodamine B dye over novel porous Ti O₂ -Sn O₂ Nanocomposites prepared by hydrothermal method, *Int. J. Photoenergy.* 2014 (2014). <https://doi.org/10.1155/2014/928519>.
- [119] Y. Tong, J. Kang, J. Shen, Z. Chen, S. Zhao, L. Sun, W. Wang, Effective degradation of doxycycline by photocatalytic BiVO₄-H₂O₂ under visible light, *Environ. Prog. Sustain. Energy.* 38 (2019) 1–7. <https://doi.org/10.1002/ep.13259>.
- [120] P.J. Ramesh, K. Basavaiah, M.R. Divya, N. Rajendraprasad, K.B. Vinay, H.D. Revanasiddappa, Simple UV and visible spectrophotometric methods for the determination of doxycycline hyclate in pharmaceuticals, *J. Anal. Chem.* 66 (2011) 482–489. <https://doi.org/10.1134/S1061934811050157>.
- [121] X. Wu, L. Wen, K. Lv, K. Deng, D. Tang, H. Ye, D. Du, S. Liu, M. Li, Fabrication of ZnO/graphene flake-like photocatalyst with enhanced photoreactivity, *Appl. Surf. Sci.*

- 358 (2015) 130–136. <https://doi.org/10.1016/j.apsusc.2015.08.061>.
- [122] S. Azizi, M.B. Ahmad, N.A. Ibrahim, M.Z. Hussein, F. Namvar, Cellulose nanocrystals/ZnO as a bifunctional reinforcing nanocomposite for poly(vinyl alcohol)/chitosan blend films: Fabrication, characterization and properties, *Int. J. Mol. Sci.* 15 (2014) 11040–11053. <https://doi.org/10.3390/ijms150611040>.
- [123] H.P.S.A. Khalil, Y. Davoudpour, N. Islam, A. Mustapha, K. Sudesh, R. Dungani, M. Jawaid, Production and modification of nanofibrillated cellulose using various mechanical processes : A review, *Carbohydr. Polym.* 99 (2014) 649–665. <https://doi.org/10.1016/j.carbpol.2013.08.069>.
- [124] B.S. Girgis, Y.M. Temerk, M.M. Gadelrab, I.D. Abdullah, X-ray Diffraction Patterns of Activated Carbons Prepared under Various Conditions, *J. Carb Lett.* 8 (2007) 95–100. <https://doi.org/10.5714/CL.2007.8.2.095>.
- [125] D. Xrd, A.C. Mohan, B. Renjanadevi, Preparation of Zinc Oxide Nanoparticles and its Characterization Using Scanning Electron Microscopy (SEM) and X-Ray, *Procedia Technol.* 24 (2016) 761–766. <https://doi.org/10.1016/j.protcy.2016.05.078>.
- [126] F. T. L. Muniz, M. A. R. Miranda, C. M. D. Santos, J. M. Sasaki, The Scherrer equation and the dynamical theory of X-ray diffraction, *Acta Crystallogr A Found Adv*, (2016) 385–390. <https://doi.org/10.1107/S205327331600365X>.
- [127] D. Nath, F. Singh, R. Das, X-ray diffraction analysis by Williamson-Hall , Halder-Wagner and size-strain plot methods of CdSe nanoparticles- a comparative study, *Mater. Chem. Phys.* 239 (2020) 122021. <https://doi.org/10.1016/j.matchemphys.2019.122021>.
- [128] A.O. Juma, E.A.A. Arbab, C.M. Muiva, L.M. Lepodise, Synthesis and characterization of CuO-NiO-ZnO mixed metal oxide nanocomposite, *J. Alloys Compd.* 723 (2017) 866–872. <https://doi.org/10.1016/j.jallcom.2017.06.288>.
- [129] V.D. Mote, Y. Purushotham, B.N. Dole, Williamson-Hall analysis in estimation of lattice strain in nanometer-sized ZnO particles, *J. Theor Appl Phys.* 6 (2012) 2–9. <https://doi.org/10.1186/2251-7235-6-6>.
- [130] H. Wasly, X-Ray Analysis for Determination of the Crystallite size and Lattice Strain in ZnO nanoparticles, *J. Al-Azhar Univ. Eng. Sect.* 13 (2018) 1312–1320. <https://doi.org/10.21608/auej.2018.18943>.
- [131] F. Izumi, T. Ikeda, Implementation of the Williamson – Hall and Halder – Wagner Methods into RIETAN-FP, *Adv. Ceram. Res. Cent. Annu. Rep.* 3 (2014) 33–38. http://www.crl.nitech.ac.jp/ar/2014/3338_acrc_ar2014_review.pdf
- [132] A.A. Al-Tabbakh, Crystallite size and lattice strain of lithiated spinel material for rechargeable battery by X - ray diffraction peak - broadening analysis, *Int. J. Energy Res* (2019) 1–9. <https://doi.org/10.1002/er.4390>.

- [133] T. Chandra, J. Podder, M. Haque, Optical constants and dispersion energy parameters of Zn-doped TiO₂ thin films prepared by spray pyrolysis technique, *Surfaces and Interfaces*. 21 (2020) 100725. <https://doi.org/10.1016/j.surfin.2020.100725>.
- [134] A. Das, S. Pisana, B. Chakraborty, S. Piscanec, S.K. Saha, U. V Waghmare, K.S. Novoselov, H.R. Krishnamurthy, A.K. Geim, A.C. Ferrari, A.K. Sood, Monitoring dopants by Raman scattering in an electrochemically top-gated graphene transistor, *Nature Nanotech.* 3 (2008) 1–6. <https://doi.org/10.1038/nnano.2008.67>.
- [135] A. Lazzarini, A. Piovano, R. Pellegrini, G. Agostini, S. Rudić, C. Lamberti, E. Groppo, Graphitization of Activated Carbons: A Molecular-level Investigation by INS, DRIFT, XRD and Raman Techniques, *Phys. Procedia*. 85 (2016) 20–26. <https://doi.org/10.1016/j.phpro.2016.11.076>.
- [136] L. Bokobza, J.-L. Bruneel, M. Couzi, Raman Spectra of Carbon-Based Materials (from Graphite to Carbon Black) and of Some Silicone Composites, *C.* 1 (2015) 77–94. <https://doi.org/10.3390/c1010077>.
- [137] D.H. Seo, S. Pineda, J. Fang, Y. Gozukara, S. Yick, A. Bendavid, S.K.H. Lam, A.T. Murdock, A.B. Murphy, Z.J. Han, K.K. Ostrikov, Single-step ambient-air synthesis of graphene from renewable precursors as electrochemical genosensor, *Nat. Commun.* 8 (2017) 1–9. <https://doi.org/10.1038/ncomms14217>.
- [138] S. Wang, Z. Hu, J. Shi, G. Chen, Q. Zhang, Z. Weng, K. Wu, M. Lu, Green synthesis of graphene with the assistance of modified lignin and its application in anticorrosive waterborne epoxy coatings, *Appl. Surf. Sci.* 484 (2019) 759–770. <https://doi.org/10.1016/j.apsusc.2019.03.229>.
- [139] I.K. Moon, J. Lee, R.S. Ruoff, H. Lee, Reduced graphene oxide by chemical graphitization, *Nat. Commun.* 1 (2010). <https://doi.org/10.1038/ncomms1067>.
- [140] D.H. Seo, A.E. Rider, Z.J. Han, S. Kumar, K. Ostrikov, Plasma break-down and re-build: Same functional vertical graphenes from diverse natural precursors, *Adv. Mater.* 25 (2013) 5638–5642. <https://doi.org/10.1002/adma.201301510>.
- [141] T.C. Damen, S.P.S. Porto, B. Tell, Raman Effect in ZnO, *Phys. Rev.* 142 (1966) 570–573. <https://doi.org/10.1103/PhysRev.142.570>.
- [142] S.A. Azzez, Z. Hassan, J.J. Hassan, Identification and characteristics of core–shell ZnO/ZnO:Mg nanorods synthesized by hydrothermal method, *J. Mater. Sci. Mater. Electron.* 27 (2016) 12618–12626. <https://doi.org/10.1007/s10854-016-5394-4>.
- [143] R.P. Wang, G. Xu, P. Jin, Size dependence of electron-phonon coupling in ZnO nanowires, *Phys. Rev. B - Condens. Matter Mater. Phys.* 69 (2004) 5–8. <https://doi.org/10.1103/PhysRevB.69.113303>.
- [144] L. Lin, J. Liu, J. Lv, S. Shen, X. Wu, D. Wu, Y. Qu, W. Zheng, F. Lai, Correlation between

- native defects and morphological, structural and optical properties of ZnO nanostructures, *J. Alloys Compd.* 695 (2017) 1523–1527. <https://doi.org/10.1016/j.jallcom.2016.10.292>.
- [145] P. Veluswamy, S. Sathiyamoorthy, K.H. Chowdary, O. Muthusamy, K. Krishnamoorthy, T. Takeuchi, H. Ikeda, Morphology dependent thermal conductivity of ZnO nanostructures prepared via a green approach, *J. Alloys Compd.* 695 (2017) 888–894. <https://doi.org/10.1016/j.jallcom.2016.10.196>.
- [146] R. Zhang, P.G. Yin, N. Wang, L. Guo, Photoluminescence and Raman scattering of ZnO nanorods, *Solid State Sci.* 11 (2009) 865–869. <https://doi.org/10.1016/j.solidstatesciences.2008.10.016>.
- [147] R. Taziwa, L. Ntozakhe, M. Edson, Structural, Morphological and Raman Scattering Studies of Carbon Doped ZnO Nanoparticles Fabricated by PSP Technique, *J Nanosci Nanotechnol Res.* 1 (2017) 1–8. <http://www.imedpub.com>.
- [148] P. Noorunnisa Khanam, A. Hasan, Biosynthesis and characterization of graphene by using non-toxic reducing agent from *Allium Cepa* extract: Anti-bacterial properties, *Int. J. Biol. Macromol.* 126 (2019) 151–158. <https://doi.org/10.1016/j.ijbiomac.2018.12.213>.
- [149] H.S. Wahab, S. Ali, A. Abdul Hussein, S.H. Ali, A.M. Abdul Hussein, Synthesis and Characterization of Graphene by Raman Spectroscopy, *J. Mater. Sci. Appl.* 1 (2015) 130–135. <http://www.aascit.org/journal/jmsa>.
- [150] B. Tang, H. Guoxin, H. Gao, Raman spectroscopic characterization of graphene, *Appl. Spectrosc. Rev.* 45 (2010) 369–407. <https://doi.org/10.1080/05704928.2010.483886>.
- [151] P. Hudec, A. Smieskova, Z. Zidek, P. Schneider, O. Solcova, Determination of Microporous Structure of Zeolites by t-Plot Method-State-of-the-Art, *Stud. Surf. Sci. Catal.* (2002) 1587–1594. [https://doi.org/10.1016/S0167-2991\(02\)80328-7](https://doi.org/10.1016/S0167-2991(02)80328-7).
- [152] F. Ambroz, T.J. Macdonald, V. Martis, I.P. Parkin, Evaluation of the BET theory for the characterization of meso and microporous MOFs, *Small Methods.* 2 (2018) 1–17. <https://doi.org/10.1002/smt.201800173>.
- [153] T. Akhtar, M. Alam, Surface Area Study of the Nanocrystalline Zinc Oxide Synthesized by Reverse-Micellar Method, *Int. J. Sci. Res.* 3 (2014) 2277–8179. <https://www.doi.org/10.36106/ijsr>
- [154] G. Varughese, P.W. Jithin, K.T. Usha, Determination of Optical Band Gap Energy of Wurtzite ZnO : Ce Nanocrystallites, *PSIJ.* 5 (2015) 146–154. <https://doi.org/10.9734/PSIJ/2015/14151>.
- [155] S. Sagadevan, K. Pal, Z.Z. Chowdhury, M. Foley, Controllable synthesis of Graphene/ZnO-nanocomposite for novel switching, *J. Alloys Compd.* 728 (2017) 645–654. <https://doi.org/10.1016/j.jallcom.2017.09.061>.

- [156] P.M. Perillo, M.N. Atia, Solar-assisted photodegradation of methyl orange using Cu-doped ZnO nanorods, *Mater. Today Commun.* 17 (2018) 252–258. <https://doi.org/10.1016/j.mtcomm.2018.09.010>.
- [157] M. Salem, S. Akir, I. Massoudi, Y. Litaïem, M. Gaidi, K. Khirouni, Photoelectrochemical and optical properties tuning of graphene-ZnO nanocomposites, *J. Alloys Compd.* 767 (2018) 982–987. <https://doi.org/10.1016/j.jallcom.2018.07.202>.
- [158] J. Xu, Y. Cui, Y. Han, M. Hao, X. Zhang, ZnO-graphene composites with high photocatalytic activities under visible light, *RSC Adv.* 6 (2016) 96778–96784. <https://doi.org/10.1039/c6ra19622e>.
- [159] K.V. Kumar, K. Porkodi, F. Rocha, Langmuir-Hinshelwood kinetics - A theoretical study, *Catal. Commun.* 9 (2008) 82–84. <https://doi.org/10.1016/j.catcom.2007.05.019>.
- [160] R. Atchudan, T.N.J.I. Edison, S. Perumal, M. Shanmugam, Y.R. Lee, Direct solvothermal synthesis of zinc oxide nanoparticle decorated graphene oxide nanocomposite for efficient photodegradation of azo-dyes, *J. Photochem. Photobiol. A Chem.* 337 (2017) 100–111. <https://doi.org/10.1016/j.jphotochem.2017.01.021>.
- [161] M. Khairy, W. Zakaria, Effect of metal-doping of TiO₂ nanoparticles on their photocatalytic activities toward removal of organic dyes, *Egypt. J. Pet.* 23 (2014) 419–426. <https://doi.org/10.1016/j.ejpe.2014.09.010>.
- [162] W. Tie, S.S. Bhattacharyya, Y. Wang, W. He, S.H. Lee, Facile in-situ synthesis of a zinc oxide crystals/few-layered graphene flake composite for enhanced photocatalytic performance, *J. Photochem. Photobiol. A Chem.* 348 (2017) 89–95. <https://doi.org/10.1016/j.jphotochem.2017.08.005>.
- [163] S. He, P. Hou, E. Petropoulos, Y. Feng, Y. Yu, L. Xue, L. Yang, High efficient visible-light photocatalytic performance of Cu/ZnO/rGO nanocomposite for decomposing of aqueous ammonia and treatment of domestic wastewater, *Front. Chem.* 6 (2018) 1–13. <https://doi.org/10.3389/fchem.2018.00219>.
- [164] B. Li, H. Cao, ZnO@graphene composite with enhanced performance for the removal of dye from water, *J. Mater. Chem.* 21 (2011) 3346–3349. <https://doi.org/10.1039/c0jm03253k>.
- [165] L.K. Putri, W.J. Ong, W.S. Chang, S.P. Chai, Heteroatom doped graphene in photocatalysis: A review, *Appl. Surf. Sci.* 358 (2015) 2–14. <https://doi.org/10.1016/j.apsusc.2015.08.177>.
- [166] X. Li, R. Shen, S. Ma, X. Chen, J. Xie, Graphene-based heterojunction photocatalysts, *Appl. Surf. Sci.* 430 (2018) 53–107. <https://doi.org/10.1016/j.apsusc.2017.08.194>.
- [167] Q. Xiang, J. Yu, M. Jaroniec, Graphene-based semiconductor photocatalysts, *Chem. Soc. Rev.* 41 (2012) 782–796. <https://doi.org/10.1039/c1cs15172j>.

- [168] J. Fowsiya, G. Madhumitha, N.A. Al-Dhabi, M.V. Arasu, Photocatalytic degradation of Congo red using *Carissa edulis* extract capped zinc oxide nanoparticles, *J. Photochem. Photobiol. B Biol.* 162 (2016) 395–401. <https://doi.org/10.1016/j.jphotobiol.2016.07.011>.
- [169] P. Wight, Xanthene Dyes, *Kirk-Othmer Encycl. Chem. Technol.* (2000). <https://doi.org/10.1002/0471238961.2401142023090708.a01>.
- [170] K. Ozt, C. Duran, H.C. Yatmaz, C. Ozt, *Journal of Photochemistry and Photobiology A : Chemistry* Photocatalytic efficiency of ZnO plates in degradation of azo dye solutions, 198 (2008) 1–6. <https://doi.org/10.1016/j.jphotochem.2008.02.007>.
- [171] S. Pourmoslemi , A. Mohammadi , F. Kobarfard, M. Amini, Photocatalytic removal of doxycycline from aqueous solution using ZnO nano-particles : a comparison between UV-C and visible light, *Water Sci Technol.* 74 (2016) 1658–1670. <https://doi.org/10.2166/wst.2016.339>.
- [172] D. Klauson, A. Poljakova, N. Pronina, M. Krichevskaya, A. Moiseev, T. Dedova, S. Preis, Aqueous photocatalytic oxidation of doxycycline, *J. Adv. Oxid. Technol.* 16 (2013) 234–243. <https://doi.org/10.1515/jaots-2013-0203>.
- [173] M. Addamo, V. Augugliaro, A. Di Paola, E. García-López, V. Loddo, G. Marcì, L. Palmisano, Removal of drugs in aqueous systems by photoassisted degradation, *J. Appl. Electrochem.* 35 (2005) 765–774. <https://doi.org/10.1007/s10800-005-1630-y>.
- [174] J. Xu, Y. Cui, Y. Han, M. Hao, X. Zhang, ZnO-graphene composites with high photocatalytic activities under visible light, *RSC Adv.* 6 (2016) 96778–96784. <https://doi.org/10.1039/c6ra19622e>.
- [175] G. Li Puma, A. Bono, D. Krishnaiah, J.G. Collin, Preparation of titanium dioxide photocatalyst loaded onto activated carbon support using chemical vapor deposition: A review paper, *J. Hazard. Mater.* 157 (2008) 209–219. <https://doi.org/10.1016/j.jhazmat.2008.01.040>.